Genome concentration limits cell growth and modulates proteome composition in *Escherichia coli*

Jarno Mäkelä[1,2,3,†], Alexandros Papagiannakis[1,2,†], Wei-Hsiang Lin[1,2,&], Michael C. Lanz[4,5,&], Skye Glenn[2,4], Matthew Swaffer[4,¶], Georgi K. Marinov[6], Jan M. Skotheim[4,5], Christine Jacobs-Wagner[1,2,4,*]

[1]Howard Hughes Medical Institute, Stanford University, Stanford, CA 94305, USA

[2]Sarafan Chemistry, Engineering, and Medicine for Human Health Institute, Stanford University, Stanford, CA 94305, USA

[3]Institute of Biotechnology, Helsinki Institute of Life Science, University of Helsinki, Helsinki, Finland

[4]Department of Biology, Stanford University, Stanford, CA 94305, USA

[5]Chan Zuckerberg Biohub, Stanford, CA 94305, USA

[6]Department of Genetics, Stanford University, Stanford, CA 94305, USA

[¶]Current address: Wellcome Centre for Cell Biology, University of Edinburgh, Edinburgh, EH9 3BF, UK

[†]These authors contributed equally to this work.

[&]These authors contributed equally to this work.

[*]For correspondence: jacobs-wagner@stanford.edu

KEYWORDS: DNA limitation, ribosome, RNA polymerase, proteome, cell growth, cell size, single-molecule tracking, single-cell dynamics, tandem-mass-tag mass spectrometry.

ABSTRACT

Defining the cellular factors that drive growth rate and proteome composition is essential for understanding and manipulating cellular systems. In bacteria, ribosome concentration is known to be a constraining factor of cell growth rate, while gene concentration is usually assumed not to be limiting. Here, using single-molecule tracking, quantitative single-cell microscopy, and modeling, we show that genome dilution in *Escherichia coli* cells arrested for DNA replication results in a decrease in the concentration of active RNA polymerases and ribosomes. The resulting sub-linear scaling of total active RNA polymerases and ribosomes with cell size leads to sub-exponential growth, even within physiological cell sizes. Cell growth rate scales proportionally with the total number of active ribosomes in a DNA concentration-dependent manner. Tandem-mass-tag mass spectrometry experiments further reveal that a decrease in DNA-to-cell-volume ratio proportionally remodels the composition of the proteome with cell size independently of the environment. Altogether, our findings indicate that genome concentration is an important driver of exponential cell growth and a global modulator of proteome composition in *E. coli*. Comparison with studies on eukaryotic cells suggests DNA concentration-dependent scaling principles of gene expression across domains of life.

INTRODUCTION

Cells regulate the intracellular concentration of various proteins and macromolecules to modulate the rate of essential cellular processes, including growth. In bacteria, cell mass and volume typically double between division cycles. Proportionality between biosynthetic capacity and biomass accumulation results in exponential or near-exponential cell growth during the cell cycle (Campos et al., 2014; Schaechter et al., 1958; Siegal-Gaskins and Crosson, 2008; Taheri-Araghi et al., 2015; Wang

42 et al., 2010). What drives exponential growth has been a longstanding question in the microbiology
43 field (Belliveau et al., 2021; Churchward et al., 1982; Ecker and Schaechter, 1963; Zhurinsky et al.,
44 2010). Quantitative studies on model bacteria such as *Escherichia coli* place the concentration of
45 ribosomes and their kinetics as the principal rate-limiting factors (Belliveau et al., 2021; Bosdriesz et
46 al., 2015; Koch, 1988; Scott et al., 2014, 2010). Most other cellular components essential for growth
47 are estimated to be at least an order of magnitude above the level required for proper enzymatic
48 reactions (Belliveau et al., 2021), indicating that they are well in excess in terms of metabolic
49 concentrations. Thus, translation is generally seen as the rate-governing process for cellular growth.
50 While the translocation rate of ribosomes poses an inherent limit on the growth rate of the cell,
51 protein concentrations are predominantly set transcriptionally at the promoter level, with tight
52 coordination between transcription and translation (Balakrishnan et al., 2022).

53 Whereas the importance of ribosome concentration in growth rate determination has been
54 extensively studied, a potential role for genome concentration has received less attention. An early
55 population study on an *E. coli* thymine auxotroph proposed that global transcription is not limited by
56 the concentration of the genome but is instead constrained by the availability of RNA polymerases
57 (RNAPs) (Churchward et al., 1982). However, the potential impact of DNA concentration on
58 determining the growth rate of *E. coli* or other bacteria has, to our knowledge, not been formally
59 tested. Interestingly, *E. coli* and *Bacillus subtilis* have been shown to display small but reproducible
60 deviations from exponential growth during the division cycle (Kar et al., 2021; Nordholt et al., 2020),
61 with the growth rate increasing after the initiation of DNA replication under some conditions.
62 Furthermore, at the population level, these organisms initiate DNA replication at a fixed cell volume
63 (mass) per chromosomal origin of replication (*oriC*) across a wide range of nutrient and genetic

64 conditions (Donachie, 1968; Govers et al., 2024; Si et al., 2017; Zheng et al., 2016), suggesting that
65 DNA concentration is an important physiological parameter for these bacteria. In eukaryotes where
66 genome concentration is also tightly controlled (Ginzberg et al., 2015; Turner et al., 2012), a change
67 in DNA-to-cell-volume ratio has recently been demonstrated to remodel the proteome and promote
68 cellular senescence (Crozier et al., 2023; Foy et al., 2023; Lanz et al., 2023, 2022; Manohar et al., 2023;
69 Neurohr et al., 2019; Wilson et al., 2023).

70 In this study, we combined single-cell and single-molecule microscopy experiments with
71 tandem-mass-tag mass spectrometry and modeling to investigate the potential physiological role of
72 genome concentration in cell growth and proteome composition in *E. coli*.

73

74 **RESULTS**

75 **Growth rate correlates with the genome copy number in *E. coli.***

76 To examine the potential effect of DNA content on the growth rate of *E. coli*, we used two CRISPR
77 interference (CRISPRi) strains with arabinose-inducible control of expression of dCas9 (Li et al., 2016;
78 Si et al., 2017). One strain expressed a single guide RNA (sgRNA) against *oriC* where sequestration by
79 dCas9 binding prevents the initiation of DNA replication, producing cells with a single copy of the
80 chromosome (Figure 1A) (Si et al., 2017). These cells, referred to as "1N cells" below, grew into
81 filaments as a block in DNA replication prevents cell division, but not cell growth, from occurring (Carl,
82 1970; Si et al., 2017; Withers and Bernander, 1998). The second CRISPRi strain, which served as a
83 comparison, expressed a sgRNA against the cell division protein FtsZ. FtsZ depletion blocks cell division
84 while allowing DNA replication to proceed (Figure 1A) (Addinall et al., 1996; Li et al., 2016). Ongoing
85 growth resulted in filamenting cells with multiple replicating chromosomes, hereafter referred to as

86 “multi-N cells”. For both strains, we used time-lapse microscopy to monitor growth at the single-cell
87 level at 37°C in M9 minimal medium supplemented with glycerol, casamino acids, and thiamine
88 (M9glyCAAT). Cell area (A) was automatically detected from phase-contrast images using a deep
89 convolutional network (Wiktor et al., 2021), and the absolute growth rate ($\frac{dA}{dt}$) was determined by
90 calculating the difference in cell area between frames. The relative growth rate ($\frac{1}{A}\frac{dA}{dt}$), which is
91 constant for exponential growth, was calculated by dividing by the cell area. We chose to use cell area
92 rather than cell volume for growth rate measurements because cell area is what we measured in our
93 two-dimensional cell images, and the average cell width remained largely constant for 1N and multi-
94 N cells following CRISPRi induction (Figure 1 – figure supplement 1A). Furthermore, we found that
95 absolute and relative growth rates based on extracted cell volumes produced similar results (Figure 1
96 – figure supplement 1B-K) to those based on cell areas (Figure 1 and Figure 1 – figure supplement 2).
97 Therefore, we will report growth rate measurements based on cell areas hereafter.

98 For the CRISPRi *oriC* strain, we selected 1N cells that contained a single DNA object (nucleoid)
99 labeled by a mCherry fusion to the nucleoid-binding protein HupA (referred to as HU below). To
100 confirm this 1N chromosome designation, we used a CRISPRi *oriC* strain that expresses HU-CFP and
101 carries an *oriC*-proximal *parS* site labeled with ParB-mCherry (Figure 1 – figure supplement 3A), used
102 here to determine the number of nucleoids and chromosomal origins per cell. We found that 96 ± 1%
103 (mean ± standard deviation, SD, n = 3378 cells, three biological replicates) of cells with a single HU-
104 labeled nucleoid contained no more than one ParB-mCherry focus, indicative of a single *oriC*.

105 Using this methodology, we observed a significant difference in growth rate between 1N and
106 multi-N cells as shown in representative single-cell growth trajectories (Figure 1B) and in aggregated
107 absolute growth rate measurements (Figure 1C). In multi-N cells, the absolute growth rate rapidly

108 increased with cell area. For these cells, the scaling between absolute growth rate and cell size might
109 even be slightly greater than expected for exponential growth, as the relative growth rate was not
110 perfectly constant and mildly increased with cell area (Figure 1E). This slight increase would be
111 consistent with the super-exponential growth pattern previously described for wild-type (WT) cells
112 (Cylke and Banerjee, 2023; Kar et al., 2021). Multi-N cells grew identically to WT within the same cell
113 size range (Figure 1 – figure supplement 2). In contrast, 1N cells grew significantly slower than multi-
114 N-cells and their absolute growth rate only moderately increased with cell area, approaching an
115 apparent plateau at large cell sizes (Figure 1C-D). This sub-exponential growth resulted in a relative
116 growth rate that decreased with cell area (Figure 1E). The striking divergence in growth between 1N
117 and multi-N cells of the same size suggested that growth is dependent on DNA concentration. The
118 difference in growth rate between 1N and multi-N cells was already apparent in the physiological
119 range of cell sizes when compared to WT cells (Figure 1 – figure supplement 2), suggesting that growth
120 rate reduction occurs soon after DNA replication fails to initiate.

121 We ruled out that the slower growth of 1N cells was due to an induction of the SOS response
122 or to an increased level in the nucleotide alarmone (p)ppGpp, as inactivation of either stress pathway
123 (through deletion of *recA* or *spoT*/*relA*, respectively) in 1N cells made little to no difference to their
124 growth rate (Figure 1 – figure supplement 4). Furthermore, as an independent validation, we used an
125 orthogonal system to block DNA replication using the temperature-sensitive mutant *dnaC2*, which
126 encodes a deficient DNA helicase loader at the restrictive temperature of 37°C (Carl, 1970; Withers
127 and Bernander, 1998). We observed that the relationship between absolute growth rate and cell area
128 in *dnaC2* cells with a single nucleoid was similar to that of 1N cells produced by the CRISPRi *oriC* system
129 (Figure 1D and E).

130 We noticed that, even at the restrictive temperature, the *dnaC2* strain produced a sizeable
131 fraction of cells with more than one HU-mCherry-labelled nucleoid (Figure 1 – figure supplement 3B
132 and C), indicating that the temperate-sensitive effect on DNA replication is not fully penetrant. We
133 took advantage of this phenotypic "leakiness" to measure the growth rate of cells with different
134 numbers of nucleoids (and thus chromosomes) within the *dnaC2* population. We observed a notable
135 difference in growth rate between cells of 1, 2, and >2 nucleoids in the population, with each
136 additional nucleoid contributing to higher cellular growth at a given cell size (Figure 1F-G). This finding
137 is consistent with DNA-limited growth in which cellular growth rate increases with genome
138 concentration.

139 In the relatively nutrient-rich M9glyCAAT condition, WT cells at birth are expected to have
140 higher DNA content than 1N cells on average due to overlapping DNA replication (Fossum et al., 2007).
141 This difference in DNA concentration explains the lower absolute growth rate of 1N cells relative to
142 WT even at the smallest cell sizes (Figure 1- figure supplement 2). To examine whether cells are also
143 subject to DNA-limited growth when multi-fork DNA replication is rare or nonexistent, we measured
144 growth of 1N cells in two different nutrient-poor media, M9 glycerol (M9gly) and M9 L-alanine (M9ala).
145 In both conditions, the growth rate scaled slower with cell area in 1N cells relative to WT cells (Figure
146 1H-K). Here again, this difference in growth was apparent in the cell size range of WT cells, indicating
147 that the difference in growth rate is not simply the result of a non-physiological regime. Altogether,
148 our data suggest that in WT cells, the genome concentration is (or is close to be) limiting for growth
149 and that growth rate scales with ploidy.

150

151

152 **The concentration of ribosomal proteins remains relatively constant in DNA-diluted cells.**

153 Ribosome content is often proposed to explain the approximately exponential growth of biomass in
154 bacteria, with growth rate being directly proportional to ribosome concentration (Bremer and Dennis,
155 1996; Ecker and Schaechter, 1963; Scott et al., 2014, 2010). Therefore, we first quantified the
156 fluorescence concentration of a monomeric superfolder green fluorescent protein (msfGFP) fusion to
157 the ribosomal protein RpsB (expressed from the native chromosomal locus) in 1N and multi-N cells in
158 M9glyCAAT as a function of cell area. We found it to be almost identical between the two CRISPRi
159 strains and relatively constant across cell areas, regardless of DNA content (Figure 2A).

160 To exclude the possibility that the msfGFP tag altered the synthesis of RpsB or that this protein
161 behaved differently from other ribosomal proteins, we adapted a tandem-mass-tag (TMT) mass
162 spectrometry (MS) method recently developed to examine cell size-dependent proteome scaling in
163 yeast and human cells (Lanz et al., 2022). Note that for the CRISPRi *oriC* strain, a minority (~10-15%)
164 of cells have more than one nucleoid. These cells were excluded from the analysis of our single-cell
165 microscopy experiments. However, this could not be done for the TMT-MS experiments, which
166 provide population-level measurements. Therefore, for this TMT-MS section, we will refer to the
167 CRISPRi *oriC* cell population as "1N-rich" cells, instead of just "1N" cells. Using the TMT-MS approach,
168 we found that the relative concentration of all (54) high-abundance ribosomal proteins (including
169 untagged RpsB) remained approximately constant across all sizes of 1N-rich cells and was relatively
170 similar between 1N-rich and multi-N cells (Figure 2B). Only the ribosomal protein L31B, a stationary
171 phase paralog of the more prevalent exponential phase ribosomal protein L31A (Lilleorg et al., 2019),
172 displayed significant dilution in 1N cells (Dataset 1). Ribosomal protein concentration also appeared
173 to remain constant in 1N cells in nutrient-poor media based on RpsB-msfGFP fluorescence intensity

174 measurements in single cells (Figure 2 – figure supplement 1). Thus, the concentration of ribosomal
175 proteins does not explain the difference in growth rate between cells with different ploidy.
176
177 **The fraction of active ribosomes is reduced in DNA-diluted cells.**
178 To more specifically probe the translational activity of ribosomes in 1N cells, we performed single-
179 molecule tracking in live cells growing in M9glyCAAT. Ribosomes are expected to exhibit at least two
180 different dynamic states: slow mobility when active (i.e., engaged in translation on the mRNA, often
181 in polyribosome form), and faster mobility when inactive ribosomes (or ribosomal subunits) are
182 diffusing in the cytoplasm (Mohapatra and Weisshaar, 2018; Sanamrad et al., 2014). To track
183 ribosomes, we introduced a HaloTag fusion to RpsB at the endogenous locus and labeled the HaloTag
184 using the membrane-permeable Janelia Fluor 549 (JF549) fluorescent dye (Grimm et al., 2015). We
185 quantified the apparent diffusion coefficient (D_a) of single-molecule tracks in WT cells as well as in 1N
186 and multi-N cells at multiple time points following CRISPRi induction (Figure 2C). We found that the
187 distribution of D_a in multi-N cells of all sizes (~2-10 μm^2) was similar to that in WT cells despite the
188 considerable differences in cell sizes. In contrast, 1N cells displayed distributions clearly distinct from
189 WT and multi-N cells, gradually shifting toward faster mobilities (higher D_a) with increasing cell size.
190 This shift suggests that ribosome activity is altered in 1N cells.
191 Gaussian fitting of the D_a logarithmic data in WT cells revealed two predominant dynamic
192 states of ribosomes: a slow-diffusing and a fast-diffusing state, representing 77 ± 1% (mean ± standard
193 error of the mean (SEM)) and 20 ± 1% of the ribosome population, respectively (Figure 2D). In addition,
194 we observed a small fraction (3.2 ± 0.5%) of faster-moving molecules with D_a expected for freely-
195 diffusing proteins (Banaz et al., 2019; Elowitz et al., 1999), likely indicative of a small pool of free RpsB-

196 HaloTag proteins (i.e., not assembled into ribosomes). To confirm that the slow-diffusing fraction
197 corresponded to translationally active ribosomes, we showed that this fraction nearly vanished (down
198 to 1.10 ± 0.02%) when cells were depleted of mRNAs following 30 min treatment with the
199 transcription inhibitor rifampicin (Figure 2 – figure supplement 2). The estimated fraction (~77%) of
200 active ribosomes in untreated cells was in good agreement with previous single-molecule and
201 biochemical studies under these growth conditions (Blundell and Wild, 1971; Mohapatra and
202 Weisshaar, 2018; Phillips et al., 1969; Sanamrad et al., 2014).

203 Upon fitting the D_a values of ribosomes in 1N cells of different sizes (Figure 2E), we observed
204 a significant reduction in the slow-diffusing ribosome population (Figure 2 – figure supplement 3).
205 Quantification of the active (slow-diffusing) ribosome fraction per cell revealed that 1N cells have
206 overall lower ribosome activity than WT cells, and that ribosome activity decreases monotonically
207 with increasing cell area (Figure 2F). In contrast, ribosome activity in multi-N cells remained the same
208 as in WT across different cell sizes (Figure 2G). The reduction in fraction of active ribosomes was less
209 pronounced in 1N cells growing in M9gly and M9ala (Figure 2 – figure supplement 4), consistent with
210 the smaller deviation in growth rate between 1N and WT cells (Figure 1H-K).

211 To estimate the total number of active ribosomes per cell in M9glyCAAT, we multiplied the
212 total amount of ribosomes by the fraction of active ribosomes and plotted the result as a function of
213 cell area (Figure 2H). We found that the difference in the total number of active ribosomes between
214 1N and multi-N cells matches the observed difference in growth rate in M9glyCAAT (Figure 2H),
215 indicating cell growth rate is directly proportional to the increase in total active ribosomes. We also
216 estimated the total number of active ribosomes in WT and 1N cells in M9gly and M9ala, where, overall,
217 we observed similar trends (Figure 2 – figure supplement 4G-H). Altogether, the results are consistent

218 with the hypothesis that DNA limitation decreases ribosome activity, which in turn reduces the growth
219 rate.
220
221 **DNA dilution reduces the activity of RNA polymerases.**
222 We reasoned that the observed changes in ribosome activity in 1N cells may reflect the available
223 mRNA pool in cells. If true, we would expect the total activity of RNAPs to be reduced in 1N cells. In
224 cells, the total activity of RNAPs is determined by the concentration of RNAPs multiplied by the
225 fraction of active RNAPs. Therefore, we first determined whether RNAP concentration was lower in
226 1N cells relative to multi-N cells in M9glyCAAT by quantifying the fluorescence intensity of a functional
227 fusion of YFP to the RNAP β' subunit (encoded by *rpoC*) expressed from its native chromosomal locus.
228 As expected, RNAP concentration remained constant in multi-N cells (Figure 3A). In 1N cells, the RNAP
229 concentration increased with cell size (Figure 3A), the opposite of what would be expected to explain
230 the growth rate defect. We confirmed this increasing trend in concentration for other protein subunits
231 of the core RNAP and the primary sigma factor σ^{70} (encoded by *rpoD*) using TMT-MS (Figure 3B),
232 clearly demonstrating that the abundance of RNAPs was not the limiting factor. RNAP concentration
233 also increased, albeit to a lesser degree, in 1N cells in nutrient-poor media based on fluorescence
234 intensity measurements (Figure 3 – figure supplement 1).
235 To quantify RNAP activity in 1N and multi-N cells, we performed single-molecule tracking in
236 live cells in M9glyCAAT using a functional fusion of HaloTag to the β' protein subunit RpoC labeled
237 with the JF549 dye. As expected, the D_a values of RpoC-HaloTag in multi-N cells were distributed
238 similarly to those in WT cells (Figure 3C). In contrast, the distribution in 1N cells changed gradually
239 toward higher D_a values (faster mobility) with increasing cell size (Figure 3C).

240 As with ribosomes, RNAPs primarily exhibited two major states of diffusivity (Figure 3D): a
241 slower-diffusing fraction (49 ± 4%; mean ± SEM) and a faster-diffusing fraction (49 ± 4%), likely
242 representing transcriptionally active RNAPs and inactive, diffusing RNAPs, respectively. A small
243 fraction of RpoC-HaloTag (2 ± 0.1%) diffused very fast, with D_a values expected for free proteins,
244 suggesting that it reflects the few β' proteins not assembled into the RNAP core complex. Using
245 rifampicin treatment, we confirmed that the slowest state corresponded to RNAPs actively engaged
246 in transcription (Figure 3 – figure supplement 2). In these rifampicin-treated cells, the slow-diffusing
247 fraction was reduced to 13 ± 4%. Rifampicin does not prevent promoter binding or open complex
248 formation and instead blocks transcription elongation following the synthesis of 3-nucleotide-long
249 RNAs (Campbell et al., 2001). Thus, the observation that slow-moving RNAPs did not completely
250 disappear after rifampicin treatment is consistent with the mechanism of action of the drug, leaving
251 a fraction of RNAPs bound at promoter sites.

252 Unlike in WT and multi-N cells, the fraction of active RNAPs in 1N cells decreased
253 monotonically with increasing cell area in all tested media (Figure 3F-G and Figure 3 – figure
254 supplements 3 and 4). However, because the RNAP concentration simultaneously increased in 1N
255 cells, it was possible that the total amount of active RNAP, which is the relevant metric of transcription
256 activity, remained equal to that of multi-N cells. By calculating the total amount of active RNAPs, we
257 showed that the decrease in active fraction in 1N cells was not the mere result of the increase in RNAP
258 concentration. Indeed, in M9glyCAAT, the total amount of active RNAPs hardly increased with cell size
259 in 1N cells whereas it increased proportionally with cell size in both multi-N and WT cells (Figure 3H).
260 This was also true in M9gly and M9ala (Figure 3 – figure supplement 4G-H). The reduction in the total

261 amount of active RNAPs was also readily apparent in 1N cells within the range of WT cell sizes (Figure
262 3H and Figure 3 – figure supplement 4G-H).

263 A recent study has shown that the intracellular concentration of Rsd, the anti-sigma factor of
264 σ^{70}, increases in WT cells under slower growth conditions, causing a reduction in global mRNA
265 synthesis (Balakrishnan et al., 2022). Therefore, we verified that the concentration of Rsd remains
266 approximately constant in both 1N-rich and multi-N cells based on our TMT-MS data (Figure 3 – figure
267 supplement 5), eliminating Rsd as possible source of reduced RNAP activity in 1N cells. Instead, our
268 data supports the notion that substrate (DNA) limitation leads to a reduced transcription rate, which
269 would reduce the pool of mRNAs available for ribosomes.

270

271 **DNA dilution can result in sub-exponential growth through mRNA limitation.**

272 In a previous theoretical study, Lin and Amir (2018) considered distinct scenarios for gene expression.
273 Their model predicted that if DNA and mRNAs are in excess, cells display exponential growth, whereas
274 if DNA and mRNAs are limiting, cells will adopt linear growth. Our experiments showed that 1N cells
275 converge toward linear growth (toward slope = 0 in Figure 1C, H, and J), though the complete
276 transition to linear growth required a large decrease in DNA concentration. To quantitatively examine
277 this transition from exponential to linear growth through DNA dilution, we developed two
278 deterministic ordinary differential equation (ODE) models of the flow of genetic information that
279 include parameters for the fractions of active RNAPs and ribosomes. In these models, the dynamics
280 of mRNA (X) and protein (Y) numbers in the cell are described by

281 $$\frac{dX}{dt} = r_1 \alpha_{RNAP}(X, Y)Y - \delta X \qquad \text{(Eq.1)}$$

282 $$\frac{dY}{dt} = r_2 \alpha_{ribo}(X, Y)Y \qquad \text{(Eq.2)}$$

283 Where r_1 is the bulk transcription rate normalized by the total protein number, r_2 is the bulk
284 translation rate normalized by the total protein number, $\alpha_{RNAP}(X,Y)$ is the fraction of active RNAPs,
285 δ is the mRNA degradation rate, $\alpha_{ribo}(X,Y)$ is the fraction of active ribosomes, and $\frac{dY}{dt}$ corresponds
286 to the absolute growth rate. For simplicity, we assumed that the protein degradation is negligible and
287 that the cell volume and the number of rRNAs grow proportional to protein Y (Balakrishnan et al.,
288 2022; Lin and Amir, 2018). For detailed description and estimation of the model parameters, see
289 Table 1 and Appendix 1.

290 Based on the function form of $\alpha_{RNAP}(X,Y)$, we consider two ODE model variants. Model A
291 examined the effect of DNA limitation with minimal mathematical complexity by assuming that the
292 proteome does not change (see Materials and Methods). Model B considered RNAP kinetics (with
293 three different RNAP states: free, promoter-bound, and transcribing) and took into consideration the
294 experimentally observed increase in RNAP concentration in 1N cells (Figure 3A-B, see Materials and
295 Methods and Appendix 2). For both models, α_{RNAP} depended on DNA concentration. In 1N cells, the
296 DNA amount was fixed to 1 genome while it scaled with cell volume in multi-N cells. We then used
297 both models to perform simulations and compared the results to our measurements, starting with
298 parameter values extracted or estimated from the *E. coli* literature (Table 2). The parameters were
299 then optimized to fit six experimental datasets simultaneously: cell growth rate, the fraction of active
300 RNAPs, and the fraction of active ribosomes in both 1N and multi-N cells in M9glyCAAT (see Materials
301 and Methods and Appendix 3).

302 As shown in Figure 4A-D (model A) and Figure 4 – figure supplement 1 (model B), both models
303 performed similarly after parameter optimization. While the model curves (solid lines) did not exactly
304 match the average behavior of our experimental results (open squares), they displayed similar trends

305 and fell within the variance of the single-cell data (dots). The models showed that multi-N cells (blue)
306 display balanced exponential growth while the 1N cells (yellow) exhibit sub-exponential growth
307 (Figure 4A and Figure 4 – figure supplement 1A), consistent with experiments. At the same time, both
308 models recapitulated the observed experimental trends in active fractions of both ribosomes and
309 RNAPs, which remained constant in multi-N cells while decaying gradually with DNA concentration in
310 1N cells (Figure 4B-D and Figure 4 – figure supplement 1B-D).

311 In the absence of published values for the RNAP kinetic constants in nutrient-poor media, we
312 only used the simpler model A for the M9gly and M9ala conditions. Here again, the model reproduced
313 the trends for the experimental measurements of WT cells (gray) and 1N cells (yellow) (Figure 4 –
314 figure supplement 2), with one notable deviation. At cell birth, the curves of fractions of active RNAPs
315 and ribosomes for 1N cells started slightly higher than the ones for WT cells due to a limitation of our
316 ODE model, which uses the average concentration of genome and does not include DNA replication
317 dynamics.

318 The simulation results of 1N cells suggest the following cascade of events when DNA is limiting.
319 Lower DNA concentration results in fewer substrates for RNAPs, which reduces the transcription rate.
320 This results in a decrease in mRNA concentration (Figure 4E). As mRNAs become limiting, the fraction
321 of ribosomes engaged in translation decreases. This, in turn, decreases the rate in bulk protein
322 synthesis, which decreases the relative growth rate. The greater the DNA dilution (through cell
323 growth), the more severe the downstream effects become, explaining the decay in relative growth
324 rate in 1N cells (Figure 4E).

325 Since the models predicted a reduced mRNA pool in 1N cells, we performed live-cell staining
326 with SYTO RNASelect (Wu et al., 2020), a fluorogenic RNA-specific dye that primarily (~70% of the

327 signal) binds mRNAs in *E. coli* based on rifampicin treatment (Bakshi et al., 2014). In our RNASelect
328 staining experiments, we mixed 1N cells with multi-N cells of similar size ranges prior to incubation
329 with the dye to mitigate variability in staining. We next imaged the mixed populations and
330 distinguished 1N cells from multi-N cells by examining the difference in nucleoid number (one vs.
331 multiple) per cell (Figure 4F). Single cells were then sampled to ensure that the cell area distributions
332 of the two populations perfectly matched (Figure 4 – figure supplement 3). Comparison between the
333 two sampled populations from five independent experiments revealed a reduced concentration of
334 RNASelect signal (by ~50%) in 1N cells relative to multi-N cells for a cell size range of 4 to 10 μm^2
335 (Figure 4G-H). We also found that the RNASelect concentration ratio between 1N and multi-N cells
336 decreased exponentially with increasing cell area and thus DNA dilution (Figure 4I), in line with the
337 model prediction (Figure 4E). Furthermore, both the model (Figure 4E) and our experimental findings
338 (Figure 4I) suggest that the effects of DNA limitation on the mRNA concentration already appear at
339 physiological cell area ranges (between 2 and 3 μm^2).

340 To verify that the decrease in RNASelect signal in 1N cells was not caused by a global change
341 in membrane permeability to small molecules, we performed similar staining experiments with the
342 HaloTag dye JF549 in CRISPRi strains expressing RpoC-HaloTag (Figure 4 – figure supplement 4A-B).
343 Because RpoC concentration increases with cell size in 1N cells relative to multi-N cells (Figure 3A-B),
344 we expected a similar increase in the ratio of JF549 signal between these two cell types if the
345 membrane permeability to small molecules remained unchanged. This is indeed what we observed
346 (Figure 4 – figure supplement 4C-E). Hence the RNASelect results are consistent with a reduced mRNA
347 concentration in 1N cells caused by DNA dilution and reduced global transcription activity.

348

349 **Genome dilution incrementally changes the composition of the proteome.**

350 The fact that the relative concentrations of ribosomal proteins and RNAP subunits scaled differently
351 with cell area in 1N cells (Figures 2A-B and 3A-B) indicated that all genes are not equally impacted by
352 DNA dilution. In yeast and mammalian cells, a decrease in the DNA-per-volume ratio has recently
353 been demonstrated to alter the composition of the proteome, with some proteins increasing in
354 relative concentration while others become comparatively more diluted (Lanz et al., 2023, 2022). To
355 examine whether this effect may be conserved across domains of life, we used our proteomic TMT-
356 MS data on the CRISPRi strains to quantify the relative concentration of each detected protein across
357 cell areas following DNA replication or cell division arrest. For each protein, we calculated the relative
358 change in concentration against the relative change in cell size through regression fitting, yielding a
359 slope value. A slope of zero indicates that the relative concentration of a protein remains constant
360 whereas a slope of -1 (or 1) means that the relative concentration is decreasing (or increasing) by two-
361 fold with each cell size doubling (Figure 5A).

362 We found that the slope distribution was highly reproducible between biological replicates
363 (Figure 5 – figure supplement 1A-B) but drastically different between 1N-rich cells and multi-N cells
364 (Figure 5B, Dataset 1). In the control multi-N cells where the genome concentration does not change
365 with cell growth, the concentration of ~94% of the detected proteins (2217/2360) remained roughly
366 constant, with their concentrations decreasing or increasing by less than 20% per cell size doubling
367 (i.e., slopes > -0.2 or < 0.2; Figure 5B and Dataset 1). This indicates that protein amounts largely scale
368 with cell size, as generally assumed. However, in 1N-rich cells where the genome dilutes with cell
369 growth, the proportion of detected proteins that maintained similarly constant concentrations across
370 cell areas (i.e., slopes > -0.2 or < 0.2) dropped to ~37% (859/2360) (Figure 5B and Dataset 1). A

371 principal component analysis on the relative protein concentration during cell growth confirmed that
372 the relative proteome composition changes proportionally with genome dilution (1N-rich cells),
373 whereas it remains constant when the DNA-to-cell volume is maintained (multi-N cells) (Figure 5C).

374 Interestingly, for 1N-rich cells, we also observed a slight yet significant positive correlation
375 (Spearman $\rho = 0.23$, p-value $< 10^{-10}$, for genes within 1.35 Mb from *oriC*) between protein slope and
376 the gene distance from *oriC* (Figure 5D). In other words, genes closer to *oriC* were more likely to
377 encode proteins that dilute during DNA-limited growth (protein slope < 0) compared to distal genes
378 (Figure 5D). This was irrespective of their total protein abundance based on summed ion intensities
379 normalized by protein sequence lengths (Figure 5E). This may suggest the existence of a mechanism
380 that compensates for the gene dosage associated with DNA replication.

381 To examine whether the proteome scaling behavior stems from changes in mRNA levels, we
382 performed transcriptomic (RNA-seq) analysis on two biological replicates of 1N-rich cells at different
383 time points after induction of DNA replication arrest. The two replicates were strongly correlated at
384 the transcript level (Spearman $\rho = 0.91$, Figure 5 – figure supplement 1C). We also found a strong
385 correlation in scaling behavior with cell area between mRNAs and proteins across the genome
386 (Spearman $\rho = 0.76$, Figure 5F and Dataset 2), indicating that most of the changes in protein levels
387 observed upon genome dilution take place at the mRNA level.

388

389 **DISCUSSION**

390 In this study, we show that genome concentration acts as a rate-limiting factor for exponential cellular
391 growth and a modulator of proteome composition in *E. coli*. These roles for genome concentration
392 help explain why the timing of DNA replication is so robustly linked to cell volume across

393 environmental and genetic conditions that affect cell size (Donachie, 1968; Govers et al., 2024; Si et
394 al., 2017; Zheng et al., 2016).

395 Our data suggest that DNA limitation in 1N cells affects cell growth rate through modulation
396 of downstream transcription and translation activities (Figures 2-4 and associated figure supplements).
397 As a result of growth-induced dilution, the genome becomes increasingly limiting as a template,
398 decreasing the fraction of active RNAPs (Figure 3). This indicates a sub-linear scaling of global
399 transcription relative to the cell size. We propose that this reduced transcription activity in
400 comparison to cells undergoing DNA replication results in a gradual decrease in total mRNA
401 concentration (Figure 4E-G). Reduced mRNA availability would cause a decrease in the fraction of
402 ribosomes engaged in translation (Figure 2F and Figure 2 – supplement 4), which would, in turn, lead
403 to sub-linear scaling of global protein synthesis and absolute growth rate with cell size (Figure 2H and
404 Figure 2 – supplement 4). It is also possible that the cumulative effect of small changes in proteome
405 composition in 1N cells contributes to their growth rate defect.

406 The growth rate dependency on genome concentration is unlikely to be a particularity of *E.*
407 *coli*, as we also observed a divergence in absolute and relative growth rates with increasing cell area
408 between 1N and multi-N cells of *Caulobacter crescentus* (Figure 1 – supplement 6A and B). In this
409 organism, filamenting 1N and multi-N cells were generated by depleting the DNA replication initiation
410 factor DnaA (Gorbatyuk and Marczynski, 2001) and the cell division protein FtsZ (Wang et al., 2001),
411 respectively. The 1N versus multi-N designation was confirmed by visualizing the number of
412 chromosomal origins of replication (one versus multiple) per cell using the *parS*/ParB-eCFP labeling
413 system (Figure 1 –supplement 6C). The fact that DNA limitation for cellular growth was also observed
414 in *C. crescentus* is significant not only because this bacterium is distantly related to *E. coli*, but also

415 because it has a different pattern of cell wall growth and distinct control mechanisms of DNA
416 replication (Aaron et al., 2007; Banerjee et al., 2017; Frandi and Collier, 2019; Lasker et al., 2016;
417 Terrana and Newton, 1975). This suggests that DNA concentration may be a prevalent growth
418 constraint across bacterial species.

419 We found that even a relatively small dilution in DNA concentration—as expected in DNA
420 replication-arrested cells that are still within or close to physiological sizes—results in growth rate
421 reduction in *E. coli* and *C. crescentus* (Figure 1 and Figure 1 – supplements 2 and 6). Thus, under our
422 standard growth conditions, cells appear to live at the cusp of DNA limitation for cellular growth. This
423 suggests that cells make enough—but not too much—DNA, presumably because DNA replication is a
424 costly process that represents a significant fraction (~6% in minimal media) of the cellular energy
425 budget (Neidhardt et al., 1990). What may be the implications of living at the cusp of DNA limitation
426 in bacteria? While *E. coli* carefully controls its DNA concentration across various conditions and
427 growth rates at the population level (Donachie, 1968; Govers et al., 2024; Si et al., 2017; Zheng et al.,
428 2016), there remains some variability in DNA concentration at the single-cell level, with some cells
429 initiating DNA replication at smaller or larger cell volumes than others (Si et al., 2019; Witz et al., 2019).
430 It will be interesting to explore in future studies whether this variability contributes to the known
431 growth rate heterogeneity across isogenic cells (Lin and Jacobs-Wagner, 2022; Wang et al., 2010). It
432 is also tempting to speculate that changes in DNA concentration may, at least in part, contribute to
433 the deviations from exponential growth that have been reported during the division cycle of *B. subtilis*,
434 *E. coli,* and stalked *C. crescentus* progeny (Banerjee et al., 2017; Kar et al., 2021; Nordholt et al., 2020;
435 Reshes et al., 2008). More substantial forms of DNA dilution may occur under other circumstances as
436 well. *C. crescentus* cells in freshwater lakes often form long filaments during algal blooms in the

437 summer months (Heinrich et al., 2019). These filament cells are thought to be the result of a DNA
438 replication arrest in response to the combination of an alkaline pH, a depletion in phosphate, and an
439 excess in ammonium (Heinrich et al., 2019). Another example is illustrated by the Lyme disease agent
440 *Borrelia burgdorferi*. This pathogen, which forms long polyploid cells during exponential growth,
441 experiences a progressive decrease in genome concentration (up to eightfold) in stationary phase
442 cultures through the gradual loss of genome copies (Takacs et al., 2022).

443 Comparison with studies on eukaryotic cells suggests conservation of gene expression
444 principles across domains of life. For instance, in yeast, it has been shown that the global transcription
445 rate in G1-arrested cells is higher in diploids than haploids of similar sizes (Swaffer et al., 2023),
446 consistent with DNA concentration being a limiting factor for transcription. Furthermore, in both yeast
447 and mammalian cells, small G1-arrested cells display higher growth rate (or global RNA or protein
448 synthesis rate) per cell volume than large ones that have exceeded a certain volume (Cadart et al.,
449 2018; Liu et al., 2022; Neurohr et al., 2019; Zatulovskiy et al., 2022). This is likely due to a change in
450 genome concentration rather than a change in cell volume, as the relative growth rate is unaffected
451 in very large cells as long as they undergo a proportional increase in ploidy (Mu et al., 2020).

452 In yeast cells, an increase in RNAP II gene occupancy combined with a decrease in mRNA
453 turnover helps mitigate DNA dilution on global transcription activities up to a certain cell volume
454 beyond which the compensation breaks down (Swaffer et al., 2023; Zhurinsky et al., 2010). Such
455 buffering activities, which are consistent with model predictions (Figure 4 – figure supplement 5)
456 (Swaffer et al., 2023), may also be at play in bacteria, potentially in a growth medium-dependent
457 manner. For example, in our *E. coli* experiments, we noted that the global transcriptional activity (total
458 amount of active RNAPs) strongly deviated from proportional scaling with cell size in 1N cells

459 compared to WT and multi-N cells in all tested medium conditions (Figure 3H and Figure 3 –
460 supplement 4G-H). This indicates that the genome content limits transcription. However, the global
461 translation activity (total amount of active ribosomes) only strongly deviated from proportional
462 scaling with cell sizes in 1N cells growing in the relatively rich medium (M9glyCAAT) condition (Figure
463 2H). In poor media (M9gly and M9ala), the deviation was far less pronounced (Figure 2H and Figure 2
464 – supplement 4G-H), suggesting that a decrease in mRNA turnover and/or an increase in ribosome
465 occupancy per transcript partially buffer(s) DNA limitation on transcription in poor media.

466 Another remarkable similarity between bacteria and eukaryotes is the effect of genome
467 concentration on proteome composition. While protein abundance is typically assumed to scale with
468 cell size in bacteria, we found that this is true at the proteome level only when ploidy also scales
469 (Figure 5). This requirement was also recently shown in yeast and mammalian cells (Lanz et al., 2023,
470 2022). This conservation in scaling principle further highlights the importance of genome
471 concentration in controlling protein expression.

472 At the GO term level, we did not identify any specific trends in proteome changes (Dataset 1).
473 In eukaryotic cells, histones are known to scale in proportion with DNA rather than cell size (Claude
474 et al., 2021; Swaffer et al., 2021; Wiśniewski et al., 2014). As a result, their concentration
475 proportionally decreases (i.e., slope = -1) with growth in G1 phase. In *E. coli*, the relative abundance
476 of some nucleoid-associated proteins (H-NS, HU and Dps) decreased with genome dilution, while
477 others (IHF and Fis) displayed superscaling behavior (Figure 5 – supplement 2). What determines the
478 scaling behavior of proteins is not clear. We found that, in *E. coli*, the alteration in proteome
479 composition largely occurs at the mRNA level (Figure 5F) and partially involves chromosomal
480 positioning (Figure 5D).

481 Finally, given the prevalent use of *E. coli* in the biotechnological world, we hope that our
482 findings will be helpful to future bioengineering studies and growth rate optimization efforts. We
483 show that protein content and cellular growth depend on the ploidy-to-cell volume ratio (Figures 1
484 and 5). As such, models of protein expression that take into consideration the DNA concentration and
485 the active number of RNAPs and ribosomes could provide a starting point to identify the parameter
486 space that leads to growth rate improvement.
487

488 **MATERIALS AND METHODS**

489 **Bacterial strains and growth conditions**

490 Bacterial strains and their construction can be found in Table 3. Oligomers used for polymerase chain
491 reaction (PCR) are listed in Table 4. Transductions and Gibson assemblies were performed as
492 described previously (Ely, 1991; Thomason et al., 2007).

493 *E. coli* strains were grown at 37°C in M9 minimal media with different supplements: 0.2%
494 glycerol, 0.1% casamino acids and 1 µg/ml thiamine (M9glyCAAT); 0.2% glycerol (M9gly); or 0.2% L-
495 alanine (M9ala). For microscopy, cells were grown in culture tubes to stationary phase, diluted
496 10,000-fold, and grown until they reached an optical density (OD_{600}) between 0.05 and 0.2. For
497 imaging, cells were then spotted onto a 1% agarose pad on a glass slide prepared with the appropriate
498 M9 medium and covered by a #1.5 thickness coverslip.

499 For time-lapse microscopy experiments with the CRISPRi strains (Li et al., 2016), the cells were
500 induced by adding L-arabinose (0.2%) to liquid cultures after which a sample (~1 µl) was immediately
501 collected and spotted on an agarose pad containing the appropriate growth medium supplemented
502 with 0.2% L-arabinose. This was promptly followed by imaging of individual cells. To determine the

503 1N status of CRISPRi *oriC* cells, we monitored the last division and number of nucleoids based on HU-
504 mCherry fluorescence. In Figure 1B, the time point "0 min" refers to the time when cells have reached
505 the 1N status.

506 For population microscopy experiments with the CRISPRi strains, the cells were induced with
507 0.2% L-arabinose and allowed to grow in normal conditions until a specific time point (depending on
508 the growth medium and strain) was reached, after which the cells were spotted on an agarose pad
509 containing the appropriate growth medium and 0.2% L-arabinose, and imaged (see information for
510 each experiment in the corresponding Figure). Note that the CRISPRi strains do not metabolize
511 arabinose due to the *araBAD* deletion.

512 For the TMT-MS experiments, CRISPRi *oriC* (SJ_XTL676) cells were supplemented with 0.2% L-
513 arabinose and allowed to grow in liquid M9glyCAAT cultures at 37°C for 0, 120, 180, 240 and 300 min
514 before harvesting, while CRISPRi *ftsZ* (SJ_XTL229) cells were collected after 0, 60, and 120 min after
515 arabinose addition. For RNAseq experiments, CRISPRi *oriC* (SJ_XTL676) cells were supplemented with
516 0.2% L-arabinose and allowed to grow liquid M9glyCAAT cultures 37°C for 60, 120 200, and 240 min
517 before harvesting.

518 Strains carrying the *dnaC2* mutation were grown at a permissive temperature of 30°C and then
519 shifted to 37°C to block replication initiation. Transcription inhibition and mRNA depletion were
520 achieved by exposing cells to 200 µg/ml rifampicin for 30 min before spotting cells onto a 1% agarose
521 pad containing the appropriate M9 medium and rifampicin concentration. The HaloTag was labeled
522 with Janelia Fluor 549 (JF549) ligand (Grimm et al., 2015) as described previously (Banaz et al., 2019).
523 Briefly, cells were incubated with 2.5 µM of the JF549 ligand for 30 min while shaking, washed 5 times

524 with growth medium, and allowed to recover for several generations (while remaining in exponential
525 phase) prior to imaging.

526 *C. crescentus* strains were grown at 22˚C in PYE (2 g/L bacto-peptone, 1 g/L yeast extract, 1
527 mM $MgSO_4$, 0.5 mM $CaCl_2$) supplemented with 0.03% xylose to induce production of the essential
528 protein FtsZ (Wang et al., 2001) or DnaA (Gorbatyuk and Marczynski, 2001). For microscopy, cells
529 were grown in overnight cultures, then diluted at least 1:10,000 in fresh medium and grown to
530 exponential phase (OD_{660} nm < 0.3). To induce cell filamentation by depleting FtsZ or DnaA, xylose
531 was removed from the medium by pelleting cells, washing twice with PYE, and resuspending in fresh
532 PYE. Cultures were then allowed to grow for an additional 30 min to allow ongoing cell division cycles
533 to complete before spotting on 1% agarose pads containing PYE but lacking xylose to deplete FtsZ or
534 DnaA. To estimate the concentration of fluorescently-labeled ribosomes and RNAPs by fluorescence
535 microscopy, cultures were sampled at 0, 4, 8, and sometimes 12 h following xylose depletion with 30
536 min outgrowth to allow late predivisional cells time to divide before spotting. For timelapse
537 microscopy, new pads were spotted with cells from the original culture at 0, 4, 8, and sometimes 12
538 h following xylose removal with 30 min outgrowth in a liquid PYE medium.

539

540 **Epifluorescence microscopy**

541 For *E. coli*, phase contrast and fluorescence imaging (except for the RpoC-HaloTag-JF549
542 epifluorescence experiment), were performed on a Nikon Ti2 microscope equipped with a Perfect
543 Focus System, a 100x Plan Apo λ 1.45 NA oil immersion objective, a motorized stage, a Prime BSI
544 sCMOS camera (Photometrics), and a temperature chamber (Okolabs). Fluorescence emission was
545 collected during a 100 or 200 ms exposure time provided by a Spectra III Light Engine LED excitation

546 source (Lumencor): mCherry – 594 nm excitation, DAPI/FITC/TxRed filter cube (polychroic FF-
547 409/493/596-Di02, triple-pass emitter FF-1-432/523/702-25); GFP and SYTO RNASelect – 488 nm
548 excitation, DAPI/FITC/TxRed polychroic filter cube, and an ET525/50M emission filter; YFP – 514 nm
549 excitation, CFP/YFP/mCherry filter cube (polychroic FF-459/526/596-Di01, triple-pass emitter FF-1-
550 475/543/702-25), and a FF02-525/40-25 emission filter. The microscope was controlled using NIS-
551 Elements AR. For time-lapse imaging, phase images were collected every 5 min.

552 Epifluorescence snapshots of RpoC-HaloTag-JF549 were taken using a Nikon Ti microscope,
553 equipped with a Perfect Focus System, a 100x Plan Apo λ 1.45 NA oil immersion objective, a motorized
554 stage, an ORCA Flash 4.0 camera (Hamamatsu) and a temperature chamber (Okolabs). Fluorescence
555 emission was collected during a 200 ms exposure time provided by a Sola solid state white light source
556 (Lumencor) and a Cy3 filter cube (excitation AT545/25x, dicrhoic T565lpxr, emission ET605/70m). The
557 microscope was controlled using NIS-Elements AR.

558 For *C. crescentus*, phase contrast and fluorescence imaging were performed on a Nikon Ti-E
559 microscope equipped with a Perfect Focus System, a 100x Plan Apo λ 1.45 NA oil immersion objective,
560 a motorized stage, an Orca-Flash4.0 V2 142 CMOS camera (Hamamatsu) at room temperature.
561 Chroma filter sets were used to acquire fluorescence images: CFP (excitation ET436/20x, dichroic
562 T455lp, emission ET480/40m) and mCherry (excitation ET560/40x, dichroic T585lpxr, emission
563 ET630/75m). The microscope was controlled using NIS-Elements AR. For time-lapse imaging, phase
564 images were collected every 2.5 min.

565

566

567

568 **Photoactivated localization microscopy**

569 For single-molecule photoactivated localization (PALM) microscopy, coverslips were plasma-cleaned
570 of background fluorescent particles using a plasma cleaner (PDC-32G, Harrick Plasma). Live cell PALM
571 microscopy was performed on a Nikon N-STORM microscope equipped with a Perfect Focus System
572 and a motorized stage. JF549 fluorescence was measured using an iXon3 DU 897 EMCCD camera
573 (Andor) and excited from a 50 mW 561 nm laser (MLC400B laser unit, Agilent) with 50% transmission.
574 The laser was focused through a 100x Apo TIRF 1.49 NA oil immersion objective (Nikon) onto the
575 sample using an angle for highly inclined thin illumination to reduce background fluorescence
576 (Tokunaga et al., 2008). Fluorescence emission was filtered by a C-N Storm 405/488/561/647 laser
577 quad set. Transmission illumination was used to gather brightfield images. PALM movies of 20,000
578 frames were acquired with continuous laser illumination and a camera frame rate of 10.7 ms.

579

580 **SYTO RNASelect staining experiments**

581 In order to compare the mRNA concentration between 1N and multi-N cells, exponentially growing
582 CJW7576 (CRISPRi *ftsZ*) and CJW7457 (CRISPRi *oriC*) cells were stained with the fluorogenic SYTO
583 RNASelect dye (Invitrogen™, S7576) after CRISPRi induction with 0.2% L-arabinose. To ensure
584 overlapping cell area distributions in the absence of cell division, considering the measured growth
585 rate differences between the 1N and multi-N cells, CRISPRi *oriC* was was induced for 3.5 h whereas
586 CRISPRi *ftsZ* was induced for 1.5 h. Then, the two populations were mixed at equal optical densities
587 (OD_{600}) and stained with 0.5 µM SYTO RNASelect for 15 min at 37°C with shaking. For each staining, a
588 fresh 5µM SYTO RNASelect stock was prepared in L-arabinose-containing medium. Stained cells (~0.5

589 μL) were spotted on a 1% agarose pad prepared with the same growth medium with L-arabinose for
590 imaging. Five biological replicates were performed.
591
592 **RpoC-HaloTag-JF549 staining experiments for epifluorescence snapshots**
593 For Figure 4 – supplement 5, CRISPRi *oriC* in CJW7520 cells was induced for 3.5 h whereas CRISPRi *ftsZ*
594 (CJW7527) was induced for 1.5 h with 0.2% L-arabinose to obtain a similar range of cell sizes for
595 imaging. Then the two populations were mixed at equal optical densities (OD_{600}) and stained with 2.5
596 μM JF549 at 37°C for 30 min with shaking. The mixed cells were then washed three times with L-
597 arabinose-containing (0.2%) medium. All washes were performed at 4°C, using ice-cold medium to
598 block cell growth and avoid the dilution of the dye. Then, the cells (~0.5 μL) were spotted on a 1%
599 agarose pad prepared with the same L-arabinose-containing growth medium for imaging. Two
600 biological replicates were performed.
601
602 **Image processing and data analysis**
603 Data analysis was done in MATLAB (Mathworks) (MAIN_pop_analysis.m script for epifluorescence
604 snapshots, MAIN_timelapse.m script for timelapse movies and MAIN_mol_tracking.m script for
605 single-molecule tracking experiments), except for segmentation of phase contrast images, which was
606 done in Python (segmentationRun.py) using a convolutional neural network, the Nested-Unet (Wiktor
607 et al., 2021; Zhou et al., 2020), and the analysis of the SYTO RNASelect and RpoC-HaloTag-JF549
608 epifluorescence (snapshots_analysis_UNET_version_ND2.py class) that was also performed in Python
609 3.9 (DNA_limitation_python_environment.yml). The Nested-Unet network was trained for our

610 microscopy setup using PyTorch 1.7.0 and NumPY 1.19.2 (trainerWrapper.py) (Harris et al., 2020;
611 Paszke et al., 2019).

612 Cell area masks from segmentation were linked between time-lapse frames based on
613 maximum overlap (trackCells.m). Two masks linked to the same cell area were considered a cell
614 division event. To estimate the absolute growth rate, the cell area over time was smoothed by a
615 sliding-average window of five data points (time interval 5 min) and the difference in the cell area
616 between consecutive frames was calculated. The relative growth rate was calculated by dividing the
617 absolute growth rate by the cell area. Cell areas were converted into volumes using Oufti's scripts
618 (Paintdakhi et al., 2016). To avoid bias from cells reaching sizes too large to support growth, the time-
619 lapse data for filamenting cells was truncated based on their maximum absolute growth rate. We
620 confirmed that the relative reduction in the growth rate of 1N in comparison to multi-N cells was not
621 due to longer time-lapse duration as we observed no differences when acquiring shorter 2 h time-
622 lapse sequences (Figure 1 – figure supplement 5A). Finally, we confirmed that cells were under stable
623 growth conditions prior to starting imaging by showing that relative growth remained constant from
624 the beginning of acquisition (Figure 1 – figure supplement 5B).

625 Fluorescent ParB-mCherry spots were detected by fitting a 2D Gaussian function to raw image
626 data (detectSpots.m). First, the fluorescent image was filtered using a bandpass filter to identify the
627 local maxima. Next, the local maxima were fitted by a Gaussian function and a spot quality score was
628 calculated based on spot intensity and quality of a Gaussian fit (Intensity * $quality_{fit}$ / σ_{fit}). The spot
629 score threshold was determined by visual inspection of the training data and was set to remove poor-
630 quality spots from analysis.

631 The number of HU-mCherry-labeled nucleoid areas were detected using Otsu's thresholding
632 (multithresh.m) (Otsu, 1979). Minimum and maximum area thresholds for an individual nucleoid were
633 determined by measuring the number of fluorescent spots of ParB protein fusion in HU-labeled
634 nucleoid areas of a strain (CJW7517) carrying a *parS* site from plasmid pMT1 at *ori1* (Figure 1 –
635 supplement 3A). Only cells containing a single nucleoid were considered 1N cells. To measure the
636 total fluorescence intensity of a cell, the median intensity of the area outside the cell areas was
637 subtracted from the fluorescent intensity of each pixel of a cell, and the intensity of all pixels was
638 summed together.

639 For the SYTO RNASelect and RpoC-HaloTag-JF549 epi-fluorescence snapshot experiments
640 (Figure 4F-I, Figure 4 – supplement 4 and Figure 4 – supplement 5), the nucleoid objects were
641 segmented using the *segment_nucleoids* function in the *snapshots_analysis_UNET_version_ND2.py*
642 class. This function combines a Laplacian of Gaussian (LoG) filter, an adaptive filter, and a hard
643 threshold to detect the nucleoid boundaries and distinguish between 1N and multi-N cells in the
644 mixed populations. The image filters were applied using the scikit-image (Van Der Walt et al., 2014)
645 and NumPy (Harris et al., 2020) Python libraries. For the SYTO RNASelect-stained cells, the HU-
646 mCherry fluorescence was used to segment the nucleoid objects. For the RpoC-HaloTag-JF549-stained
647 cells, the fluorescence of RpoC-HaloTag-JF549 bound to nucleoids was used to segment the nucleoid
648 objects.

649 The SYTO RNASelect concentration corresponds to the total fluorescence of the fluorogenic
650 dye within the cell boundaries of the cell mask, divided by the area of the cell mask. Similarly, the
651 RpoC-HaloTag-JF549 concentration was calculated in arbitrary units.

652 To ensure that the SYTO RNASelect or the RpoC-HaloTag-JF549 fluorescence was compared
653 for the same distributions of cell areas between the 1N and multi-N cells in the mixed populations,
654 random sampling was performed in each cell area bin using a sample size equal to the smaller cell
655 number between the 1N and multi-N cells (Figure 4 – supplements 4 and 5B). For example, if in each
656 cell area bin, there were 200 1N cells and 100 multi-N cells, 100 cells were randomly sampled from
657 the 1N population to match the sample size of the multi-N population. Bins with less than 50 cells per
658 population across biological replicates were removed from the analysis. This sampling was performed
659 one time to compare the distributions of the SYTO RNASelect (Figure 4G) and RpoC-HaloTag-JF549
660 (Figure 4 – supplement 5C) concentrations between the 1N and multi-N cells. However, to estimate
661 the average 1N/multi-N SYTO RNASelect or RpoC-HaloTag-JF549 ratio during cell growth (Figure 4I
662 and Figure 4 – supplement 5E) multiple samplings (with substitution) were performed for each
663 biological replicate and cell area bin. This allowed us to use all the data while still comparing equal
664 numbers of 1N and multi-N cells per biological replicate and cell area bin. Cell area bins with less than
665 10 cells per biological replicate were removed from the analysis. Also here, the sample size was set
666 by the smallest population size (1N or multi-N population) and the number of iterations was equal to
667 the difference between the populations multiplied by 10.
668
669 **Single-molecule tracking analysis**
670 Single-molecule tracking data was analyzed as previously described (Mäkelä and Sherratt, 2020).
671 Candidate fluorescent spots were detected using band-pass filtering and an intensity threshold for
672 each frame of the time-lapse sequence. These initial localizations were used as starting positions in
673 phasor spot detection for high-precision localization (Martens et al., 2018). Individual molecules were

674 then tracked in each cell area by linking positions to a trajectory if they appeared in consecutive
675 frames within a distance of 0.8 µm. Cell areas were detected from bright-field images using
676 MicrobeTracker (Sliusarenko et al., 2011). In the case of multiple localizations within the tracking
677 radius, these localizations were omitted from the analysis. Tracking allowed for a single frame
678 disappearance of the molecule within a trajectory due to blinking or missed localization. The mobility
679 of each molecule was determined by calculating an apparent diffusion coefficient, D_a, from the
680 stepwise mean-squared displacement (MSD) of the trajectory using:

681 $$D_a = \frac{1}{4n\Delta t}\sum_{i=1}^{n}[x(i\Delta t) - x(i\Delta t + \Delta t)]^2 + [y(i\Delta t) - y(i\Delta t + \Delta t)]^2$$

682 where x(t) and y(t) indicate the coordinates of the molecule at time t, Δt is the frame rate of the
683 camera, and n is the total number of the steps in the trajectory. Trajectories with less than 9
684 displacements were omitted due to the higher uncertainty in D_a.

685 The calculated D_a are expected to reflect different dynamic states of molecules. To determine
686 the fraction of molecules in each state, $\log_{10}$ transformed D_a data (Figure 2D) was fitted to a Gaussian
687 mixture model (GMM) using the expectation-maximization algorithm (Bishop, Christopher, 2006). A
688 mixture of 3 Gaussian distributions with free parameters for mean, SD, and weight of each state were
689 fitted for different conditions (Figure 2D). Additionally, for 1N cells, single-molecule tracking data
690 were binned and fitted as a function of cell area (Figure 2D – supplement 3). To determine the active
691 RNAP or ribosome fraction of a single cell, the GMM was used to determine the state of each molecule
692 from the measured D_a, and the fraction of molecules in the slowest ("active") state was calculated.
693 Only cells with at least 50 trajectories were considered in the analysis for more accurate quantification.

694 The total quantity of active molecules was estimated by multiplying the measured total fluorescence
695 intensity with the measured active fraction as a function of the cell area.
696
697 **Sample preparation for liquid chromatography coupled to tandem mass spectrometry (LC-MS/MS)**
698 CRISPRi *oriC* (SJ_XTL676) cells were collected 0, 120, 180, 240 and 300 min after addition of 0.2%
699 arabinose, while CRISPRi *ftsZ* (SJ_XTL229) cells were collected after 0, 60, and 120 min of induction,
700 and pelleted. Cell pellets were lysed in 1% SDS at 95°C for 10 min (with vigorous intermittent vortexing
701 and in the presence of 5 mM β-mercaptoethanol as a reducing agent). Cell lysates were cleared by
702 centrifugation at 15000 x g for 30 min at 4°C. The lysates were alkylated with 10 mM iodoacetamide
703 for 15 min at room temperature, and then precipitated with three volumes of a solution containing
704 50% acetone and 50% ethanol. Precipitated proteins were re-solubilized in 2 M urea, 50 mM Tris-HCl,
705 pH 8.0, and 150 mM NaCl, and then digested with TPCK-treated trypsin (50:1) overnight at 37°C.
706 Trifluoroacetic acid was added to the digested peptides at a final concentration of 0.2%. Peptides
707 were desalted with a Sep-Pak 50 mg C18 column (Waters). The C18 column was conditioned with five
708 column volumes of 80% acetonitrile and 0.1% acetic acid, and then washed with five column volumes
709 of 0.1% trifluoroacetic acid. After samples were loaded, the column was washed with five column
710 volumes of 0.1% acetic acid followed by elution with four column volumes of 80% acetonitrile and
711 0.1% acetic acid. The elution was dried in a Concentrator at 45°C. Peptides (20 µg) resuspended in a
712 100-mM triethylammonium bicarbonate solution were labeled using 100 µg of Thermo TMT10plex™
713 in a reaction volume of 25 µl for 1 h. The labeling reaction was quenched with 8 µL of 5%
714 hydroxylamine for 15 min. Labeled peptides were pooled, acidified to a pH of ~2 using drops of 10%
715 trifluoroacetic acid, and desalted again with a Sep-Pak 50 mg C18 column as described above. TMT-

716 labeled peptides were pre-fractionated using a Pierce™ High pH Reversed-Phase Peptide
717 Fractionation Kit. Pre-fractionated peptides were dried using a concentrator and re-suspended in 0.1%
718 formic acid.
719
720 **LC-MS/MS data acquisition**
721 Pre-fractionated TMT-labeled peptides were analyzed on a Fusion Lumos mass spectrometer (Thermo
722 Fisher Scientific) equipped with a Thermo EASY-nLC 1200 LC system (Thermo Fisher Scientific).
723 Peptides were separated by capillary reverse phase chromatography on a 25 cm column (75 µm inner
724 diameter, packed with 1.6 µm C18 resin, AUR2-25075C18A, Ionopticks). Electrospray Ionization
725 voltage was set to 1550 V. Peptides were introduced into the Fusion Lumos mass spectrometer using
726 a 180 min stepped linear gradient at a flow rate of 300 nL/min. The steps of the gradient were as
727 follows: 6–33% buffer B (0.1% (v/v) formic acid in 80% acetonitrile) for 145 min, 33-45% buffer B for
728 15 min, 40-95% buffer B for 5 min, and 90% buffer B for 5 min. Column temperature was maintained
729 at 50°C throughout the procedure. Xcalibur software (Thermo Fisher Scientific) was used for the data
730 acquisition and the instrument was operated in data-dependent mode. Advanced peak detection was
731 disabled. Survey scans were acquired in the Orbitrap mass analyzer (centroid mode) over the range
732 of 380 to 1400 m/z with a mass resolution of 120,000 (at m/z 200). For MS1 (the survey scan), the
733 normalized AGC target (%) was set at 250 and the maximum injection time was set to 100 ms. Selected
734 ions were fragmented by the Collision Induced Dissociation (CID) method with normalized collision
735 energies of 34 and the tandem mass spectra were acquired in the ion trap mass analyzer with the
736 scan rate set to “Rapid”. The isolation window was set to 0.7 m/z. For MS2 (the peptide fragmentation
737 scan), the normalized AGC target (%) and the maximum injection time were set to “standard” and 35

738 ms, respectively. Repeated sequencing of peptides was kept to a minimum by dynamic exclusion of
739 the sequenced peptides for 30 s. The maximum duty cycle length was set to 3 s. Relative changes in
740 peptide concentration were determined at the level of the MS3 (reporter ion fragmentation scan) by
741 isolating and fragmenting the five most dominant MS2 ion peaks.
742
743 **Spectral searches**
744 All raw files were searched using the Andromeda engine (Thomason, Costantino, and Court 2007)
745 embedded in MaxQuant (v2.3.1.0) (Cox and Mann, 2008). A Reporter ion MS3 search was conducted
746 using 10plex TMT isobaric labels. Variable modifications included oxidation (M) and protein N-
747 terminal acetylation. Carbamidomethylation of cysteines was a fixed modification. The number of
748 modifications per peptide was capped at five. Digestion was set to tryptic (proline-blocked). Database
749 search was conducted using the UniProt proteome Ecoli_UP000000625_83333. The minimum
750 peptide length was seven amino acids. The false discovery rate was determined using a reverse decoy
751 proteome (Elias and Gygi, 2007).
752
753 **Proteomics data analysis**
754 Normalization and protein slope calculations were performed as described previously (Lanz et al.,
755 2022). In brief, the relative signal difference between the TMT channels for each peptide was plotted
756 against the normalized cell area for each of the bins of *E. coli* cells. For protein detection, we used a
757 minimum of three unique peptide measurements per protein as a threshold. To derive the protein
758 slope values shown in Figure 5, individual peptide measurements were consolidated into a protein
759 level measurement using Python's groupby.median. Peptides with the same amino acid sequence that

760 were identified as different charge states or in different fractions were considered independent
761 measurements. We summarized the size scaling behavior of individual proteins as a slope value
762 derived from a regression. Each protein slope value was based on the behavior of all detected
763 peptides.
764

765 For a given protein, we calculated the cell size-dependent slope as follows:

766 y_i = relative signal in the ith TMT channel (median of all corresponding peptides in this channel)

767 x_i = normalized cell size in the ith TMT channel (cell area for a given timepoint / mean cell area for the
768 experiment)

769 The protein slope value was determined from a linear fit to the log-transformed data using the
770 equation:

771 $$\mathrm{Log}_2(y) = \mathrm{Slope} * \log_2(x)$$

772 Variables were log-transformed so that a slope of 1 corresponds to an increase in protein
773 concentration that is proportional to the increase in cell volume, and a slope of -1 corresponds to
774 1/volume dilution. Pearson correlation coefficients and p values were calculated using SciPy's
775 pearsonr module in Python (Virtanen et al., 2020). The results were reproducible across the two
776 replicates (Figure 5 – figure supplement 1).

777

778

779 **Estimation of protein abundance using summed ion intensity**

780 MS1-level peptide ion intensities from experiment #1 were used to estimate the relative protein
781 abundance. For each protein, all peptide intensities were summed together using the "Intensity"
782 column of MaxQuant's evidence.txt file. To adjust for the fact that larger proteins produce more
783 tryptic peptides, the summed ion intensity for each protein was divided by its amino acid sequence
784 length.

785

786 **Calculation of distance from *oriC***

787 Gene coordinates were downloaded from EcoCyc database. The midpoint of each coding sequence
788 was used to determine the circular distance (in base pairs) from *oriC* (base pair 3,925,859 of the total
789 length of 4,641,652). A script was written to make three distance calculations. First, the direct distance
790 (the midpoint of each gene minus 3,925,859 bp (*oriC*)) was determined. Next, the midpoint coordinate
791 of each gene was subtracted by the total genome length (4,641,652 bp) and then subtracted again by
792 the coordinate of *oriC* (3,925,859 bp). Finally, the midpoint coordinate of each gene was added to the
793 total genome length (4,641,652 bp) and then subtracted by the coordinate of *oriC* (3,925,859 bp). The
794 absolute values of these three calculations were then taken and the minimal values represent the
795 circular distances between *oriC* and each gene.

796

797 **Sample preparation for RNA-seq experiments**

798 CRISPRi *oriC* strain (SJ_XTL676) was grown in M9glyCAAT at 37°C and cells were collected 60, 120, 200,
799 and 240 min after addition of 0.2% L-arabinose. Images of cells were acquired at each timepoint to

800 determine cell area, as described above. For each timepoint, the aliquot was spun down, the
801 supernatant was removed, and the pellet was flash-frozen. *E. coli* pellets were resuspended in ice cold
802 phosphate buffer saline solution (PBS) and mixed with *C. crescentus* cells in approximately a 1-to-1
803 ratio based on OD_{600}. *C. crescentus* cells were originally included with the intent of using them as a
804 spike-in reference. However, the fraction of final reads obtained from *C. crescentus* transcripts was
805 inconsistent with the initial mixing ratios. In addition, without knowing the exact DNA concentration
806 in each 1N-rich cell sample, this spike-in became purposeless and thus was ignored for analysis. Cells
807 (50 µL) in PBS were mixed with 250 µl TRI Reagent (Zymo Research) and lysed by bead beating on a
808 Fastprep 24 (MPbio). Cell debris were pelleted (14k rpm, 2 min) and the supernatant was recovered.
809 RNA was then extracted using the direct-zol RNA microprep kit (Zymo Research). Ribosomal RNA
810 (rRNA) was then depleted using the NEBNext rRNA Depletion Kit for Bacteria (NEB, #E7850) and
811 NEBNext Ultra II Directional RNA Library Prep Kit for Illumina (NEB, #E7760) was then used to prepare
812 libraries for paired-end (2x150bp) Illumina sequencing (Novogene).
813
814 **RNA-seq data analysis**
815 A combined genome file of *E. coli* K-12 MG1655 and *C. crescentus* NA1000 with gene annotations was
816 generated using a previously described approach (Swaffer et al., 2023). Read mapping statistics and
817 genome browser tracks were generated using custom Python scripts. For quantification purposes,
818 reads were aligned as 2x50mers in transcriptome space against an index generated from the
819 combined gene annotation model using Bowtie (version 1.0.1 ; settings: -e 200 -a -X 1000) (Langmead
820 et al., 2009). Alignments were then quantified using eXpress (version 1.5.1) (Roberts and Pachter,

821 2013) as TPM (Transcripts Per Million). TPM values were then recalculated after filtering for only *E.*
822 *coli* genes. E. coli genes with TPM values below 1 were then removed from analysis.

823 The RNA slope (i.e., relative transcript concentration vs. cell area) was calculated for each gene
824 as follows. TPM values were normalized to the mean of all values for that gene and then log2
825 transformed. The same normalization was applied to the cell area measurements for each condition.
826 A linear model was fitted to the normalized log2 data and the slope of the linear regression was taken
827 as the RNA slope.

828

829 **Mathematical model and simulations**

830 Phenomenological model: We developed a phenomenological model to illustrate cell growth
831 dynamics. In our models, the number of mRNA (X) and the number of protein (Y) in the cell are
832 described by the differential equations:

833 $$\frac{dX}{dt} = r_1 \alpha_{RNAP}(X,Y)Y - \delta X \qquad \text{(Eq.1)}$$

834 $$\frac{dY}{dt} = r_2 \alpha_{ribo}(X,Y)Y \qquad \text{(Eq. 2)}$$

835 where $r_1 = \frac{\text{bulk transcription rate}}{\text{total protein number}}$, $r_2 = \frac{\text{bulk translation rate}}{\text{total protein number}}$, $\alpha_{RNAP}(X,Y)$ is the fraction of active RNA
836 polymerases, $\alpha_{ribo}(X,Y)$ is the fraction of active ribosomes, and δ is the mRNA degradation rate. We
837 assumed that the protein degradation is negligible because most bacterial proteins are stable
838 (Balakrishnan et al., 2022; Lin and Amir, 2018). For the fraction of active RNAPs, we considered two
839 different models (models A and B). In model A, the fraction of active RNAPs was modeled by $\alpha_{RNAP} =$
840 $\frac{[Z]}{K_1+[Z]}$. In model B, where we included different states of RNAP and promoter, the expression of α_{RNAP}
841 is more complicated and is described in Appendix 2. For both models, the ribosomes were modeled

842 by $\alpha_{ribo} = \frac{[X]}{K_2+[X]}$. We used $[Z]$ and $[X]$ to represent the genome and mRNA concentrations,

843 respectively. We assumed that the cell volume (*V*) and cell area (*A*) are proportional to the protein

844 number Y, which is a good approximation (Basan et al., 2015; Kubitschek et al., 1984). While this

845 assumption has not been verified in 1N cells, the concentration of ribosomes, which constitute most

846 of the protein mass, were found to remain constant in these cells (Figure 2A). Namely, in our model,

847 $V = cY$ and $A = c'Y$ with constants c, c'. Under balanced growth conditions, $[Z]$ was assumed to be

848 constant. For the DNA-limited growth condition (as in 1N cells), we assumed that the genome does

849 not duplicate and is kept at a single copy per cell ($Z(t) = 1$) while the cell volume continue to increase.

850 The details for parameters used in this model are described in Table 1.

851 Numerical simulations: To simulate the model for balanced and DNA-limited growths, we first

852 fixed a parameter set based on the literature (see Tables 1 and 2) and simulated Eq. 1 and Eq. 2 to

853 reach the regime of balanced growth. Under balanced growth, we obtained the balanced growth

854 vector (X^*, Y^*) where Y^* matches the initial protein number reported in the literature (see Table 2).

855 Then, using the balanced growth vector as the initial condition, we simulated the balanced growth

856 and DNA-limited growth using different assumptions of genome content $Z(t)$ (described in the

857 previous paragraph). The simulation was performed using the MATLAB built-in function *ode23* with

858 relative and absolute errors of the numerical values to be 10^{-4} and 10^{-5}, respectively. For each growth

859 condition, we obtained growth trajectories $\big(X(t), Y(t)\big)$, and from $Y(t)$, we calculated the cell

860 volume $V(t)$ and area $A(t)$ as described above. For model A, the fraction of active RNAPs was

861 calculated by $\alpha_{RNAP} = \frac{[Z]}{K_1+[Z]}$, while for model B, it is calculated using a more complicated formula

862 that take into account RNAP kinetics (see Appendix 2). For both models, the fraction of active
863 ribosomes was calculated as $\alpha_{ribo} = \frac{[X]}{K_2+[X]}$.

864 Parameter fitting: For either model A or B, we fitted our simulation results to all the
865 experimental data including growth curves, the fraction of active RNAPs, and the fraction of active
866 ribosomes for 1N and WT or multi-N cells (six datasets in total); see Appendix 1 for the initial
867 parameter estimation and Appendix 3 for the optimization procedure details. The optimized
868 parameter sets (see Table 2) were used for the numerical simulations shown in Figure 4. Note that
869 the optimized parameter set remained within the realistic range for cellular physiology (see Appendix
870 3 - figure 1 for comparison between original and optimized parameters).

871

872 **DATA AVAILABILITY**

873 Microscopy image analysis code is available on the Jacobs-Wagner lab github repository
874 (https://github.com/JacobsWagnerLab/published/tree/master/Makela_2023). The TMT-MS and
875 RNA-seq data analysis and processing code is available at
876 https://github.com/mikechucklanz/Proteome_size_scaling_Ecoli and
877 https://github.com/georgimarinov/GeorgiScripts.

878 For this study, the following TMT-MS and RNA-seq data were generated. Dataset 1 includes
879 the calculated protein slopes from 1N-rich and multi-N cells, the normalized protein proportions, the
880 summed ion intensities for each protein as well as the distance of its gene from the origin of
881 replication (*oriC*) and the GO-term analysis. Dataset 2 includes the calculated mRNA slopes, in
882 comparison with the average protein slopes from 1N-rich cells. All sequencing data associated with
883 this study were submitted to the GEO repository on 2/10/2024 (GEO: GSEXXXX—will be updated

884 when available). The mass spectrometry proteomics data have been deposited to the
885 ProteomeXchange Consortium via the PRIDE partner repository with the dataset identifier
886 PXD050093.

887

888 **ACKNOWLEDGMENTS**

889 We thank Drs. Brun, Jun, Marczynski, Shapiro and Weisshaar for sharing published strains. We are
890 grateful to Dr. Lavis for the gift of JF549 and Dr. Badrinarayanan for valuable discussion. We would
891 also like to thank the Jacobs-Wagner laboratory for support, discussion, and critical reading of the
892 manuscript. C.J.-W. is an investigator of the Howard Hughes Medical Institute.

893

894 **REFERENCES**

895 Aaron M, Charbon G, Lam H, Schwarz H, Vollmer W, Jacobs-Wagner C. 2007. The tubulin homologue
896 FtsZ contributes to cell elongation by guiding cell wall precursor synthesis in Caulobacter
897 crescentus. *Mol Microbiol* **64**:938–952. doi:10.1111/j.1365-2958.2007.05720.x
898 Addinall SG, Bi E, Lutkenhaus J. 1996. FtsZ ring formation in fts mutants. *J Bacteriol* **178**:3877–3884.
899 Bakshi S, Choi H, Mondal J, Weisshaar JC. 2014. Time-dependent effects of transcription- and
900 translation-halting drugs on the spatial distributions of the Escherichia coli chromosome and
901 ribosomes. *Mol Microbiol* **94**:871–887. doi:10.1111/mmi.12805
902 Bakshi S, Siryaporn A, Goulian M, Weisshaar JC. 2012. Superresolution imaging of ribosomes and
903 RNA polymerase in live Escherichia coli cells. *Mol Microbiol* **85**:21–38. doi:10.1111/j.1365-
904 2958.2012.08081.x
905 Balakrishnan R, Mori M, Segota I, Zhang Z, Aebersold R, Ludwig C, Hwa T. 2022. Principles of gene
906 regulation quantitatively connect DNA to RNA and proteins in bacteria. *Science*
907 **378**:eabk2066. doi:10.1126/science.abk2066
908 Banaz N, Mäkelä J, Uphoff S. 2019. Choosing the right label for single-molecule tracking in live
909 bacteria: side-by-side comparison of photoactivatable fluorescent protein and Halo tag dyes.
910 *J Phys Appl Phys* **52**:064002. doi:10.1088/1361-6463/aaf255
911 Banerjee S, Lo K, Daddysman MK, Selewa A, Kuntz T, Dinner AR, Scherer NF. 2017. Biphasic growth
912 dynamics control cell division in Caulobacter crescentus. *Nat Microbiol* **2**:6–11.
913 doi:10.1038/nmicrobiol.2017.116
914 Basan M, Zhu M, Dai X, Warren M, Sévin D, Wang Y-P, Hwa T. 2015. Inflating bacterial cells by
915 increased protein synthesis. *Mol Syst Biol* **11**:836. doi:10.15252/msb.20156178

916 Belliveau NM, Chure G, Hueschen CL, Garcia HG, Kondev J, Fisher DS, Theriot JA, Phillips R. 2021.
917 Fundamental limits on the rate of bacterial growth and their influence on proteomic
918 composition. *Cell Syst* **12**:924-944.e2. doi:10.1016/j.cels.2021.06.002
919 Bishop, Christopher. 2006. Pattern Recognition and Machine Learning. New York, NY: Springer.
920 Blundell MR, Wild DG. 1971. Altered ribosomes after inhibition of Escherichia coli by rifampicin.
921 *Biochem J* **121**:391–398. doi:10.1042/bj1210391
922 Bosdriesz E, Molenaar D, Teusink B, Bruggeman FJ. 2015. How fast-growing bacteria robustly tune
923 their ribosome concentration to approximate growth-rate maximization. *FEBS J* **282**:2029–
924 2044. doi:10.1111/febs.13258
925 Bremer H, Dennis P. 1996. Modulation of chemical composition and other parameters of the cell by
926 growth rate. *Neidhardt F Ed Wash DC Am Soc Microbiol Press* 1553.
927 Cadart C, Monnier S, Grilli J, Sáez PJ, Srivastava N, Attia R, Terriac E, Baum B, Cosentino-Lagomarsino
928 M, Piel M. 2018. Size control in mammalian cells involves modulation of both growth rate
929 and cell cycle duration. *Nat Commun* **9**:3275. doi:10.1038/s41467-018-05393-0
930 Campbell EA, Korzheva N, Mustaev A, Murakami K, Nair S, Goldfarb A, Darst SA. 2001. Structural
931 mechanism for rifampicin inhibition of bacterial rna polymerase. *Cell* **104**:901–912.
932 doi:10.1016/s0092-8674(01)00286-0
933 Campos M, Surovtsev IV, Kato S, Paintdakhi A, Beltran B, Ebmeier SE, Jacobs-Wagner C. 2014. A
934 constant size extension drives bacterial cell size homeostasis. *Cell* **159**:1433–1446.
935 doi:10.1016/j.cell.2014.11.022
936 Carl PL. 1970. Escherichia coli mutants with temperature-sensitive synthesis of DNA. *MGG Mol Gen*
937 *Genet* **109**:107–122. doi:10.1007/BF00269647
938 Cherepanov PP, Wackernagel W. 1995. Gene disruption in Escherichia coli: TcR and KmR cassettes
939 with the option of Flp-catalyzed excision of the antibiotic-resistance determinant. *Gene*
940 **158**:9–14. doi:10.1016/0378-1119(95)00193-A
941 Churchward G, Bremer H, Young R. 1982. Transcription in bacteria at different DNA concentrations. *J*
942 *Bacteriol* **150**:572–581. doi:10.1128/jb.150.2.572-581.1982
943 Claude K-L, Bureik D, Chatzitheodoridou D, Adarska P, Singh A, Schmoller KM. 2021. Transcription
944 coordinates histone amounts and genome content. *Nat Commun* **12**:4202.
945 doi:10.1038/s41467-021-24451-8
946 Crozier L, Foy R, Adib R, Kar A, Holt JA, Pareri AU, Valverde JM, Rivera R, Weston WA, Wilson R,
947 Regnault C, Whitfield P, Badonyi M, Bennett LG, Vernon EG, Gamble A, Marsh JA, Staples CJ,
948 Saurin AT, Barr AR, Ly T. 2023. CDK4/6 inhibitor-mediated cell overgrowth triggers osmotic
949 and replication stress to promote senescence. *Mol Cell* **83**:4062-4077.e5.
950 doi:10.1016/j.molcel.2023.10.016
951 Cylke A, Banerjee S. 2023. Super-exponential growth and stochastic size dynamics in rod-like
952 bacteria. *Biophys J* **122**:1254–1267. doi:10.1016/j.bpj.2023.02.015
953 Datsenko KA, Wanner BL. 2000. One-step inactivation of chromosomal genes in Escherichia coli K-12
954 using PCR products. *Proc Natl Acad Sci* **97**:6640–6645. doi:10.1073/pnas.120163297
955 Donachie W. 1968. Relationship between cell size and time of initiation of DNA replication. *Nature*
956 **219**:1077–1079. doi:10.1038/2191077a0
957 Ecker RE, Schaechter M. 1963. Ribosome content and the rate of growth of Salmonella
958 typhimurium. *BBA - Biochim Biophys Acta* **76**:275–279. doi:10.1016/0006-3002(63)90040-4

959 Elias JE, Gygi SP. 2007. Target-decoy search strategy for increased confidence in large-scale protein
960 identifications by mass spectrometry. *Nat Methods* **4**:207–214. doi:10.1038/nmeth1019
961 Elowitz MB, Surette MG, Wolf P-E, Stock JB, Leibler S. 1999. Protein Mobility in the Cytoplasm of
962 Escherichia coli. *J Bacteriol* **181**:197–203. doi:10.1128/JB.181.1.197-203.1999
963 Ely B. 1991. [17] Genetics of Caulobacter crescentus. *Methods Enzymol* **204**:372–384.
964 doi:10.1016/0076-6879(91)04019-K
965 Fossum S, Crooke E, Skarstad K. 2007. Organization of sister origins and replisomes during multifork
966 DNA replication in Escherichia coli. *EMBO J* **26**:4514–4522. doi:10.1038/sj.emboj.7601871
967 Foy R, Crozier L, Pareri AU, Valverde JM, Park BH, Ly T, Saurin AT. 2023. Oncogenic signals prime
968 cancer cells for toxic cell overgrowth during a G1 cell cycle arrest. *Mol Cell* **83**:4047-4061.e6.
969 doi:10.1016/j.molcel.2023.10.020
970 Frandi A, Collier J. 2019. Multilayered control of chromosome replication in Caulobacter crescentus.
971 *Biochem Soc Trans* **47**:187–196. doi:10.1042/BST20180460
972 Ginzberg MB, Kafri R, Kirschner M. 2015. On being the right (cell) size. *Science* **348**:1245075.
973 doi:10.1126/science.1245075
974 Gorbatyuk B, Marczynski GT. 2001. Physiological consequences of blocked Caulobacter crescentus
975 dnaA expression, an essential DNA replication gene. *Mol Microbiol* **40**:485–497.
976 doi:10.1046/j.1365-2958.2001.02404.x
977 Govers SK, Campos M, Tyagi B, Laloux G, Jacobs-Wagner C. 2024. Apparent simplicity and emergent
978 robustness in the control of the *Escherichia coli* cell cycle. *Cell Syst* **15**:19-36.e5.
979 doi:10.1016/j.cels.2023.12.001
980 Gray WT, Govers SK, Xiang Y, Parry BR, Campos M, Kim S, Jacobs-Wagner C. 2019. Nucleoid Size
981 Scaling and Intracellular Organization of Translation across Bacteria. *Cell* **177**:1632-1648.e20.
982 doi:10.1016/J.CELL.2019.05.017
983 Grimm JB, English BP, Chen J, Slaughter JP, Zhang Z, Revyakin A, Patel R, Macklin JJ, Normanno D,
984 Singer RH, Lionnet T, Lavis LD. 2015. A general method to improve fluorophores for live-cell
985 and single-molecule microscopy. *Nat Methods* **12**:244–250. doi:10.1038/nmeth.3256
986 Guyer MS, Reed RR, Steitz JA, Low KB. 1981. Identification of a Sex-factor-affinity Site in E. coli as γδ.
987 *Cold Spring Harb Symp Quant Biol* **45**:135–140. doi:10.1101/SQB.1981.045.01.022
988 Harris CR, Millman KJ, van der Walt SJ, Gommers R, Virtanen P, Cournapeau D, Wieser E, Taylor J,
989 Berg S, Smith NJ, Kern R, Picus M, Hoyer S, van Kerkwijk MH, Brett M, Haldane A, Del Río JF,
990 Wiebe M, Peterson P, Gérard-Marchant P, Sheppard K, Reddy T, Weckesser W, Abbasi H,
991 Gohlke C, Oliphant TE. 2020. Array programming with NumPy. *Nature* **585**:357–362.
992 doi:10.1038/s41586-020-2649-2
993 Heinrich K, Leslie DJ, Morlock M, Bertilsson S, Jonas K. 2019. Molecular Basis and Ecological
994 Relevance of Caulobacter Cell Filamentation in Freshwater Habitats. *mBio* **10**:e01557-19.
995 doi:10.1128/mBio.01557-19
996 Kar P, Tiruvadi-Krishnan S, Männik Jaana, Männik Jaan, Amir A. 2021. Distinguishing different modes
997 of growth using single-cell data. *eLife* **10**:1–34. doi:10.7554/elife.72565
998 Kim S, Beltran B, Irnov I, Jacobs-Wagner C. 2019. Long-Distance Cooperative and Antagonistic RNA
999 Polymerase Dynamics via DNA Supercoiling. *Cell* **179**:106-119.e16.
1000 doi:10.1016/j.cell.2019.08.033
1001 Koch AL. 1988. Why can't a cell grow infinitely fast? *Can J Microbiol* **34**:421–426. doi:10.1139/m88-
1002 074

1003 Kubitschek HE, Baldwin WW, Schroeter SJ, Graetzer R. 1984. Independence of buoyant cell density
1004 and growth rate in Escherichia coli. *J Bacteriol* **158**:296. doi:10.1128/jb.158.1.296-299.1984
1005 Langmead B, Trapnell C, Pop M, Salzberg SL. 2009. Ultrafast and memory-efficient alignment of
1006 short DNA sequences to the human genome. *Genome Biol* **10**:R25. doi:10.1186/gb-2009-10-
1007 3-r25
1008 Lanz MC, Zatulovskiy E, Swaffer MP, Zhang L, Ilerten I, Zhang S, You DS, Marinov G, McAlpine P, Elias
1009 JE, Skotheim JM. 2022. Increasing cell size remodels the proteome and promotes
1010 senescence. *Mol Cell* **82**:3255-3269.e8. doi:10.1016/j.molcel.2022.07.017
1011 Lanz MC, Zhang S, Swaffer MP, Ziv I, Götz LH, McCarty F, Jarosz DF, Elias JE, Skotheim JM. 2023.
1012 Genome dilution by cell growth drives starvation-like proteome remodeling in mammalian
1013 and yeast cells. doi:10.1101/2023.10.16.562558
1014 Lasker K, Mann TH, Shapiro L. 2016. An intracellular compass spatially coordinates cell cycle
1015 modules in *Caulobacter crescentus*. *Curr Opin Microbiol*, Antimicrobials Microbial systems
1016 biology **33**:131–139. doi:10.1016/j.mib.2016.06.007
1017 Li X, Jun Y, Erickstad MJ, Brown SD, Parks A, Court DL, Jun S. 2016. tCRISPRi: tunable and reversible,
1018 one-step control of gene expression. *Sci Rep* **6**:39076. doi:10.1038/srep39076
1019 Lilleorg S, Reier K, Pulk A, Liiv A, Tammsalu T, Peil L, Cate JHD, Remme J. 2019. Bacterial ribosome
1020 heterogeneity: Changes in ribosomal protein composition during transition into stationary
1021 growth phase. *Biochimie* **156**:169–180. doi:10.1016/j.biochi.2018.10.013
1022 Lin J, Amir A. 2018. Homeostasis of protein and mRNA concentrations in growing cells. *Nat Commun*
1023 **9**:4496. doi:10.1038/s41467-018-06714-z
1024 Lin W-H, Jacobs-Wagner C. 2022. Connecting single-cell ATP dynamics to overflow metabolism, cell
1025 growth, and the cell cycle in Escherichia coli. *Curr Biol* **32**:3911-3924.e4.
1026 doi:10.1016/j.cub.2022.07.035
1027 Liu X, Yan J, Kirschner MW. 2022. Beyond G1/S regulation: how cell size homeostasis is tightly
1028 controlled throughout the cell cycle? doi:10.1101/2022.02.03.478996
1029 Mäkelä J, Sherratt DJ. 2020. Organization of the Escherichia coli Chromosome by a MukBEF Axial
1030 Core. *Mol Cell* **78**:250-260.e5. doi:10.1016/j.molcel.2020.02.003
1031 Manohar S, Estrada ME, Uliana F, Vuina K, Alvarez PM, de Bruin RAM, Neurohr GE. 2023. Genome
1032 homeostasis defects drive enlarged cells into senescence. *Mol Cell* **83**:4032-4046.e6.
1033 doi:10.1016/j.molcel.2023.10.018
1034 Martens KJA, Bader AN, Baas S, Rieger B, Hohlbein J. 2018. Phasor based single-molecule localization
1035 microscopy in 3D (pSMLM-3D): An algorithm for MHz localization rates using standard CPUs.
1036 *J Chem Phys* **148**:123311. doi:10.1063/1.5005899
1037 Mohapatra S, Weisshaar JC. 2018. Functional mapping of the E. coli translational machinery using
1038 single-molecule tracking. *Mol Microbiol* **110**:262–282. doi:10.1111/mmi.14103
1039 Mu L, Kang JH, Olcum S, Payer KR, Calistri NL, Kimmerling RJ, Manalis SR, Miettinen TP. 2020. Mass
1040 measurements during lymphocytic leukemia cell polyploidization decouple cell cycle- and cell
1041 size-dependent growth. *Proc Natl Acad Sci* **117**:15659–15665. doi:10.1073/pnas.1922197117
1042 Neidhardt FC, Ingraham JL, Schaechter M. 1990. Physiology of the Bacterial Cell: A Molecular
1043 Approach. Sunderland, Mass: Sinauer Associates Inc.
1044 Neurohr GE, Terry RL, Lengefeld J, Bonney M, Brittingham GP, Moretto F, Miettinen TP, Vaites LP,
1045 Soares LM, Paulo JA, Harper JW, Buratowski S, Manalis S, van Werven FJ, Holt LJ, Amon A.

2019. Excessive Cell Growth Causes Cytoplasm Dilution And Contributes to Senescence. *Cell* **176**:1083-1097.e18. doi:10.1016/J.CELL.2019.01.018

Nielsen HJ, Ottesen JR, Youngren B, Austin SJ, Hansen FG. 2006. The Escherichia coli chromosome is organized with the left and right chromosome arms in separate cell halves. *Mol Microbiol* **62**:331–338. doi:10.1111/j.1365-2958.2006.05346.x

Nordholt N, van Heerden JH, Bruggeman FJ. 2020. Biphasic Cell-Size and Growth-Rate Homeostasis by Single Bacillus subtilis Cells. *Curr Biol* **30**:2238-2247.e5. doi:10.1016/j.cub.2020.04.030

Otsu N. 1979. A threshold selection method from gray-level histograms. *IEEE Trans Sys Man Cyber* **9**:62–66. doi:10.1109/TSMC.1979.4310076

Paintdakhi A, Parry B, Campos M, Irnov I, Elf J, Surovtsev I, Jacobs-Wagner C. 2016. Oufti: an integrated software package for high-accuracy, high-throughput quantitative microscopy analysis. *Mol Microbiol* **99**:767–777. doi:10.1111/mmi.13264

Paszke A, Gross S, Massa F, Lerer A, Bradbury J, Chanan G, Killeen T, Lin Z, Gimelshein N, Antiga L, Desmaison A, Köpf A, Yang E, DeVito Z, Raison M, Tejani A, Chilamkurthy S, Steiner B, Fang L, Bai J, Chintala S. 2019. PyTorch: An Imperative Style, High-Performance Deep Learning Library. *arXiv*, Advances in Neural Information Processing Systems 32 1912.01703. doi:10.48550/arXiv.1912.01703

Phillips LA, Hotham-Iglewski B, Franklin RM. 1969. Polyribosomes of Escherichia coli: II. Experiments to determine the in vivo distribution of polysomes, ribosomes and ribosomal subunits. *J Mol Biol* **45**:23–38. doi:10.1016/0022-2836(69)90207-1

Reshes G, Vanounou S, Fishov I, Feingold M. 2008. Cell Shape Dynamics in Escherichia coli. *Biophys J* **94**:251–264. doi:10.1529/biophysj.107.104398

Roberts A, Pachter L. 2013. Streaming fragment assignment for real-time analysis of sequencing experiments. *Nat Methods* **10**:71–73. doi:10.1038/nmeth.2251

Sanamrad A, Persson F, Lundius EG, Fange D, Gynnå AH, Elf J. 2014. Single-particle tracking reveals that free ribosomal subunits are not excluded from the Escherichia coli nucleoid. *Proc Natl Acad Sci* **111**:11413–11418. doi:10.1073/pnas.1411558111

Schaechter M, Maaloe O, Kjeldgaard NO. 1958. Dependency on Medium and Temperature of Cell Size and Chemical Composition during Balanced Growth of Salmonella typhimurium. *J Gen Microbiol* **19**:592–606. doi:10.1099/00221287-19-3-592

Schaechter M, Williamson JP, Hood JR, Koch AL. 1962. Growth, Cell and Nuclear Divisions in some Bacteria. *Microbiology* **29**:421–434. doi:10.1099/00221287-29-3-421

Scott M, Gunderson CW, Mateescu EM, Zhang Z, Hwa T. 2010. Interdependence of Cell Growth and Gene Expression: Origins and Consequences. *Science* **330**:1099–1102. doi:10.1126/science.1192588

Scott M, Klumpp S, Mateescu EM, Hwa T. 2014. Emergence of robust growth laws from optimal regulation of ribosome synthesis. *Mol Syst Biol* **10**:747. doi:10.15252/msb.20145379

Si F, Le Treut G, Sauls JT, Vadia S, Levin PA, Jun S. 2019. Mechanistic Origin of Cell-Size Control and Homeostasis in Bacteria. *Curr Biol* **29**:1760-1770.e7. doi:10.1016/j.cub.2019.04.062

Si F, Li D, Cox SE, Sauls JT, Azizi O, Sou C, Schwartz AB, Erickstad MJ, Jun Y, Li X, Jun S. 2017. Invariance of Initiation Mass and Predictability of Cell Size in Escherichia coli. *Curr Biol* **27**:1278–1287. doi:10.1016/j.cub.2017.03.022

Siegal-Gaskins D, Crosson S. 2008. Tightly Regulated and Heritable Division Control in Single Bacterial Cells. *Biophys J* **95**:2063–2072. doi:10.1529/BIOPHYSJ.108.128785

1090 Sliusarenko O, Heinritz J, Emonet T, Jacobs-Wagner C. 2011. High-throughput, subpixel precision
1091 analysis of bacterial morphogenesis and intracellular spatio-temporal dynamics. *Mol*
1092 *Microbiol* **80**:612–627. doi:10.1111/j.1365-2958.2011.07579.x
1093 Swaffer MP, Kim J, Chandler-Brown D, Langhinrichs M, Marinov GK, Greenleaf WJ, Kundaje A,
1094 Schmoller KM, Skotheim JM. 2021. Transcriptional and chromatin-based partitioning
1095 mechanisms uncouple protein scaling from cell size. *Mol Cell* **81**:4861-4875.e7.
1096 doi:10.1016/j.molcel.2021.10.007
1097 Swaffer MP, Marinov GK, Zheng H, Fuentes Valenzuela L, Tsui CY, Jones AW, Greenwood J, Kundaje
1098 A, Greenleaf WJ, Reyes-Lamothe R, Skotheim JM. 2023. RNA polymerase II dynamics and
1099 mRNA stability feedback scale mRNA amounts with cell size. *Cell* **186**:5254-5268.e26.
1100 doi:10.1016/j.cell.2023.10.012
1101 Taheri-Araghi S, Bradde S, Sauls JT, Hill NS, Levin PA, Paulsson J, Vergassola M, Jun S. 2015. Cell-Size
1102 Control and Homeostasis in Bacteria. *Curr Biol* **25**:385–391. doi:10.1016/j.cub.2014.12.009
1103 Takacs CN, Kloos ZA, Scott M, Rosa PA, Jacobs-Wagner C. 2018. Fluorescent Proteins, Promoters,
1104 and Selectable Markers for Applications in the Lyme Disease Spirochete Borrelia burgdorferi.
1105 *Appl Environ Microbiol* **84**:e01824-18. doi:10.1128/AEM.01824-18
1106 Takacs CN, Wachter J, Xiang Y, Ren Z, Karaboja X, Scott M, Stoner MR, Irnov I, Jannetty N, Rosa PA,
1107 Wang X, Jacobs-Wagner C. 2022. Polyploidy, regular patterning of genome copies, and
1108 unusual control of DNA partitioning in the Lyme disease spirochete. *Nat Commun* **13**:7173.
1109 doi:10.1038/s41467-022-34876-4
1110 Terrana B, Newton A. 1975. Pattern of unequal cell division and development in Caulobacter
1111 crescentus. *Dev Biol* **44**:380–385. doi:10.1016/0012-1606(75)90409-1
1112 Thanbichler M, Iniesta AA, Shapiro L. 2007. A comprehensive set of plasmids for vanillate- and
1113 xylose-inducible gene expression in Caulobacter crescentus. *Nucleic Acids Res* **35**:e137.
1114 doi:10.1093/nar/gkm818
1115 Thanbichler M, Shapiro L. 2006. MipZ, a Spatial Regulator Coordinating Chromosome Segregation
1116 with Cell Division in Caulobacter. *Cell* **126**:147–162. doi:10.1016/j.cell.2006.05.038
1117 Thomason LC, Costantino N, Court DL. 2007. E. coli Genome Manipulation by P1 Transduction. *Curr*
1118 *Protoc Mol Biol* **79**:1.17.1-1.17.8. doi:10.1002/0471142727.mb0117s79
1119 Tokunaga M, Imamoto N, Sakata-Sogawa K. 2008. Highly inclined thin illumination enables clear
1120 single-molecule imaging in cells. *Nat Methods* **5**:159–161. doi:10.1038/nmeth1171
1121 Turner JJ, Ewald JC, Skotheim JM. 2012. Cell size control in yeast. *Curr Biol* **22**:R350–R359.
1122 doi:10.1016/j.cub.2012.02.041
1123 Van Der Walt S, Schönberger JL, Nunez-Iglesias J, Boulogne F, Warner JD, Yager N, Gouillart E, Yu T.
1124 2014. scikit-image: image processing in Python. *PeerJ* **2**:e453. doi:10.7717/peerj.453
1125 Virtanen P, Gommers R, Oliphant TE, Haberland M, Reddy T, Cournapeau D, Burovski E, Peterson P,
1126 Weckesser W, Bright J, van der Walt SJ, Brett M, Wilson J, Millman KJ, Mayorov N, Nelson
1127 ARJ, Jones E, Kern R, Larson E, Carey CJ, Polat İ, Feng Y, Moore EW, VanderPlas J, Laxalde D,
1128 Perktold J, Cimrman R, Henriksen I, Quintero EA, Harris CR, Archibald AM, Ribeiro AH,
1129 Pedregosa F, van Mulbregt P. 2020. SciPy 1.0: fundamental algorithms for scientific
1130 computing in Python. *Nat Methods* **17**:261–272. doi:10.1038/s41592-019-0686-2
1131 Wang P, Robert L, Pelletier J, Dang WL, Taddei F, Wright A, Jun S. 2010. Robust Growth of
1132 Escherichia coli. *Curr Biol* **20**:1099–1103. doi:10.1016/j.cub.2010.04.045

1133 Wang Y, Jones BD, Brun YV. 2001. A set of ftsZ mutants blocked at different stages of cell division in
1134 Caulobacter. *Mol Microbiol* **40**:347–360. doi:10.1046/j.1365-2958.2001.02395.x
1135 West L, Yang D, Stephens C. 2002. Use of the Caulobacter crescentus Genome Sequence To Develop
1136 a Method for Systematic Genetic Mapping. *J Bacteriol* **184**:2155–2166.
1137 doi:10.1128/JB.184.8.2155-2166.2002
1138 Wiktor J, Gynnå AH, Leroy P, Larsson J, Coceano G, Testa I, Elf J. 2021. RecA finds homologous DNA
1139 by reduced dimensionality search. *Nature* **597**:426–429. doi:10.1038/s41586-021-03877-6
1140 Wilson GA, Vuina K, Sava G, Huard C, Meneguello L, Coulombe-Huntington J, Bertomeu T, Maizels
1141 RJ, Lauring J, Kriston-Vizi J, Tyers M, Ali S, Bertoli C, de Bruin RAM. 2023. Active growth
1142 signaling promotes senescence and cancer cell sensitivity to CDK7 inhibition. *Mol Cell*
1143 **83**:4078-4092.e6. doi:10.1016/j.molcel.2023.10.017
1144 Wiśniewski JR, Hein MY, Cox J, Mann M. 2014. A "Proteomic Ruler" for Protein Copy Number and
1145 Concentration Estimation without Spike-in Standards*. *Mol Cell Proteomics* **13**:3497–3506.
1146 doi:10.1074/mcp.M113.037309
1147 Withers HL, Bernander R. 1998. Characterization of dnaC2 and dnaC28 mutants by flow cytometry. *J*
1148 *Bacteriol* **180**:1624–1631. doi:10.1128/jb.180.7.1624-1631.1998
1149 Witz G, van Nimwegen E, Julou T. 2019. Initiation of chromosome replication controls both division
1150 and replication cycles in E. coli through a double-adder mechanism. *eLife* **8**:e48063.
1151 doi:10.7554/eLife.48063
1152 Wu Y, Liu Y, Lu C, Lei S, Li J, Du G. 2020. Quantitation of RNA by a fluorometric method using the
1153 SYTO RNASelect stain. *Anal Biochem* **606**:113857. doi:10.1016/j.ab.2020.113857
1154 Xiao H, Kalman M, Ikehara K, Zemel S, Glaser G, Cashel M. 1991. Residual guanosine 3',5'-
1155 bispyrophosphate synthetic activity of relA null mutants can be eliminated by spoT null
1156 mutations. *J Biol Chem* **266**:5980–5990. doi:10.1016/S0021-9258(19)67694-5
1157 Zatulovskiy E, Lanz MC, Zhang S, McCarthy F, Elias JE, Skotheim JM. 2022. Delineation of proteome
1158 changes driven by cell size and growth rate. *Front Cell Dev Biol* **10**.
1159 doi:10.3389/fcell.2022.980721
1160 Zheng H, Ho P-Y, Jiang M, Tang B, Liu W, Li D, Yu X, Kleckner NE, Amir A, Liu C. 2016. Interrogating
1161 the Escherichia coli cell cycle by cell dimension perturbations. *Proc Natl Acad Sci* **113**:15000–
1162 15005. doi:10.1073/pnas.1617932114
1163 Zhou Z, Siddiquee MMR, Tajbakhsh N, Liang J. 2020. UNet++: Redesigning Skip Connections to
1164 Exploit Multiscale Features in Image Segmentation. *IEEE Trans Med Imaging* **39**:1856–1867.
1165 doi:10.1109/TMI.2019.2959609
1166 Zhurinsky J, Leonhard K, Watt S, Marguerat S, Bähler J, Nurse P. 2010. A Coordinated Global Control
1167 over Cellular Transcription. *Curr Biol* **20**:2010–2015. doi:10.1016/j.cub.2010.10.002
1168

1169

1170

1171

1172

1173 **FIGURE LEGENDS**

1174 **Figure 1. Growth rate and genome copy number in *E. coli.***

1175 (**A**) Illustration of 1N (CRISPRi *oriC*, CJW7457) and multi-N (CRISPRi *ftsZ*, CJW7576) cells with different
1176 numbers of chromosomes along with representative microscopy images at different time points
1177 following CRISPRi induction. Scale bars: 1 µm. (**B**) Plot showing representative single-cell trajectories
1178 of cell area as a function of time for the CRISPRi strains following a block in DNA replication and/or
1179 cell division. (**C**) Plot showing the absolute growth rate as a function of cell area for 1N (32735
1180 datapoints from 1568 cells) and multi-N cells (14006 datapoints from 916 cells) in M9glyCAAT. Lines
1181 and shaded areas denote mean ± SD from three experiments. This also applies to the panels below.
1182 (**D**) Absolute and (**E**) relative growth rate in 1N (32735 datapoints from 1568 cells, CJW7457), multi-N
1183 (14006 datapoints from 916 cells, CJW7576), and *dnaC2* 1N (13933 datapoints from 1043 cells,
1184 CJW7374) cells as a function of cell area in M9glyCAAT. (**F**) Absolute growth rate and (**G**) relative
1185 growth rate in 1N (13933 datapoints from 1043 cells), 2N (6265 datapoints from 295 cells) and >2N
1186 (2116 datapoints from 95 cells) *dnaC2* (CJW7374) cells as a function of cell area in M9glyCAAT. (**H**)
1187 Absolute and (**I**) relative growth rate in 1N (50352 from 973 cells, CJW7457) and WT (80269 datapoints
1188 from 12544 cells, CJW7339) cells in M9gly. (**J**) Absolute and (**K**) relative growth rate in 1N (71736
1189 datapoints from 909 cells, CJW7457) and WT (63367 datapoints from 6880 cells, CJW7339) cells in
1190 M9ala. Lines and shaded areas denote mean ± SD from three biological replicates.

1191

1192 **Figure 2. Lower ribosome activity explains the reduced growth rate of 1N cells.** (**A**) RpsB-msfGFP
1193 fluorescence concentration in 1N (6542 cells, CJW7478) and multi-N (10537 cells, CJW7564) cells as a
1194 function of cell area. Lines and shaded areas denote mean ± SD from three experiments. (**B**) Relative

1195 protein concentration of different ribosomal proteins in 1N (SJ_XTL676) and multi-N (SJ_XTL229) cells
1196 by TMT-MS. 1N-rich cells were collected 0, 120, 180, 240 and 300 min after addition of 0.2% arabinose,
1197 while multi-N cells were collected after 0, 60, and 120 min of induction. Blue and cyan represent two
1198 independent experiments. Only proteins with at least four peptide measurements are plotted. (**C**)
1199 Apparent diffusion coefficients (D_a) of JF549-labeled RspB-HaloTag in WT (32,410 tracks from 771 cells,
1200 CJW7528), 1N (848,367 tracks from 2478 cells, CJW7529) and multi-N cells (107,095 tracks from 1139
1201 cells, CJW7530). Only tracks of length ≥9 displacements are included. 1N cells are color-binned
1202 according to their cell area while multi-N cells contain aggregated data for ~2-10 μm^2 cell areas. (**D**)
1203 D_a in WT cells fitted by a three-state Gaussian mixture model (GMM): 77 ± 1%, 20 ± 1%, and 3.2 ± 0.5%
1204 (±SEM) of the ribosome population, from the slowest moving to the fastest moving (32,410 tracks
1205 from 771 cells). (**E**) Example WT and 1N cells where (red, slow-moving) active and (gray, fast-moving)
1206 inactive ribosomes are classified according to the GMM. (**F**) Active (slow-moving) ribosome fraction
1207 in individual WT (237 cells) and 1N (2453 cells) cells as a function of cell area. Only cells with ≥50 tracks
1208 are included. Lines and shaded areas denote mean and 95% confidence interval (CI) of the mean from
1209 bootstrapping. (**G**) Same as (F) but for WT (237 cells) and multi-N (683 cells) cells. (**H**) Absolute growth
1210 rate of 1N and multi-N cells (Figure 1C) as a function of cell area was overlaid with the total active
1211 ribosome amount (calculated from Fig. 2A, F and G). Lines and shaded areas denote mean and 95% CI
1212 of the mean from bootstrapping.
1213
1214 **Figure 3. RNAP activity is reduced in 1N cells.** (**A**) RpoC-YFP fluorescence concentration in 1N (3580
1215 cells, CJW7477) and multi-N (5554 cells, CJW7563) cells as a function of cell area. Lines and shaded
1216 areas denote mean ± SD from 3 experiments. (**B**) Relative protein concentration of core RNAP subunits

1217 and σ^{70} in 1N-rich (SJ_XTL676) and multi-N (SJ_XTL229) cells by TMT-MS. 1N-rich cells were collected
1218 0, 120, 180, 240 and 300 min after addition of 0.2% L-arabinose, while multi-N cells were collected
1219 after 0, 60, and 120 min of induction. (**C**) Apparent diffusion coefficients of JF549-labeled RpoC-
1220 HaloTag in WT (91,280 tracks from 1000 cells, CJW7519), 1N (175,884 tracks from 1219 cells, CJW7520)
1221 and multi-N cells (186,951 tracks from 1040 cells, CJW7527). Only tracks of length ≥9 displacements
1222 are included. 1N cells are binned according to cell area while multi-N cells contain aggregated data
1223 for ~2-15 μm^2 cell areas. (**D**) D_a in WT cells fitted by a 3-state GMM: 49 ± 4%, 49 ± 4%, and 2 ± 0.1%
1224 (±SEM) of the RNAP population, from the slowest moving to the fastest moving (91,280 tracks from
1225 1,000 cells). (**E**) Example WT and 1N cells where (red, slow-moving) active and (gray, fast-moving)
1226 inactive RNAPs are classified according to the GMM. (**F**) Active RNAP fraction in individual WT (854
1227 cells) and 1N (1024 cells) cells as a function of cell area. Only cells with at least 50 tracks are included.
1228 Lines and shaded areas denote mean ± 95% CI of the mean from bootstrapping (3 experiments). (**G**)
1229 Same as (F) but for WT (854 cells) and multi-N (924 cells) cells. (**H**) Total amount of active RNAP in WT,
1230 1N and multi-N cells as a function of cell area (calculated from Fig. 3A, F and G). Also, shown is a linear
1231 fit to multi-N data ($f(x) = 4.16*10^4*x$, R^2 0.98). Lines and shaded areas denote mean and 95% CI of the
1232 mean from bootstrapping. All microscopy data are from three biological replicates.
1233

1234 **Figure 4. Mathematical modeling and RNASelect concentration measurements in 1N and multi-N**
1235 **cells.** (**A-C**) Plots comparing simulation results of model A (solid lines) with experimental data points
1236 (dots) and averages (open squares) in the M9glyCAAT condition. The multi-N and 1N cells are
1237 indicated as blue and yellow, respectively: (**A**) The relation between the absolute growth rate ($\frac{dA}{dt}$) and
1238 cell area (A). (**B**) The relation between the active RNAP fraction and cell area. (**C**) The relation between

1239 the active ribosome fraction and cell area. (**D**) A two-dimensional diagram showing how the fractions
1240 of active RNAPs and ribosomes change with DNA concentration (colored from blue to yellow).
1241 Experimental data (with 2D error bars) from multi-N and 1N cells were combined and shown in the
1242 same plot. Simulated results (filled dots) are based on model A. (**E**) Plot showing the effect of DNA
1243 limitation using the ODE model A, with respect to the decay of DNA concentration, mRNA
1244 concentration and relative growth rate in 1N cells. Each quantity was normalized to their value at
1245 normal cell size (cell area = 2.5 μm^2). (**F**) The phase contrast (top), HU-mCherry (middle) and SYTO
1246 RNASelect fluorescence (bottom) images of two representative cells from a mixed population of 1N
1247 (CRISPRi *oriC*, CJW7457) and multi-N (CRISPRi *ftsZ*, CJW7576) cells. The purple and orange ticks In the
1248 SYTO RNASelect colorbar correspond to the average fluorescence (concentration proxy) of the multi-
1249 N and the 1N cell respectively. (**G**) SYTO RNASelect concentration distributions for 1N and multi-N
1250 cells (3077 cells for each population from five biological replicates). (**H**) The average 1N/multi-N SYTO
1251 RNASelect concentration ratio (gray bar) calculated from five biological replicates (white circles). (**I**)
1252 RNASelect concentration ratio as a function of cell area (Mean +/- SD from five biological replicates).
1253 A single exponential decay function was fitted to the average ratios (R^2 = 97%). All RpoC-HaloTag-
1254 JF549 concentration comparisons or ratio calculations were performed for equal numbers of 1N and
1255 multi-N cells and overlapping cell area distributions (Figure 4 – supplement 4A).
1256
1257 **Figure 5. Proteome and transcriptome remodeling in 1N-rich cells. (A)** Schematic explaining the
1258 calculation of the protein slopes, which describes the scaling of the relative protein concentration
1259 with cell area. **(B)** Plot showing the protein scaling (average slopes from 2 reproducible biological
1260 replicates, see also Figure 5 – supplement 1A-B) in 1N (x-axis) and multi-N (y-axis) cells across the

1261 proteome (2360 proteins). The colormaps correspond to a Gaussian kernel density estimation (KDE).
1262 **(C)** Plot showing the first principal component (PC1, which explains 69% of the total variance
1263 considering both 1N-rich and multi-N cells) used to reduce the dimensionality of the relative protein
1264 concentration during cell growth. The x-axis corresponds to the log-transformed cell area, whereas
1265 the marker size shows the cell area increase in linear scale. **(D)** Relationship between the absolute
1266 distance of a gene from *oriC* and the slope of the protein it encodes. Data from 2268 proteins are
1267 shown (grey markers), as well as binned data in six gene distance bins (open circles, average +/- SEM,
1268 ~370 proteins per bin). For the multi-N cells, the Spearman correlation was not significant (ρ = NS, p-
1269 value > 0.01), whereas for the 1N cells, a significant Spearman correlation ($\rho = 0.23$, p-value < 10^{-10})
1270 for genes within 1.35 Mbps of *oriC* (below the mid-point of the 4th gene distance bin). **(E)** Relationship
1271 between the distance of a gene from *oriC* and the ion intensity of its encoded protein. The protein ion
1272 intensity was divided by the protein sequence length and the quotient was log-transformed. Data
1273 from 2258 proteins are shown (grey markers) as well as binned data (open circles, average +/- SEM,
1274 ~370 proteins per bin). The spearman correlation is not significant (ρ = NS, p-value > 0.01). **(F)**
1275 Correlation between average protein and mRNA slopes across the genome (2324 genes).
1276

1277 **SUPPLEMENTARY FIGURE LEGENDS**

1278 **Figure 1 – figure supplement 1. Relationships between growth rate and cell volume across several**
1279 **growth conditions and cell types of different ploidy.** (**A**) Cell width in WT (59072 datapoints from
1280 7640 cells, CJW7339), 1N (41313 datapoints from 1585 cells, CJW7477), and multi-N (18489
1281 datapoints from 915 cells, CJW7563) cells in M9GlyCAAT as a function of cell area. Lines and shaded
1282 areas denote mean ± SD from 3 biological replicates. (**B**) Absolute and (**C**) relative growth rate based

1283 on cell volume in 1N (32735 datapoints from 1568 cells, CJW7457), multi-N (14006 datapoints from
1284 916 cells, CJW7576), and *dnaC2* 1N (13933 datapoints from 1043 cells, CJW7374) cells as a function
1285 of cell volume in M9glyCAAT. Lines and shaded areas denote mean ± SD from three experiments. The
1286 growth rates are based on volume in this figure. (**D**) Absolute and (**E**) relative growth rate in
1287 M9glyCAAT in 1N (32735 datapoints from 1568 cells, CJW7457), multi-N (14006 datapoints from 916
1288 cells, CJW7576) and WT (19495 datapoints from 7440 cells, CJW7339) cells as a function of cell area.
1289 (**F**) Absolute growth rate and (**G**) relative growth rate in 1N (13933 datapoints from 1043 cells), 2N
1290 (6265 datapoints from 295 cells) and >2N (2116 datapoints from 95 cells) *dnaC2* (CJW7374) cells as a
1291 function of cell area in M9glyCAAT. (**H**) Absolute and (**I**) relative growth rate in 1N (50352 from 973
1292 cells, CJW7457) and WT (80269 datapoints from 12544 cells, CJW7339) cells in M9gly. (**J**) Absolute
1293 and (**K**) relative growth rate in 1N (71736 datapoints from 909 cells, CJW7457) and WT (63367
1294 datapoints from 6880 cells, CJW7339) cells in M9ala. Lines and shaded areas denote mean ± SD from
1295 three biological replicates.
1296
1297 **Figure 1 – figure supplement 2. Relationships between growth rate and cell area in cell types of**
1298 **different ploidy.** (**A**) Absolute and (**B**) relative growth rate growth rate in M9glyCAAT in 1N (32735
1299 datapoints from 1568 cells, CJW7457), multi-N (14006 datapoints from 916 cells, CJW7576) and WT
1300 (19495 datapoints from 7440 cells, CJW7339) cells as a function of cell area. Lines and shaded areas
1301 denote mean ± SD from three biological replicates.
1302
1303 **Figure 1 – figure supplement 3. Characterization of ploidy in different cell types.** (**A**) Representative
1304 microscopy images of CRISPRi *oriC* cells expressing HU-CFP and ParB-mCherry with *parS* site at *ori1*

1305 (CJW7517) in M9glyCAAT 210 min after addition of 0.2% L-arabinose. Scale bar: 1 µm. (**B**)
1306 Representative microscopy images of WT (top) and *dnaC2* (bottom) cells expressing HU-mCherry
1307 growing under microscope observation in M9glyCAAT. DNA replication in *dnaC2* cells was blocked by
1308 growing cells at 37°C for 145 min. Arrows indicate *dnaC2* cells with one (1N) or two (2N) nucleoids.
1309 Scale bar: 1 µm. (**C**) Graph showing the percentage of *dnaC2* cells (CJW7374) with 1, 2 or >2 nucleoids
1310 after growth at 37°C. Shown are aggregated data from three biological replicates.

1311

1312 **Figure 1 – figure supplement 4. Determination of absolute growth rate of ppGpp^0 (CJW7518) and**
1313 **Δ*recA* (CJW7522) cells grown in M9glyCAAT as a function of cell area.** Lines and shaded areas denote
1314 mean ± SD from two biological replicates. Also shown are the data for 1N (CJW7457) and multi-N
1315 (CJW7576) cells from Figure 1C.

1316

1317 **Figure 1 – figure supplement 5. Validation of stable growth conditions under microscope**
1318 **observation.** (**A**) Plot showin the absolute growth rate of 1N (CJW7457) cells grown 90 min in a liquid
1319 M9glyCAAT culture in the presence of 0.2% L-arabinose and then transferred to an agarose pad and
1320 imaged for 2 h. The data for 1N (CJW7457) and multi-N (CJW7576) cells presented in Figure 1C are
1321 also shown for comparison; these cells were grown on an agarose pad for 6 h. Lines and shaded areas
1322 denote mean ± SD from two biological replicates. (**B**) Plot showing the relative growth rate of WT
1323 (CJW7339) cells in M9glyCAAT grown after placing them on an agarose pad. Lines and shaded areas
1324 denote mean ± SD from three biological replicates.

1325

1326 **Figure 1 – figure supplement 6. DNA-dependent growth in *Caulobacter crescentus*.** (**A**) Plot showing
1327 the absolute and (**B**) relative growth rate of 1N (DnaA depletion, strain CJW4823, 87 cells) and multi-
1328 N (FtsZ depletion, strain CJW3673, 181 cells) *C. crescentus* as a function of cell area. Lines and shaded
1329 areas denote mean ± SD from three biological replicates. (**C**) Example images of 1N and multi-N *C.*
1330 *crescentus* cells with ploidy distinguished by the number of ParB-eCFP foci. Scale bar: 2 µm.
1331
1332 **Figure 2 – figure supplement 1. Determination of RpsB-msfGFP concentration in 1N cells.** Plot
1333 showing the RpsB-msfGFP fluorescence concentration in 1N (CJW7478) cells grown in (**A**) M9gly (from
1334 three experiments) or (**B**) M9ala (from two experiments) as a function of cell area. Lines and shaded
1335 areas denote mean ± SD between the biological replicates.
1336
1337 **Figure 2 – figure supplement 2. Diffusive characteristics of labeled ribosomes in rifampicin-treated**
1338 **WT cells.** (**A**) Plot showing the probability density of apparent diffusion coefficients (D_a) of JF549-
1339 labeled RpsB-HaloTag in WT cells (CJW7528) treated with 200 µg/mL rifampicin for 30 min. Only tracks
1340 of length ≥10 are included. Also shown is D_a fitted by three-state Gaussian mixture model (GMM)
1341 (mean ± SEM). Data are from three biological replicates.
1342
1343 **Figure 2 – figure supplement 3. Diffusive characteristics of labeled ribosomes in 1N cells as a**
1344 **function of cell area.** Plots showing the probability density of apparent diffusion coefficients (D_a) of
1345 JF549-labeled RpsB-HaloTag in 1N cells (CJW7529) in M9glyCAAT at different cell areas. Also shown is
1346 D_a fitted by three-state Gaussian mixture model (GMM). Only tracks of length ≥10 are included. Data
1347 are from three biological replicates.

1348 **Figure 2 – figure supplement 4. Characterization of ribosome diffusion and active fraction in poor**
1349 **media conditions.** (**A**) Plot showing the probability density of apparent diffusion coefficients (D_a) of
1350 JF549-labeled RpsB-HaloTag across cell areas for WT (CJW7528) and 1N (CJW7529) cells grown in
1351 M9gly. Only tracks of length ≥10 are included. 1N cells were binned according to cell area. (**B**) Same
1352 as (A) for cells grown in M9ala. (**C**) Plot showing probability density of D_a of JF549-labeled RpsB-
1353 HaloTag in WT cells (CJW7528) grown M9gly. Only tracks of length ≥10 are included. Also shown is D_a
1354 fitted by three-state Gaussian mixture model (GMM) (mean ± SEM). (**D**) Same as (C) but for cells grown
1355 in M9ala. (**E**) Plot showing the fraction of active ribosomes as a function of cell area for individual WT
1356 (CJW7528) and 1N (CJW7529) cells (dots) grown in M9gly. Only cells with ≥50 tracks are included.
1357 Shaded areas denote 95% confidence interval (CI) of the mean from bootstrapping. (**F**) same as (E)
1358 but for cells grown in M9ala. (**G**) Plot showing the total active ribosome amount (left y-axis) and the
1359 absolute growth rate (right y-axis) of 1N and multi-N cells (from Figure 1C) grown in M9gly as a
1360 function of cell area. The total amount of active ribosomes was calculated by multiplying the total
1361 amount of ribosomes by the fraction of active ribosomes. Also, shown is a linear fit to WT data (f(x) =
1362 $2.99*10^4*x$, R^2 0.97). Lines and shaded areas denote mean and 95% CI of the mean from
1363 bootstrapping. All data are from three biological replicates. (**H**) Same as (G) but for cells grown in
1364 M9Ala. Here the linear fit to the WT data is f(x) = $1.90*10^4*x$, R^2 0.99.
1365
1366 **Figure 3 – figure supplement 1. Determination of RpoC-YFP concentration in 1N cells.** (**A**) Plot
1367 showing the RpoC-YFP fluorescence concentration in 1N (CJW7477) cells grown in M9gly (three
1368 experiments) as a function of cell area. Lines and shaded areas denote mean ± SD between biological
1369 replicates. (**B**) Same as (A) but for 1N cells grown in M9ala (three experiments).

1370 **Figure 3 – figure supplement 2. Diffusive characteristics of labeled RNAPs in rifampicin-treated WT**
1371 **cells.** Plot showing the probability density of apparent diffusion coefficients (D_a) of JF549-labeled
1372 RpoC-HaloTag in WT cells (CJW7519) treated with 200 µg/mL rifampicin for 30 min. Also shown is D_a
1373 fitted by three-state Gaussian mixture model (GMM) (mean ± SEM). Only tracks of length ≥10 are
1374 included. Data are from three biological replicates.
1375
1376 **Figure 3 – figure supplement 3. Diffusive characteristics of labeled RNAPs in 1N cells of different cell**
1377 **areas.** Plots showing the apparent diffusion coefficients (D_a) of JF549-labeled RpoC-HaloTag in 1N cells
1378 (CJW7520) of different cell areas. Cells were grown in M9glyCAAT. Also shown is D_a fitted by three-
1379 state Gaussian mixture model (GMM). Only tracks of length ≥10 are included. Data is from three
1380 biological replicates.
1381
1382 **Figure 3 – figure supplement 4. Characterization of RNAP diffusion and active fraction in poor media**
1383 **conditions.** (**A**) Plot showing the probability densities of apparent diffusion coefficients (D_a) of JF549-
1384 labeled RpoC-HaloTag in WT (CJW7519) and 1N (CJW7520) cells grown in M9gly. Only tracks of length
1385 ≥10 are included. 1N cells were binned according to cell area. (**B**) Same as (A) but for cells grown in
1386 M9ala. (**C**) Plot showing the probability density of D_a of JF549-labeled RpoC-HaloTag in WT cells
1387 (CJW7519) grown in M9gly. Also shown is D_a fitted by three-state Gaussian mixture model (GMM)
1388 (mean ± SEM). (D) Same as (C) but for cells grown in M9ala. (E) Plots showing the fraction of active
1389 RNAPs in individual WT (CJW7519) and 1N (CJW7520) cells (dots) grown in M9gly as a function of cell
1390 area. Only cells with ≥50 tracks are included. (**F**) Same as (E) but for cells grown in M9ala. (**G**) Plot
1391 showing the total amount of active RNAPs was calculated by multiplying the total amount of RNAPs

1392 by the fraction of active RNAPs in WT and 1N cells grown in M9gly as a function of cell area. Also,
1393 shown is a linear fit to WT data (f(x) = $3.99*10^4*x$, R^2 0.90). Shaded areas denote 95% confidence
1394 interval (CI) of the mean from bootstrapping. All data are from three biological replicates. (**H**) Same
1395 as (G) but for cells grown in M9ala. Here, the linear fit for WT data is f(x) = $3.21*10^4*x$, R^2 0.95.
1396

1397 **Figure 3 – figure supplement 5. Determination of the relative Rsd concentration in 1N-rich and**
1398 **multi-N cells as a function of cell area.** Plots showing the relative protein concentration of Rsd in 1N-
1399 rich (SJ_XTL676) and multi-N (SJ_XTL229) cells as determined by TMT-MS. 1N-rich cells grown in
1400 M9glyCAAT were collected 0, 120, 180, 240 and 300 min, while multi-N cells were collected 0, 60, and
1401 120 min after 0.2% L-arabinose induction of CRISPRi. Different shades of gray represent two
1402 independent experiments.
1403

1404 **Figure 4 – figure supplement 1. Comparison between experimental results from the M9glyCAAT**
1405 **condition and simulation results using model B.** (**A-C**) Plots comparing simulation results of model B
1406 (solid lines) with experimental data (dots) and averages (open squares) in the M9glyCAAT condition.
1407 The multi-N and 1N cells are indicated as blue and yellow, respectively: (**A**) The relation between the
1408 absolute growth rate ($\frac{dA}{dt}$) and cell area (A). (**B**) The relation between the active RNAP fraction and cell
1409 area. (**C**) The relation between the active ribosome fraction and cell area. (**D**) A two-dimensional
1410 diagram showing how the fractions of active RNAPs and ribosomes change with DNA concentration
1411 (colored from blue to yellow). Experimental data (with 2D error bars) from multi-N and 1N cells were
1412 combined and shown in the same plot.
1413

1414 **Figure 4 – figure supplement 2. Comparison between experimental results from the M9gly and**
1415 **M9ala conditions and simulation results using model A.** (**A-C**) Plots comparing simulation results of
1416 model A (solid lines) with experimental data (dots) and averages (open squares) in the M9gly
1417 condition. The wild-type and 1N cells are indicated as black and yellow, respectively. (**D-F**) Plots
1418 comparing simulation results of model A (solid lines) with experimental data (dots) and averages
1419 (open squares) in the M9ala condition. The wild-type and 1N cells are indicated as black and yellow,
1420 respectively. (**A,D**) The relation between the absolute growth rate ($\frac{dA}{dt}$) and cell area (A). (**B,E**) The
1421 relation between the active RNAP fraction and cell area. (**C,F**) The relation between the active
1422 ribosome fraction and cell area.
1423
1424 **Figure 4 – figure supplement 3. Model A-based simulations examining the effects of varying the**
1425 **rates in either mRNA synthesis or mRNA degradation on the relative growth rate of 1N cells as a**
1426 **function of cell area.** (**A**) Plot showing the decay of DNA concentration (black) and of the relative
1427 growth rate (blue) in 1N cells when the rate of bulk mRNA synthesis rate r_1 increase or decreases by
1428 ten-fold. Each quantity was normalized to its value at normal cell size (cell area = 2.5 μm^2). (**B**) Same
1429 as (A) except mRNA degradation rate δ increasing or decreasing by ten-fold.
1430
1431 **Figure 4 – figure supplement 4. Cell sampling to match cell size distribution in mixed populations of**
1432 **1N and multi-N cells.** Comparison of the cell area distributions of 1N and multi-N cells before and
1433 after random sampling. Single cells were sampled for each biological replicate and cell area bin such
1434 that the area distributions and numbers of 1N and multi-N cells overlapped. Bins with less than 50
1435 cells from either population were removed from the analysis. Cell area distributions from mixed

1436 CJW7457 (CRISPRi *oriC*) and CJW7576 (CRISPRi *ftsZ*) populations stained with SYTO RNASelect
1437 (aggregated data from five biological replicates)
1438
1439 **Figure 4 – figure supplement 5. Comparison of RpoC-HaloTag-JF549 labelling between 1N and multi-**
1440 **N cells.** (**A**) Phase contrast (left) and RpoC-HaloTag-JF549 fluorescence (right) images of two
1441 representative cells from a mixed population of 1N (CRISPRi *oriC*, CJW7520) and multi-N (CRISPRi *ftsZ*,
1442 CJW7527) cells. The blue and orange ticks In the RpoC-HaloTag-JF549 color bar correspond to the
1443 average fluorescence (concentration proxy) of the multi-N and the 1N cell, respectively. (**B**) Same as
1444 Figure 4– figure supplement 4, except for CJW7520 (CRISPRi *oriC*) and CJW7527 (CRISPRi *ftsZ*) cells in
1445 which RpoC-HaloTag was stained with the JF549 dye (aggregated data from two biological replicates).
1446 (**C**) Distributions of RpoC-HaloTag-JF549 concentration for 1N and multi-N cells (748 cells for each
1447 population from two biological replicates). (**D**) Average 1N/multi-N RpoC-HaloTag-JF549
1448 concentration ratio (gray bar) calculated from two biological replicates (white circles) after sampling
1449 the same number of cells per biological replicate and cell area bin for each population (see Materials
1450 and Methods). (**E**) Plot showing the concentration ratio of fluorescently labeled RpoC derivatives
1451 between 1N and multi-N cells versus the cell area. Squares show mean ± full range of RpoC-HaloTag-
1452 JF549 signal concentration ratios from two biological replicates, whereas grey circles indicate the
1453 mean signal concentration ratio of RpoC-YFP (from data shown in Figure 3A) for comparison. A linear
1454 regression (red dashed line) was fitted to the average RpoC-HaloTag-JF549 ratios. A cell area of ~2.8
1455 μm^2 corresponds to a 1N/multi-N RpoC-HaloTag-JF549 concentration ratio equal to 1.
1456

1457 **Figure 5 – figure supplement 1. Comparison of protein and mRNA scaling between biological**
1458 **replicates.** (**A**) Correlation of protein slopes across the proteome (2360 proteins) between two
1459 biological replicates for 1N cells. The indicated Spearman correlation (ρ) is significant (p-value < 10^{-10}.
1460 (**B**) Same as (A) but for multi-N cells. (**C**) Correlation of RNA slopes across the genome (3446 mRNAs)
1461 between two biological replicates for 1N cells. The indicated Spearman correlation shown (ρ) is
1462 significant (p-value < 10^{-10}).
1463

1464 **Figure 5 – figure supplement 2. Protein slopes relative to protein ion intensity for 1N-rich cells.** The
1465 summed ion intensity of each protein was divided by the protein sequence length and the quotient
1466 was log-transformed. The locations of selected proteins are annotated.
1467

1468 **Table 1: Model parameter description**
1469

Para-meter	Biological meaning	Unit	Description
r_1	$\frac{\text{bulk transcription rate}}{\text{total protein number}}$	10^{-3}/min	This parameter was estimated as $r_1 = \theta_{RNAP}\beta_{mRNA} / T_{RNAP}$, where θ_{RNAP} is the number of RNAPs normalized by the number of proteins; β_{mRNA} is the fraction of RNAPs engaged in transcription, and T_{RNAP} is the mean mRNA synthesis time.
r_2	$\frac{\text{bulk translation rate}}{\text{total protein number}}$	10^{-3}/min	This parameter was estimated by $r_2 = \theta_{ribo} / T_{ribo}$, where θ_{ribo} is the number of ribosomes normalized by the number of proteins, and T_{ribo} is the mean protein synthesis time.
K_1	Saturation level of DNA with respect to RNAP binding	$1/\mu m^3$	This parameter was estimates from $\alpha_{RNAP} = \frac{[Z]}{K_1+[Z]}$, where α_{RNAP} is measured in this work and $[Z]_{avg}$, the mean genome copy.
K_2	Saturation level of mRNA with respect to ribosome binding	$1/\mu m^3$	This parameter was estimated as $\alpha_{ribo} = \frac{[X]}{K_2+[X]}$, where α_{ribo} is measured in this work and $[X]$, the mRNA concentration.

δ	mRNA degradation rate	1/min	$\delta = 1/\tau_L$, where τ_L is the mRNA lifetime
c	$\frac{\text{cell volume}}{\text{protein number}}$	$10^{-6}\mu m^3$	Cell volumes of different culture conditions were measured in this work.
c'	$\frac{\text{cell area}}{\text{protein number}}$	$10^{-6}\mu m^2$	Cell area of different culture conditions were measured in this work.
$[Z]_{avg}$	Average genome concentration of normal-growing cells	genome/ μm^3	Estimated by averaging the genome concentration over the cell cycle, see Appendix 1 for details.

1470
1471
1472
1473 **Table 2: Initial and optimized model parameters**
1474

Para-meter	Unit	Initial estimation			Optimized parameters			
		M9gly CAA	M9gly	M9ala	M9glyCAA (model A)	M9glyCAA (model B)	M9gly (model A)	M9ala (model A)
r_1	10^{-3}/min	1.99	0.89	0.60	1.22	1.76	0.64	0.46
r_2	10^{-3}/min	20.0	8.21	3.70	22.4	22.5	15.3	13.6
K_1	1/ μm^3	1.40	2.99	3.03	1.17	1.55	3.02	2.78
K_2	1/ μm^3	622	1807	1467	797	532	1836	1513
δ	1/min	0.96	0.96	0.96	1.27	1.31	1.02	0.79
c	$10^{-6}\mu m^3$	0.28	0.39	0.53	0.28	0.18	0.15	0.30
c'	$10^{-6}\mu m^2$	0.47	0.62	1.06	-	-	-	-
X_{ini}	10^2/cell	20.2	7.21	3.17	-	-	-	-
Y_{ini}	10^6/cell	3.82	1.77	0.95	-	-	-	-
$[Z]_{avg}$	genome /cell	1.40	1.99	2.02	-	-	-	-

1475

1476 **Table 3. Strains used in this study**. The abbreviations *kan*, *cat*, and *spec* refer to gene cassette
1477 insertions conferring resistance to kanamycin, chloramphenicol, and spectinomycin, respectively.
1478 These insertions are flanked by Flp site-specific recombination sites (*frt*) that allow the removal of the
1479 insertion using Flp recombinase from plasmid pCP20 (Cherepanov and Wackernagel, 1995).
1480

Identifier	Genotype	Source
CJW2591	CB15N Δ*bla6 ftsZ*::pBGent-pXyl-ftsZ	BamHI/HindIII fragment was cut from YF1585 and cloned into pBGent. The

		resulting plasmid was integrated into LS107 (Wang et al., 2001).
CJW3673	CB15N *ftsZ*::pBGentpXyl-ftsZ *parB*::*ecfp-parB*	UV-inactivated ϕCr30 phage lysate was prepared from CJW2591 and transduced into MT190.
CJW4823	CB15N *parB*::*ecfp-parB dnaA*::Ω xylX::pGM2195	UV-inactivated ϕCr30 phage lysate was prepared from GM2471. First, pGM2195 was transduced into MT190, followed by a second transduction of Ω into the resulting strain to disrupt the endogenous *dnaA* gene.
CJW6737	DH5α/pKFSS1_parS^{pMT1}	parS^{pMT1} was amplified from FH3518 (Nielsen et al., 2006) using oligonucleotides NT157 and NT158, digested with BamHI and KpnI, and cloned into the BamHI/KpnI sites of pKFSS1_2 (Takacs et al., 2018).
CJW7019	MG1655 *rpsB*::*rpsB-msfgfp-kan*	(Gray et al., 2019)
CJW7079	CB15N *rplA(L1)*::*rplA(L1)-mCherry*	CJW7080 was subjected to counterselection on 0.3% xylose.
CJW7080	CB15N *rplA(L1)*::pNPTS138-rplA(L1)-mCherry-rplA(L1)DOWN	The vector pNPTS138 (M. R. Alley, unpublished) was PCR-amplified using oligomers JSG_018 and JSG_019. A ~500-bp fragment of the 3' end of the *rplA(L1)* gene, and a ~500 bp fragment immediately downstream of the *rplA* gene (rplA(L1)DOWN), were amplified from a CB15N genome template using oligomers JSG_024 and JSG_025, and JSG_020 and JSG_021, respectively. *mCherry* was amplified from MTLS4218 (Thanbichler et al., 2007) and a linker was introduced using JSG_022 and JSG_023. All products were assembled into a plasmid via Gibson assembly. The resulting plasmid, which was verified by sequencing junctions, was transformed into S17-1 and introduced into CB15N by conjugation with selection for

		kanamycin and nalidixic acid resistance.
CJW7339	MG1655 *hupA*::*hupA-mCherry-kan*	*hupA*::*hupA-mCherry-kan* from CJW5556 (Paintdakhi et al., 2016) was moved into MG1655 by P1 transduction.
CJW7374	MG1655 *hupA*::*hupA-mCherry dnaC*::*dnaC2(ts) mdoB*::*kan*	The kanamycin resistance cassette was excised from CJW7339 by expressing the Flp site-specific recombinase from pCP20 (Cherepanov and Wackernagel, 1995). *dnaC*::*dnaC2(ts) mdoB*::*kan* from FW1957 (Wu et al. 2010) was subsequently moved into this strain by P1 transduction.
CJW7411	MG1655 *glmS1868*::*parS(pMT1)-frt-kanR-frt*	Plasmid backbone was amplified from CJW6919 (Kim et al., 2019) using oligonucleotides AP0039 and AP0040, pMT1 *parS* was amplified from CJW6737 using AP0041 and AP0042, and the fragments were ligated by Gibson assembly. *parS(pMT1)-frt-kanR-frt* was amplified from the resulting plasmid with AP0078 and AP0079. The amplicon was inserted between *glmS* and *pstS* by λ-red mediated recombination (Datsenko and Wanner, 2000).
CJW7457	MG1655 *lacY(A177C) araFGH*::*spec ΔlacI ΔaraE araBAD*::*dCas9 galM<PBBa-J23119-sgRNA(oriC)-(S. pyogenes terminator)-(rrnB terminator)>gmpA hupA*::*hupA-mCherry-kan*	*hupA*::*hupA-mCherry-kan* from CJW5556 (Paintdakhi et al., 2016) was moved into SJ_XTL676 by P1 transduction.
CJW7473	CB15N *rplA(L1)*::*rplA(L1)-mCherry ftsZ*::pBGentpXyl-ftsZ	UV-inactivated ϕCr30 phage lysate was prepared from CJW7080 and used for transduction into CJW3673. Tranductants were selected on kanamycin, and then counterselected on 0.3 % xylose.
CJW7477	MG1655 *lacY(A177C) araFGH*::*spec ΔlacI ΔaraE*	The kanamycin resistance cassette was excised from CJW7457 by

	araBAD::*dCas9 galM<PBBa-J23119-sgRNA(oriC)-(S. pyogenes terminator)-(rrnB terminator)>gmpA hupA*::*hupA-mCherry rpoC*::*rpoC-ygfp-kan*	expressing the Flp site-specific recombinase from pCP20 (Cherepanov and Wackernagel, 1995). *rpoC*::*rpoC-ygfp-kan* from RLG7470 was subsequently moved into this strain by P1 transduction.
CJW7478	MG1655 *lacY(A177C) araFGH*::*spec ΔlacI ΔaraE araBAD*::*dCas9 galM<PBBa-J23119-sgRNA(oriC)-(S. pyogenes terminator)-(rrnB terminator)>gmpA hupA*::*hupA-mCherry rpsB*::*rpsB-msfgfp-kan*	The kanamycin resistance cassette was excised from CJW7457 by expressing the Flp site-specific recombinase from pCP20 (Cherepanov and Wackernagel, 1995). *rpsB*::*rpsB-msfgfp-kan* from CJW7019 was subsequently moved into this strain by P1 transduction.
CJW7500	CB15N *rplA(L1)*::*rplA(L1)-mCherry dnaA*::Ω xylX::pGM2195	UV-inactivated ϕCr30 phage lysate was prepared from GM2471. A double transduction was performed into CJW7079.
CJW7517	MG1655 *lacY(A177C) araFGH*::*spec ΔlacI ΔaraE araBAD*::*dCas9 galM<PBBa-J23119-sgRNA(oriC)-(S. pyogenes terminator)-(rrnB terminator)>gmpA gtrA*::*P58-mCherry-parB(pMT1) parS(pMT1) at ori1 hupB*::*hupB-cfp-kan*	The strain was generated by first moving *gtrA*::*P58-mCherry-parB(pMT1)-cat* (Wiktor et al., 2021) into SJ_XTL676 by P1 transduction. Next, *parS(pMT1)-kan* at *ori1* from CJW7411 was moved into the strain by P1 transduction. The resistance genes were excised by expressing the Flp site-specific recombinase from pCP20 (Cherepanov and Wackernagel, 1995). Finally, *hupB*::*hupB-cfp-kan* from CJW4656 (Gray et al., 2019) was moved into the strain by P1 transduction.
CJW7518	MG1655 *lacY(A177C) araFGH*::*spec ΔlacI ΔaraE araBAD*::*dCas9 galM<PBBa-J23119-sgRNA(oriC)-(S. pyogenes terminator)-(rrnB terminator)>gmpA hupA*::*hupA-mcherry ΔrelA251*::*kan ΔspoT207*::*cat*	The kanamycin resistance cassette was excised from CJW7457 by expressing the Flp site-specific recombinase from pCP20 (Cherepanov and Wackernagel, 1995). *ΔrelA251*::*kan* and *ΔspoT207*::*cat* were subsequently moved into this strain by two P1 transductions from strain CF1693 (Xiao et al., 1991).

CJW7519	MG1655 *rpoC*::*rpoC-HaloTag-kan*	The strain was generated by first creating *rpoC-HaloTag-kan* amplicon with oligonucleotides JSG_148 and JSG_149 from strain JM41 (Mäkelä and Sherratt, 2020). This amplicon was used to replace the endogenous *rpoC* by λ-red mediated recombination (Datsenko and Wanner, 2000). Finally, *rpoC*::*rpoC-HaloTag-kan* was moved into MG1655 by P1 transduction.
CJW7520	MG1655 *lacY(A177C) araFGH*::*spec ΔlacI ΔaraE araBAD*::*dCas9 galM<PBBa-J23119-sgRNA(oriC)-(S. pyogenes terminator)-(rrnB terminator)>gmpA rpoC*::*rpoC-HaloTag-kan*	*rpoC*::*rpoC-HaloTag-kan* from CJW7519 was moved into SJ_XTL676 by P1 transduction.
CJW7522	MG1655 *lacY(A177C) araFGH*::*spec ΔlacI ΔaraE araBAD*::*dCas9 galM<PBBa-J23119-sgRNA(oriC)-(S. pyogenes terminator)-(rrnB terminator)>gmpA hupA*::*hupA-mCherry ΔrecA*::*kan*	*recA* was replaced by *kan* using oligonucleotides JSG_173 and JSG_174 in MG1655 by λ-red mediated recombination (Datsenko and Wanner, 2000). The kanamycin resistance cassette was excised from CJW7457 by expressing the Flp site-specific recombinase from pCP20 (Cherepanov and Wackernagel, 1995) and *ΔrecA*::*kan* was subsequently moved into the strain by P1 transduction.
CJW7527	MG1655 *lacY(A177C) araFGH*::*spec ΔlacI ΔaraE araBAD*::*dCas9 galM<PBBa-J23119-sgRNA(ftsZ)-(S. pyogenes terminator)-(rrnB terminator)>gmpA rpoC*::*rpoC-HaloTag-kan*	*rpoC*::*rpoC-HaloTag-kan* from CJW7519 was moved into SJ_XTL229 by P1 transduction.
CJW7528	MG1655 *rpsB*::*rpsB-HaloTag-kan*	The strain was generated by first creating *rpsB-HaloTag-kan* amplicon with oligonucleotides JSG_157 and JSG_158 from strain JM41 (Mäkelä and Sherratt, 2020). This amplicon was used to replace the endogenous *rpsB* by λ-red mediated

		recombination (Datsenko and Wanner, 2000). Finally, *rpsB*::*rpsB-HaloTag-kan* was moved into MG1655 by P1 transduction.
CJW7529	MG1655 *lacY(A177C) araFGH*::*spec ΔlacI ΔaraE araBAD*::*dCas9 galM<PBBa-J23119-sgRNA(oriC)-(S. pyogenes terminator)-(rrnB terminator)>gmpA rpsB*::*rpsB-HaloTag-kan*	*rpsB*::*rpsB-HaloTag-kan* from CJW7528 was moved into SJ_XTL676 by P1 transduction.
CJW7530	MG1655 *lacY(A177C) araFGH*::*spec ΔlacI ΔaraE araBAD*::*dCas9 galM<PBBa-J23119-sgRNA(ftsZ)-(S. pyogenes terminator)-(rrnB terminator)>gmpA rpsB*::*rpsB-HaloTag-kan*	*rpsB*::*rpsB-HaloTag-kan* from CJW7528 was moved into SJ_XTL229 by P1 transduction.
CJW7531	CB15N *rpoC*::*mCherry-rpoC*	Two DNA segments of vector pNPTS138 (M. R. Alley, unpublished) were PCR-amplified using oligomers JSG_134 and JSG_137, and JSG_135 and JSG_136. A ~900 bp fragment upstream of the *rpoC* gene and ~900 bp of the 5' end of *rpoC* were amplified from a CB15N genome template using oligomers JSG_128 and JSG_129, and JSG_132 and JSG_133, respectively. *mCherry* was amplified from MTLS#4218 (Thanbichler et al., 2007) and a linker was introduced using oligomers JSG_130 and JSG_131. All products were assembled into a plasmid via Gibson assembly. Proper plasmid assembly was verified by sequencing junctions. Plasmid was transformed into S17-1 and introduced into CB15N by conjugation with selection for kanamycin and nalidixic acid resistance. Second homologous recombination was achieved by counterselection on 0.3 % xylose.

CJW7535	CB15N *rpoC*::*mCherry-rpoC dnaA*::Ω xylX::pGM2195	UV-inactivated ϕCr30 phage lysate was prepared from GM2471. First, pGM2195 was transduced into CJW7531, followed by a second transduction of Ω into the resulting strain to disrupt the endogenous *dnaA* gene.
CJW7563	MG1655 *lacY(A177C) araFGH*::*spec ΔlacI ΔaraE araBAD*::*dCas9 galM<PBBa-J23119-sgRNA(ftsZ)-(S. pyogenes terminator)-(rrnB terminator)>gmpA rpoC*::*rpoC-ygfp-kan*	*rpoC*::*rpoC-ygfp-kan* from RLG7470 was moved into SJ_XTL229 by P1 transduction.
CJW7564	MG1655 *lacY(A177C) araFGH*::*spec ΔlacI ΔaraE araBAD*::*dCas9 galM<PBBa-J23119-sgRNA(ftsZ)-(S. pyogenes terminator)-(rrnB terminator)>gmpA rpsB*::*rpsB-msfgfp-kan*	*rpsB*::*rpsB-msfgfp-kan* from CJW7019 was moved into SJ_XTL229 by P1 transduction.
CJW7569	CB15N *rpoC*::*mCherry-rpoC ftsZ*::pBGentpXyl-ftsZ	UV-inactivated ϕCr30 phage lysate was prepared from CJW2591 and transduced into CJW7531.
CJW7576	MG1655 *lacY(A177C) araFGH*::*spec ΔlacI ΔaraE araBAD*::*dCas9 galM<PBBa-J23119-sgRNA(ftsZ)-(S. pyogenes terminator)-(rrnB terminator)>gmpA hupA*::*hupA-mCherry-kan*	*hupA*::*hupA-mCherry-kan* from CJW5556 (Paintdakhi et al., 2016) was moved into SJ_XTL229 by P1 transduction.
GM2471	CB15N *dnaA*::Ω xylX::pGM2195	(Gorbatyuk and Marczynski, 2001)
LS107	CB15N Δ*bla6*	(West et al., 2002)
MG1655	*F- lambda- ilvG- rfb-50 rph-1*	(Guyer et al., 1981)
MT190	CB15N *parB*::*ecfp-parB*	(Thanbichler and Shapiro, 2006)
RLG7470	*rpoC*::*rpoC-ygfp-kan*	(Bakshi et al., 2012)
SJ_XTL229	*lacY(A177C) araFGH*::*spec ΔlacI ΔaraE araBAD*::*dCas9 galM<PBBa-J23119-sgRNA(ftsZ)-(S. pyogenes terminator)-(rrnB terminator)>gmpA*	(Li et al., 2016)

SJ_XTL676	*lacY(A177C) araFGH::spec ΔlacI ΔaraE araBAD::dCas9 galM<PBBa-J23119-sgRNA(oriC)-(S. pyogenes terminator)-(rrnB terminator)>gmpA*	(Si et al., 2017)
YB1585	CB15N *ftsZ*::pBGST18-pXyl-ftsZ	(Wang et al., 2001)

1481

1482

1483 **Table 4. Oligonucleotides used in this study.**

Name	Sequence
AP0039	ACCCAACTTAATCGCTGTAGGCTGGAGCTGCTTCG
AP0040	ATTAATTGCGTTGCGCAGTTCCCTACTCTCGCATGGG
AP0041	GAGAGTAGGGAACTGCGCAACGCAATTAATGTGAGTTAGC
AP0042	CAGCTCCAGCCTACAGCGATTAAGTTGGGTAACGCCA
AP0078	ATCAAACATCCTGCCAACTCCATGTGACAAACCGTCATCTTCGGCTACTTGCAACGCAATTAATGTGAGTTAGC
AP0079	ACAAACATTAATAACGAAGAGATGACAGAAAAATTTTCATTCTGTGACAGCCCTGATTCCGTGAGGATGC
JSG_018	GCCCGAGGGCACGTGACGCGTCTCCGGATG
JSG_019	ACCTCGGCGATCGCGAACGCCGAAGCTAGCGAATTCGTGGATC
JSG_020	GAATTCGCTAGCTTCGGCGTTCGCGATCGCCGAGGTG
JSG_021	GGCATGGACGAGCTGTACAAGTAAGCCACCCAAGTTTTAGTAAGCG
JSG_022	CGCTTTACTGGGTACGCTTACTAAAACTTGGGTGGCTTACTTGTACAGCTCGTCCATGCC
JSG_023	AACGTTACGCGTCACCGGTCGGCCACCATGGTGAGCAAGGGCGAG
JSG_024	GGCCGACCGGTGACGCGTAACGTTCGAATTGGCGCCGATCGAGCTGATG
JSG_025	CGGAGACGCGTCACGTGCCCTCGGGCACCGGCC
JSG_128	TCCGTAATACGACTCACTTAAGGCCTTGACGATGGTCAAGGTCTTCGTGG
JSG_129	GCCATGTTATCCTCCTCGCCCTTGCTCACCATCTTGGTTCCTTCTGCGGG
JSG_130	TTTTCGCGGGAAACCCCGCAGAAGGAACCAAGATGGTGAGCAAGGGCGAG
JSG_131	TTCAGGACTTCCTGGTTCATGCTGCCGCTGCCGCTGCCCTTGTACAGCTCGTCCATGC
JSG_132	AGCTGTACAAGGGCAGCGGCAGCGGCAGCATGAACCAGGAAGTCCTGAAC
JSG_133	ATGTACAGGCATGCGTCGACCCTCTAAGCATCCGCTTTTCGTTG
JSG_134	CGCAACGAAAAGCGGATGCTTAGAGGGTCGACGCATGC
JSG_135	CACGAAGACCTTGACCATCGTCAAGGCCTTAAGTGAGTCG
JSG_136	TTATCCGTACTCCTGATGATGC
JSG_137	GGGATCGCAGTGGTGAGTAAC
JSG_148	GCCTGGCAGAACTGCTGAACGCAGGTCTGGGCGGTTCTGATAACGAGTAATCGGCTGGCTCCGCTGCT
JSG_149	CATAAAAAAACCCGCCGAAGCGGGTTTTTACGTTATTTGCGGATTAACGAGGATCCCATATGAATATCCTCCTT

JSG_157	GTTCTCAGGATCTGGCTTCCCAGGCGGAAGAAAGCTTCGTAGAAGCTGAGTCGGCTGG CTCCGCTGCT
JSG_158	TTGCCGCCTTTCTGCAACTCGAACTATTTTGGGGGAGTTATCAAGCCTTAGGATCCCAT ATGAATATCCTCCTT
JSG_173	AAAAAAGCAAAAGGGCCGCAGATGCGACCCTTGTGTATCAAACAAGACGAGTGTAGG CTGGAGCTGCTTC
JSG_174	CAACAGAACATATTGACTATCCGGTATTACCCGGCATGACAGGAGTAAAATGTACAAG AAAGCTGGGTACG
NT157	TATGGATCCTGTTTTTCACCACGCCAATTTCATGG
NT158	TATGGTACCGAGGTTGAAAAGCGTGGTG

1484

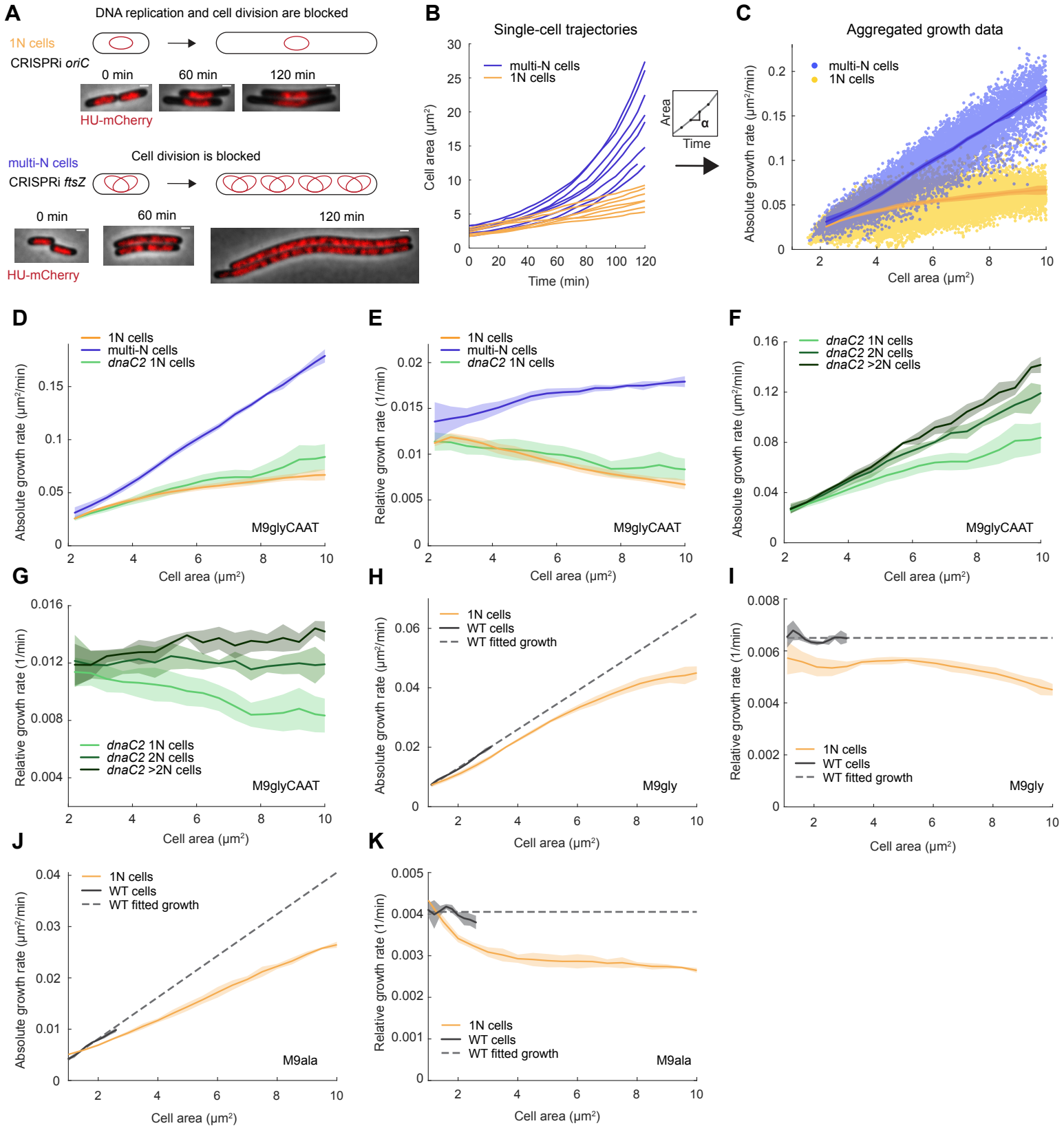
A
DNA replication and cell division are blocked
1N cells
CRISPRi oriC
0 min
60 min
120 min
HU-mCherry
multi-N cells
Cell division is blocked
CRISPRi ftsZ
0 min
60 min
120 min
HU-mCherry
B
Single-cell trajectories
multi-N cells
1N cells
Cell area (μm²)
Time (min)
Area
Time
α
C
Aggregated growth data
multi-N cells
1N cells
Absolute growth rate (μm²/min)
Cell area (μm²)
D
1N cells
multi-N cells
dnaC2 1N cells
Absolute growth rate (μm²/min)
M9glyCAAT
Cell area (μm²)
E
1N cells
multi-N cells
dnaC2 1N cells
Relative growth rate (1/min)
M9glyCAAT
Cell area (μm²)
F
dnaC2 1N cells
dnaC2 2N cells
dnaC2 >2N cells
Absolute growth rate (μm²/min)
M9glyCAAT
Cell area (μm²)
G
dnaC2 1N cells
dnaC2 2N cells
dnaC2 >2N cells
Relative growth rate (1/min)
M9glyCAAT
Cell area (μm²)
H
1N cells
WT cells
WT fitted growth
Absolute growth rate (μm²/min)
M9gly
Cell area (μm²)
I
1N cells
WT cells
WT fitted growth
Relative growth rate (1/min)
M9gly
Cell area (μm²)
J
1N cells
WT cells
WT fitted growth
Absolute growth rate (μm²/min)
M9ala
Cell area (μm²)
K
1N cells
WT cells
WT fitted growth
Relative growth rate (1/min)
M9ala
Cell area (μm²)

Figure 1

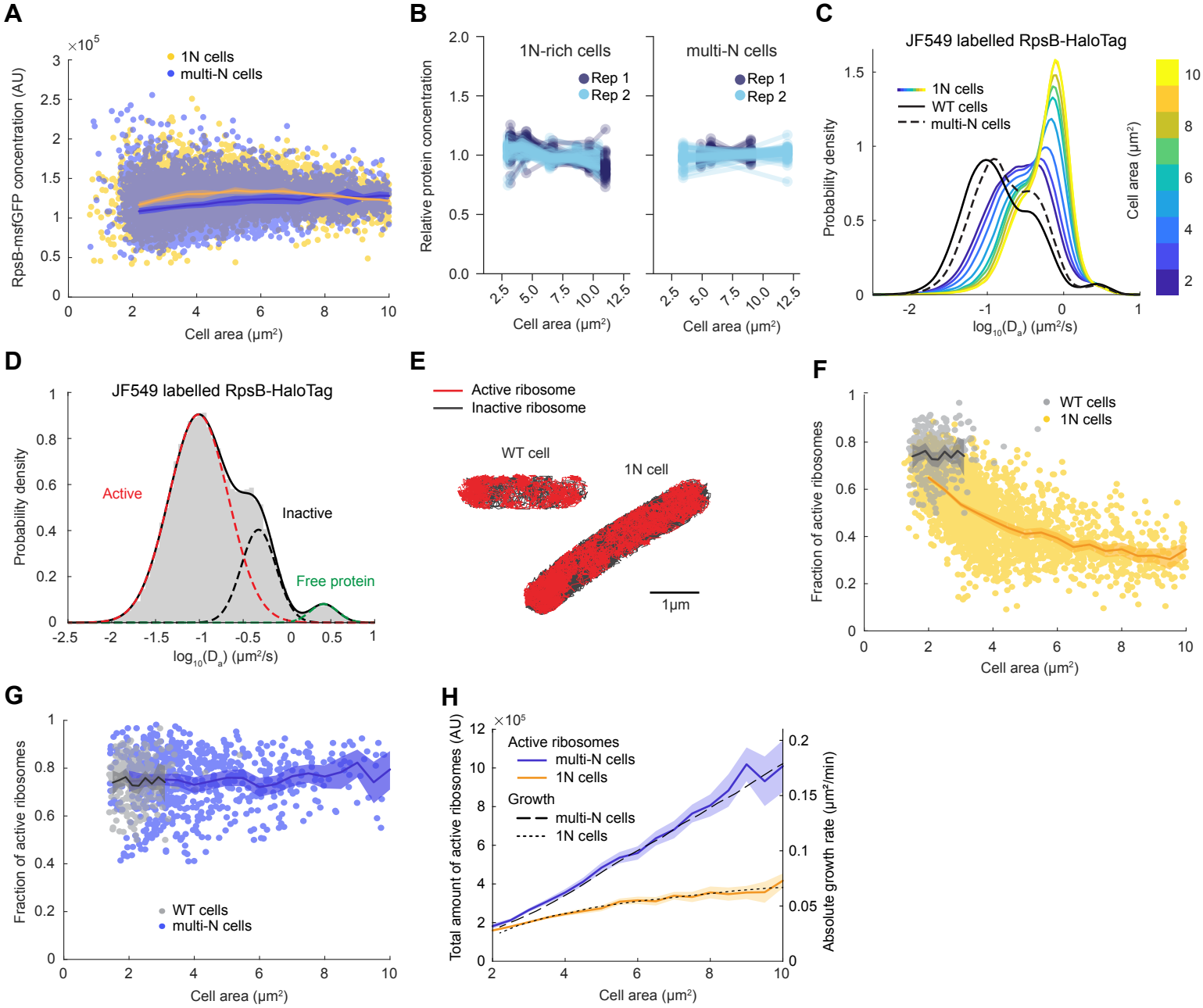
A
×10^5
1N cells
multi-N cells
RpsB-msfGFP concentration (AU)
Cell area (μm²)
B
1N-rich cells
multi-N cells
Rep 1
Rep 2
Relative protein concentration
Cell area (μm²)
C
JF549 labelled RpsB-HaloTag
1N cells
WT cells
multi-N cells
Probability density
Cell area (μm²)
log10(Da) (μm²/s)
D
JF549 labelled RpsB-HaloTag
Active
Inactive
Free protein
Probability density
log10(Da) (μm²/s)
E
Active ribosome
Inactive ribosome
WT cell
1N cell
1μm
F
WT cells
1N cells
Fraction of active ribosomes
Cell area (μm²)
G
WT cells
multi-N cells
Fraction of active ribosomes
Cell area (μm²)
H
×10^5
Active ribosomes
multi-N cells
1N cells
Growth
multi-N cells
1N cells
Total amount of active ribosomes (AU)
Absolute growth rate (μm²/min)
Cell area (μm²)

Figure 2

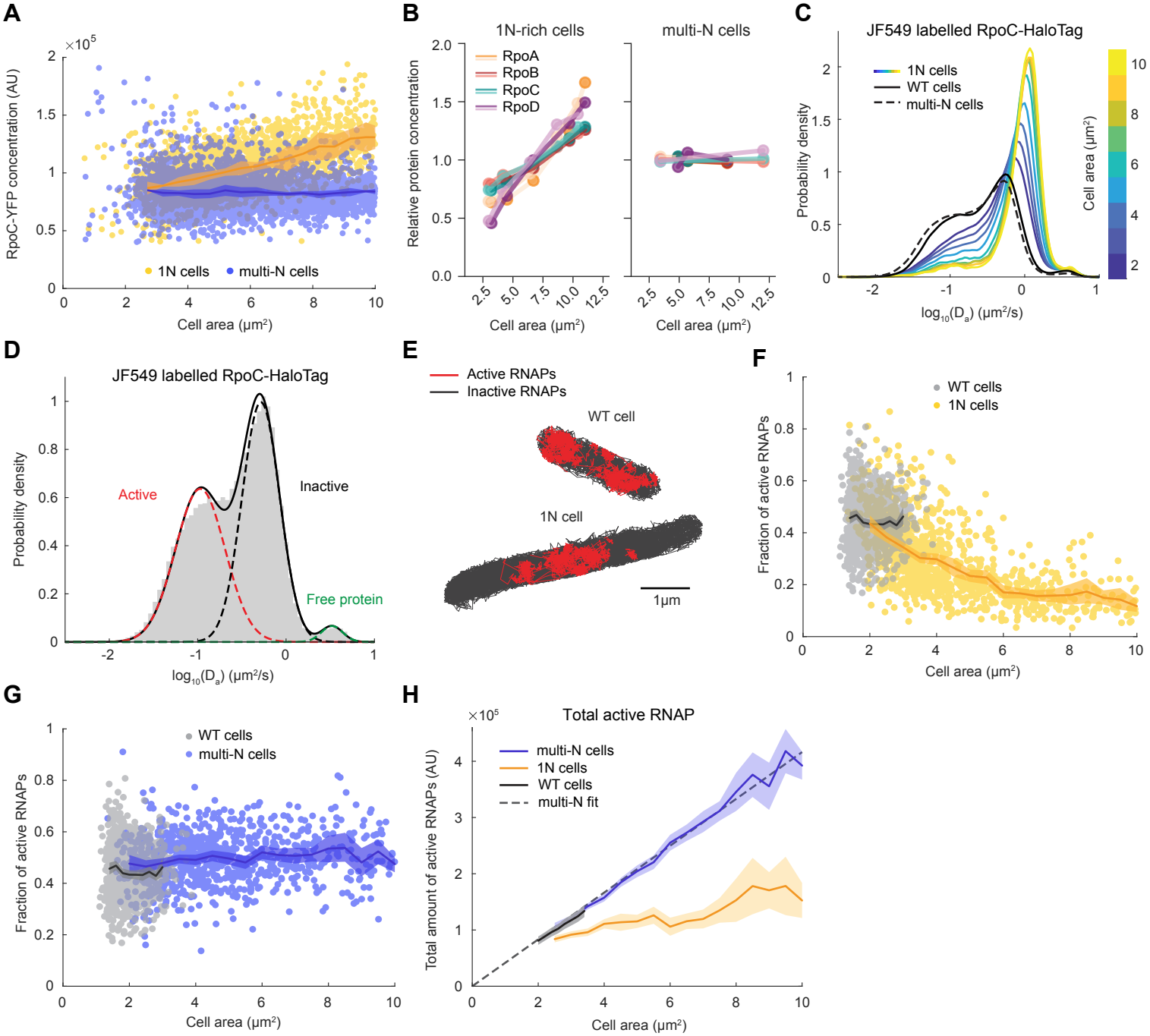
A
RpoC-YFP concentration (AU)
×10^5
1N cells
multi-N cells
Cell area (μm²)
B
1N-rich cells
multi-N cells
RpoA
RpoB
RpoC
RpoD
Relative protein concentration
Cell area (μm²)
C
JF549 labelled RpoC-HaloTag
1N cells
WT cells
multi-N cells
Probability density
Cell area (μm²)
log10(Da) (μm²/s)
D
JF549 labelled RpoC-HaloTag
Active
Inactive
Free protein
Probability density
log10(Da) (μm²/s)
E
Active RNAPs
Inactive RNAPs
WT cell
1N cell
1μm
F
WT cells
1N cells
Fraction of active RNAPs
Cell area (μm²)
G
WT cells
multi-N cells
Fraction of active RNAPs
Cell area (μm²)
H
Total active RNAP
×10^5
multi-N cells
1N cells
WT cells
multi-N fit
Total amount of active RNAPs (AU)
Cell area (μm²)

Figure 3

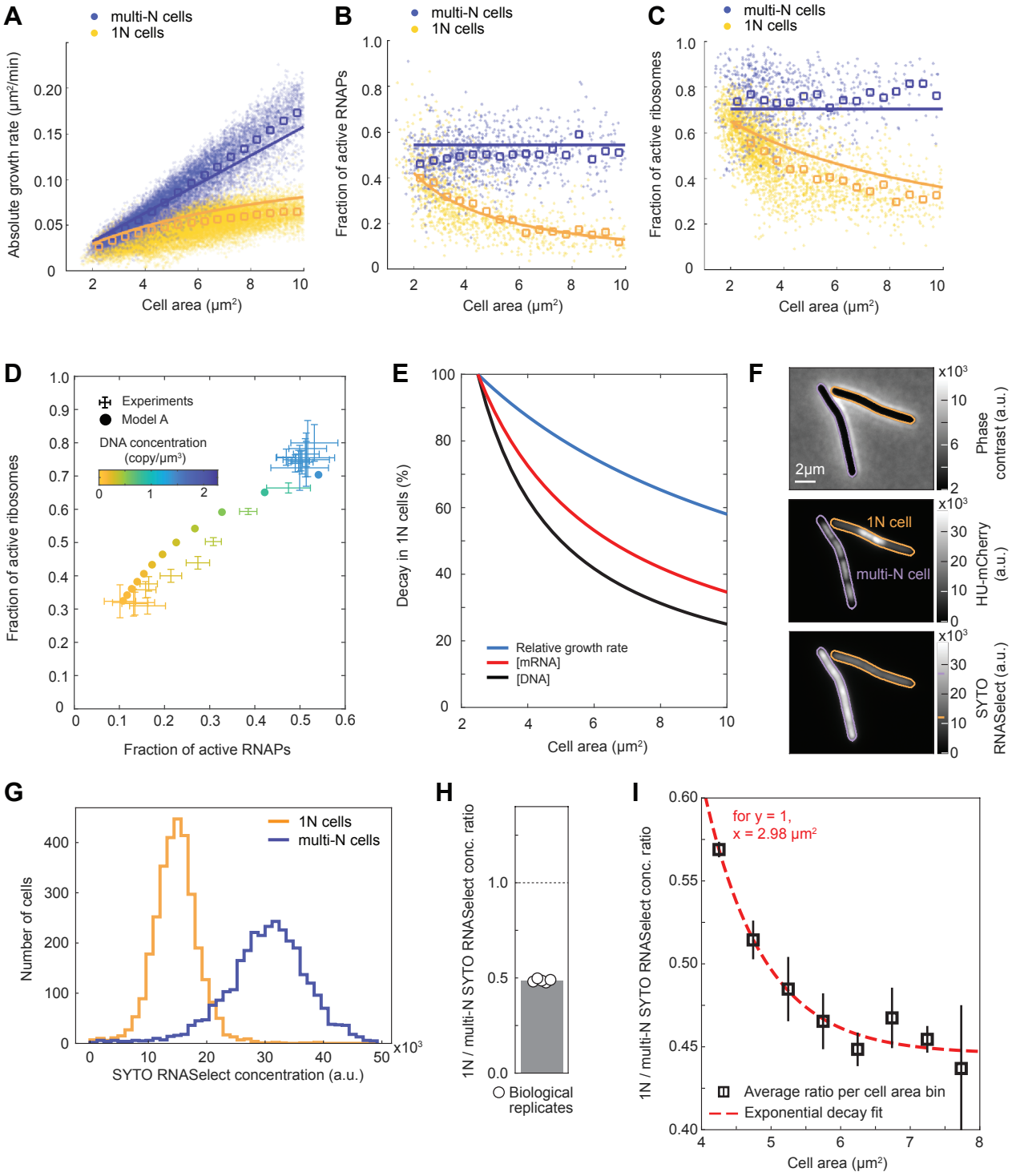
A
multi-N cells
1N cells
Absolute growth rate (μm²/min)
Cell area (μm²)
B
Fraction of active RNAPs
C
Fraction of active ribosomes
D
Experiments
Model A
DNA concentration (copy/μm³)
Fraction of active ribosomes
Fraction of active RNAPs
E
Decay in 1N cells (%)
Relative growth rate
[mRNA]
[DNA]
F
2μm
1N cell
multi-N cell
Phase contrast (a.u.)
HU-mCherry (a.u.)
SYTO RNASelect (a.u.)
G
1N cells
multi-N cells
Number of cells
SYTO RNASelect concentration (a.u.)
H
1N / multi-N SYTO RNASelect conc. ratio
Biological replicates
I
for y = 1,
x = 2.98 μm²
1N / multi-N SYTO RNASelect conc. ratio
Average ratio per cell area bin
Exponential decay fit
Cell area (μm²)

Figure 4

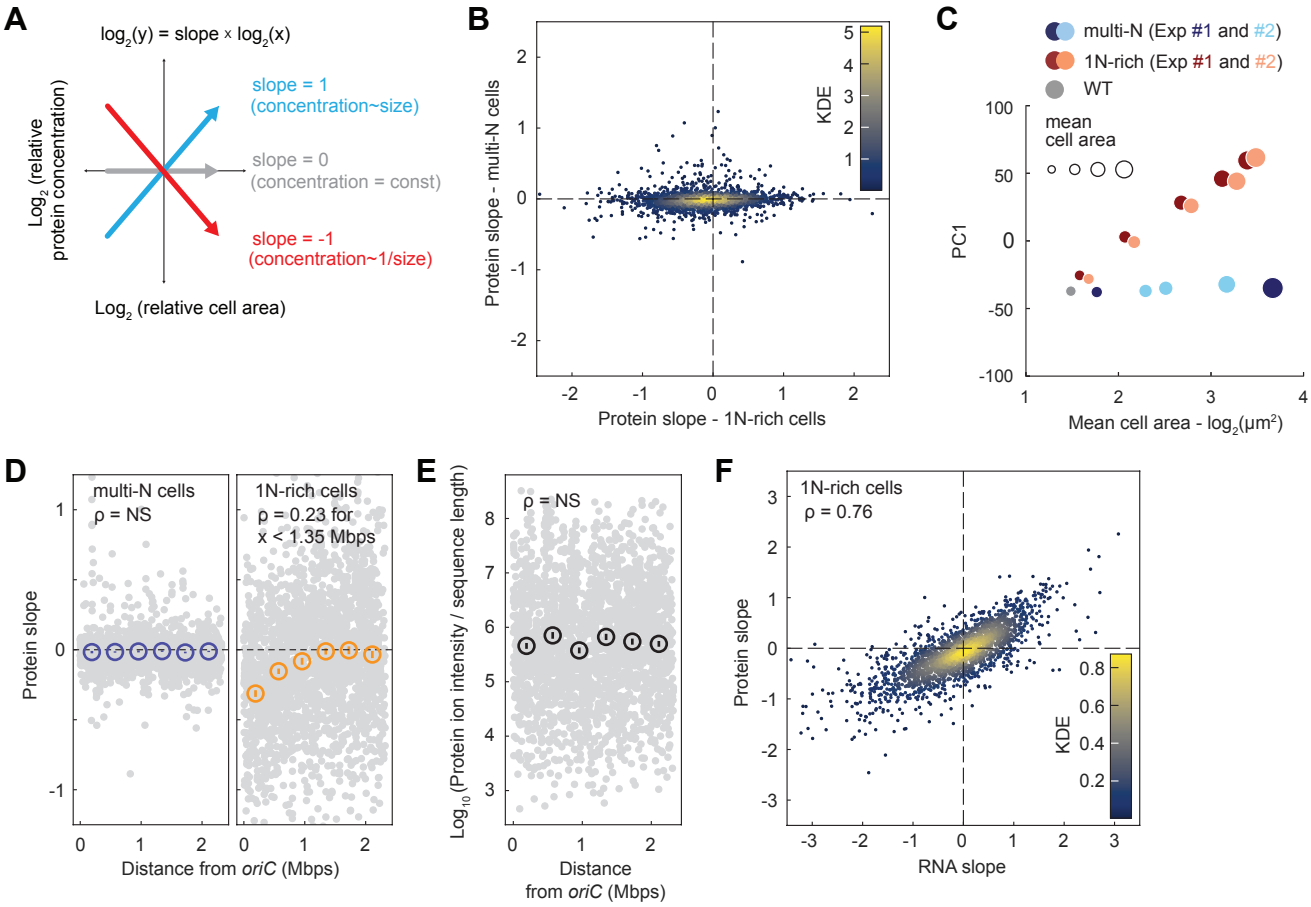
A
log2(y) = slope × log2(x)
slope = 1
(concentration~size)
slope = 0
(concentration = const)
slope = -1
(concentration~1/size)
Log2 (relative protein concentration)
Log2 (relative cell area)
B
Protein slope - multi-N cells
Protein slope - 1N-rich cells
KDE
C
multi-N (Exp #1 and #2)
1N-rich (Exp #1 and #2)
WT
mean cell area
PC1
Mean cell area - log2(μm²)
D
multi-N cells
ρ = NS
1N-rich cells
ρ = 0.23 for
x < 1.35 Mbps
Protein slope
Distance from oriC (Mbps)
E
ρ = NS
Log10(Protein ion intensity / sequence length)
Distance
from oriC (Mbps)
F
1N-rich cells
ρ = 0.76
Protein slope
RNA slope
KDE

Figure 5

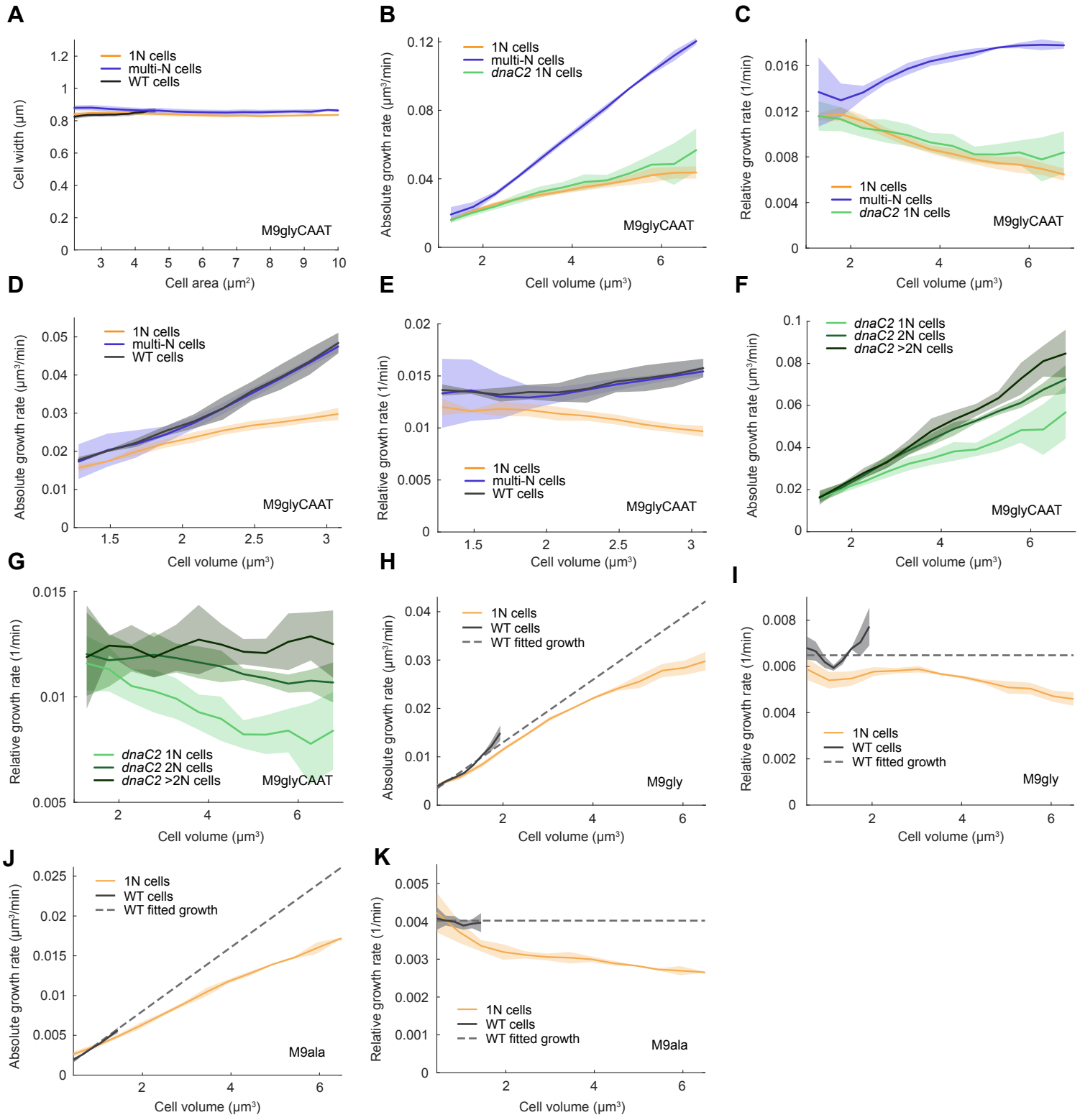

Fig 1 Fig supplement 1

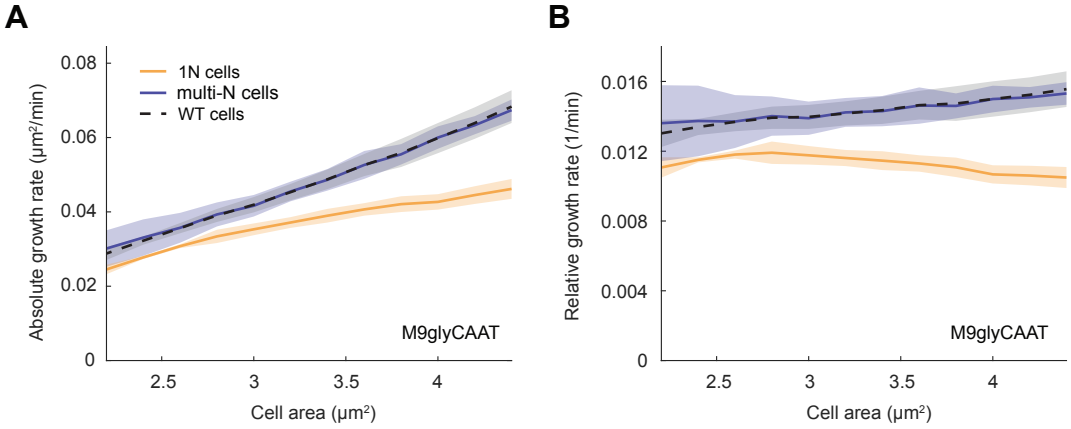

Fig 1 Fig supplement 2

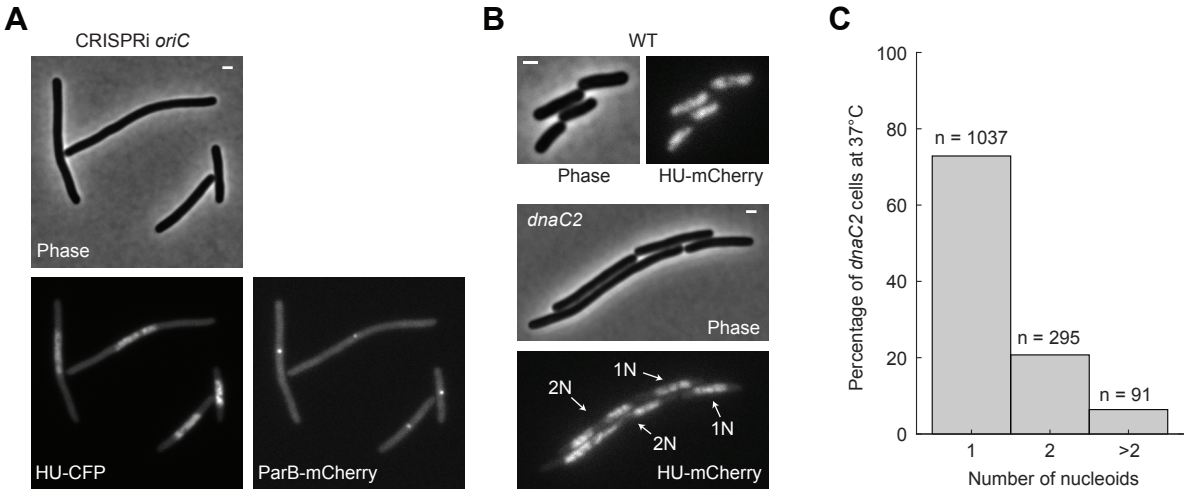

Fig 1 Fig supplement 3

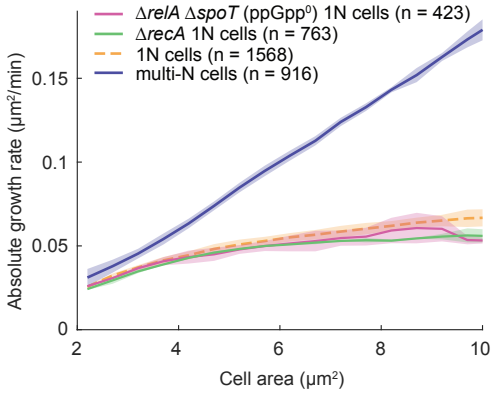

Fig 1 Fig supplement 4

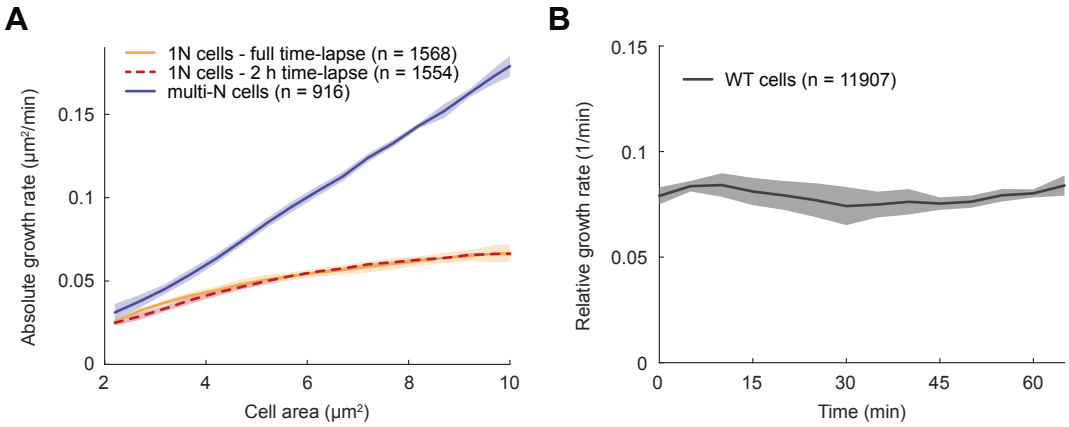

Fig 1 Fig supplement 5

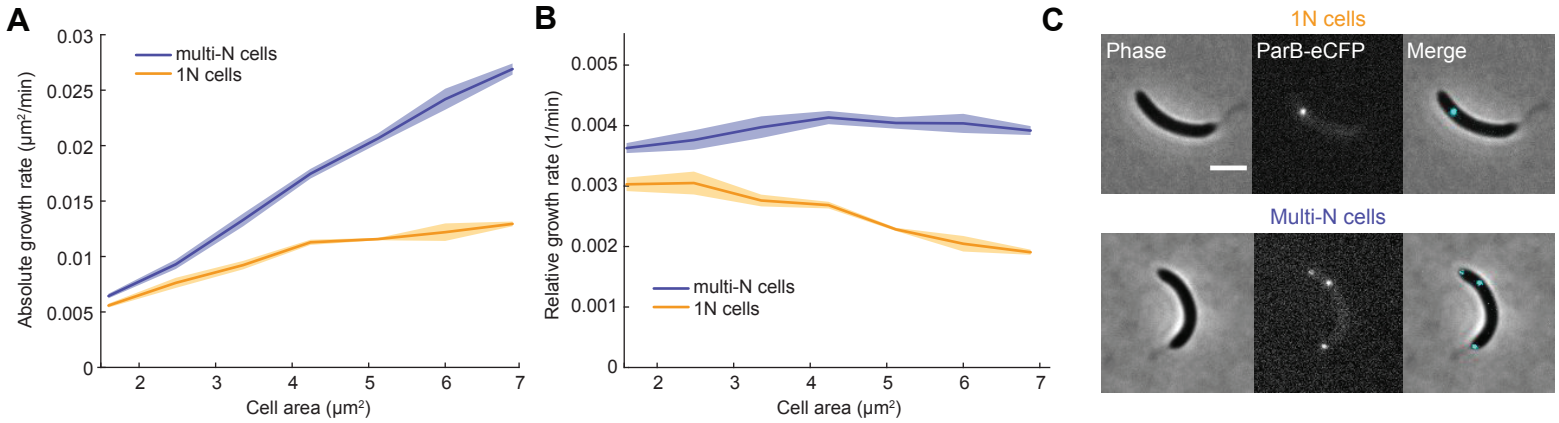

Fig 1 Fig supplement 6

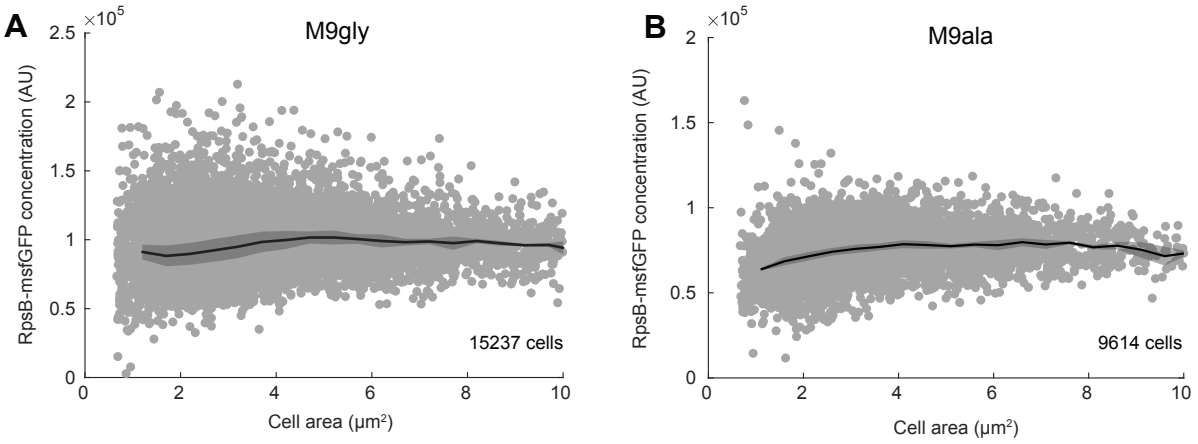

Fig 2 Fig supplement 1

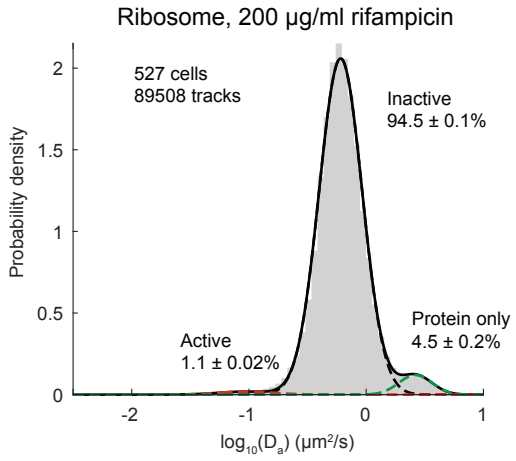

Fig 2 Fig supplement 2

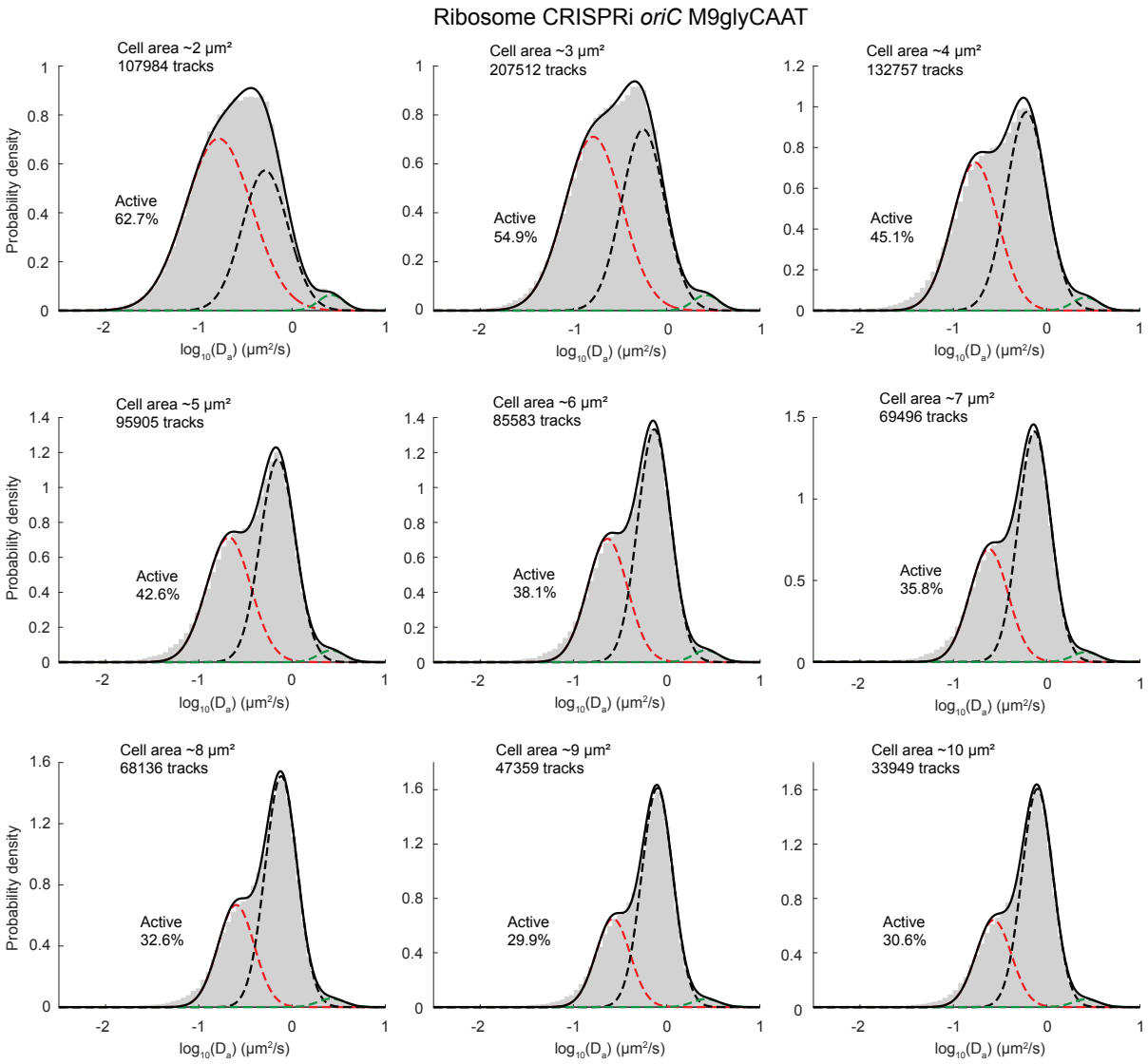

Fig 2 Fig supplement 3

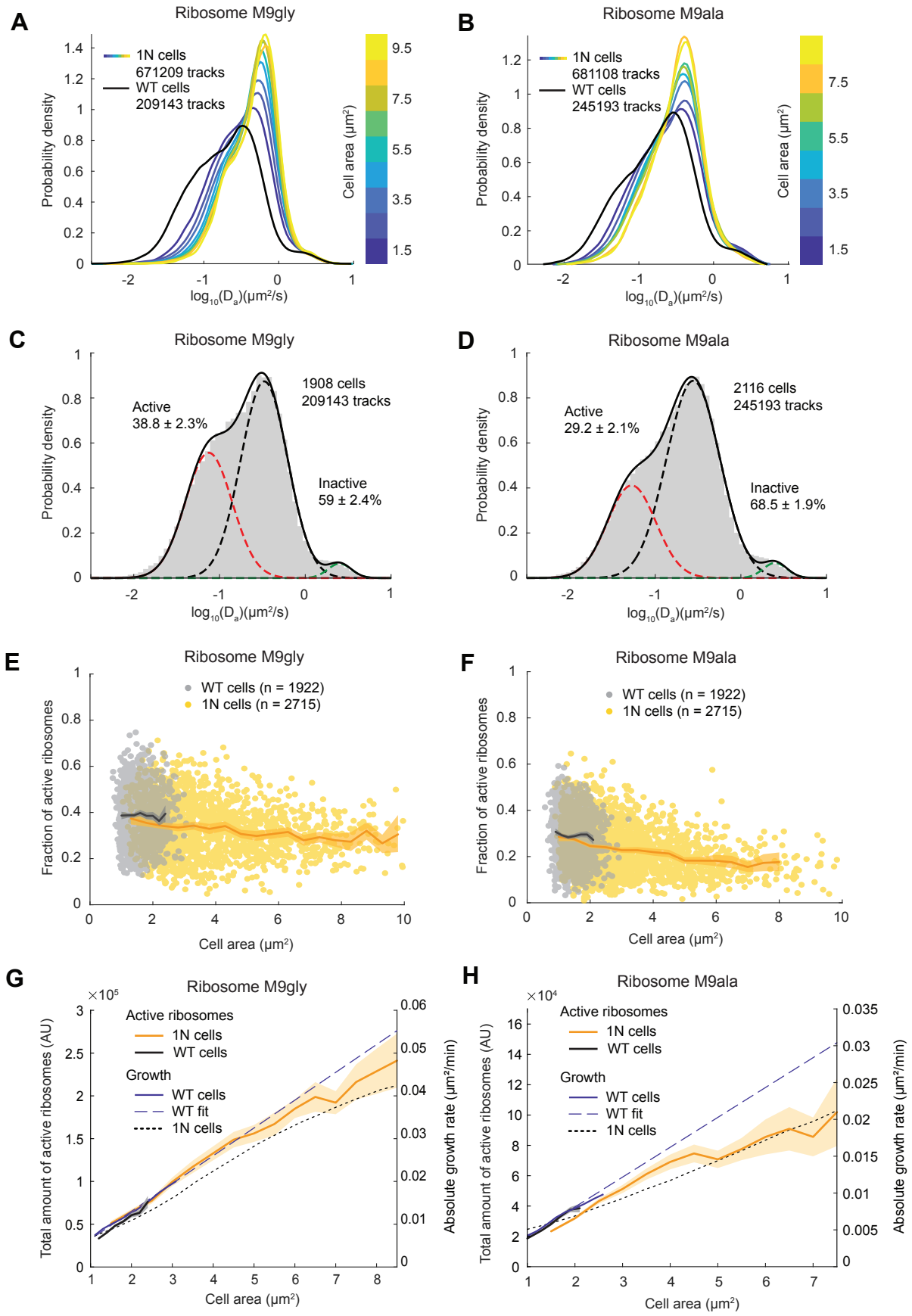

Fig 2 Fig supplement 4

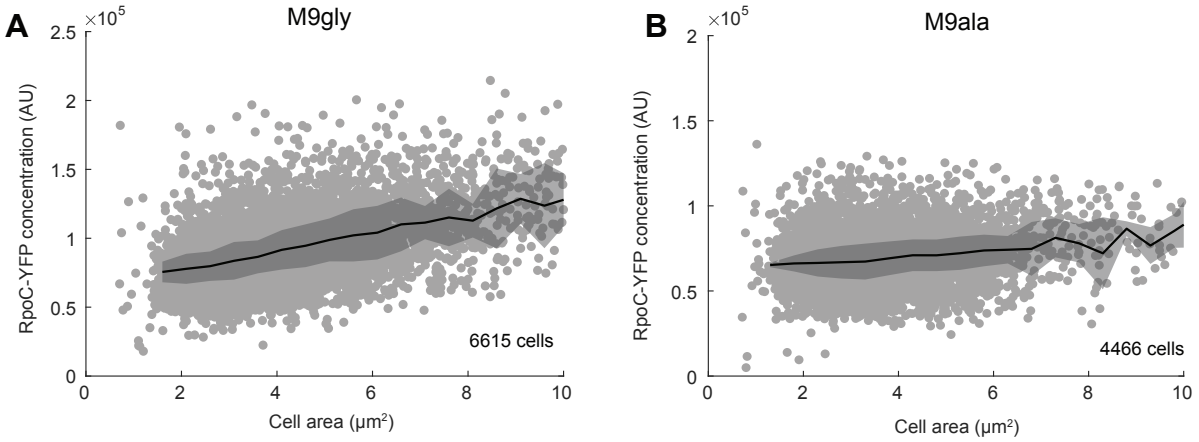

Fig 3 Fig supplement 1

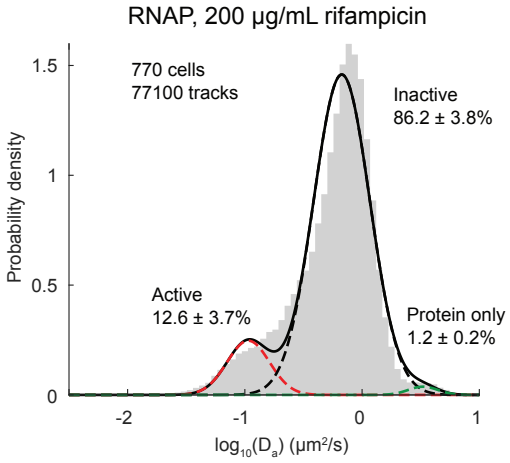

Fig 3 Fig supplement 2

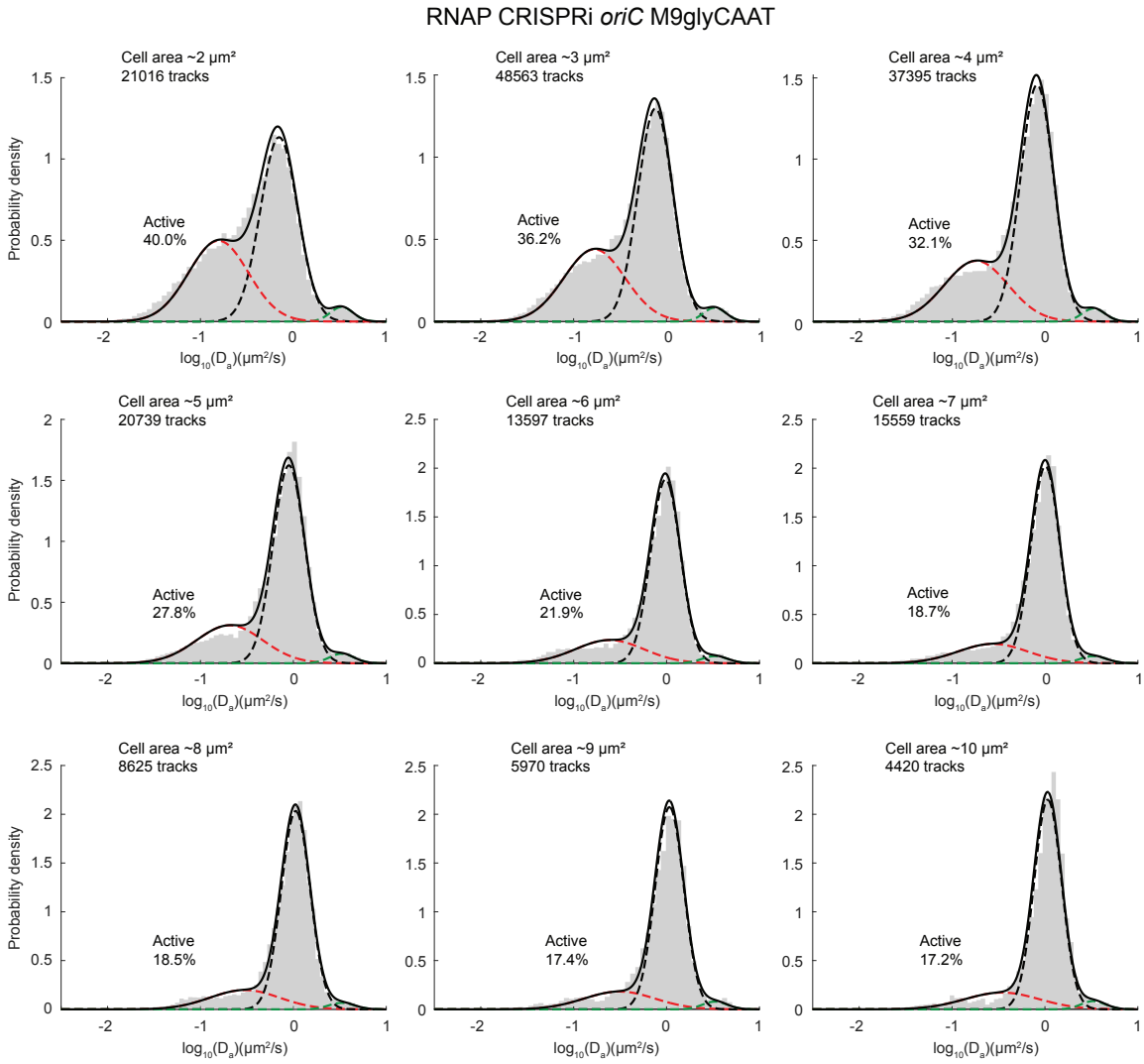

Fig 3 Fig supplement 3

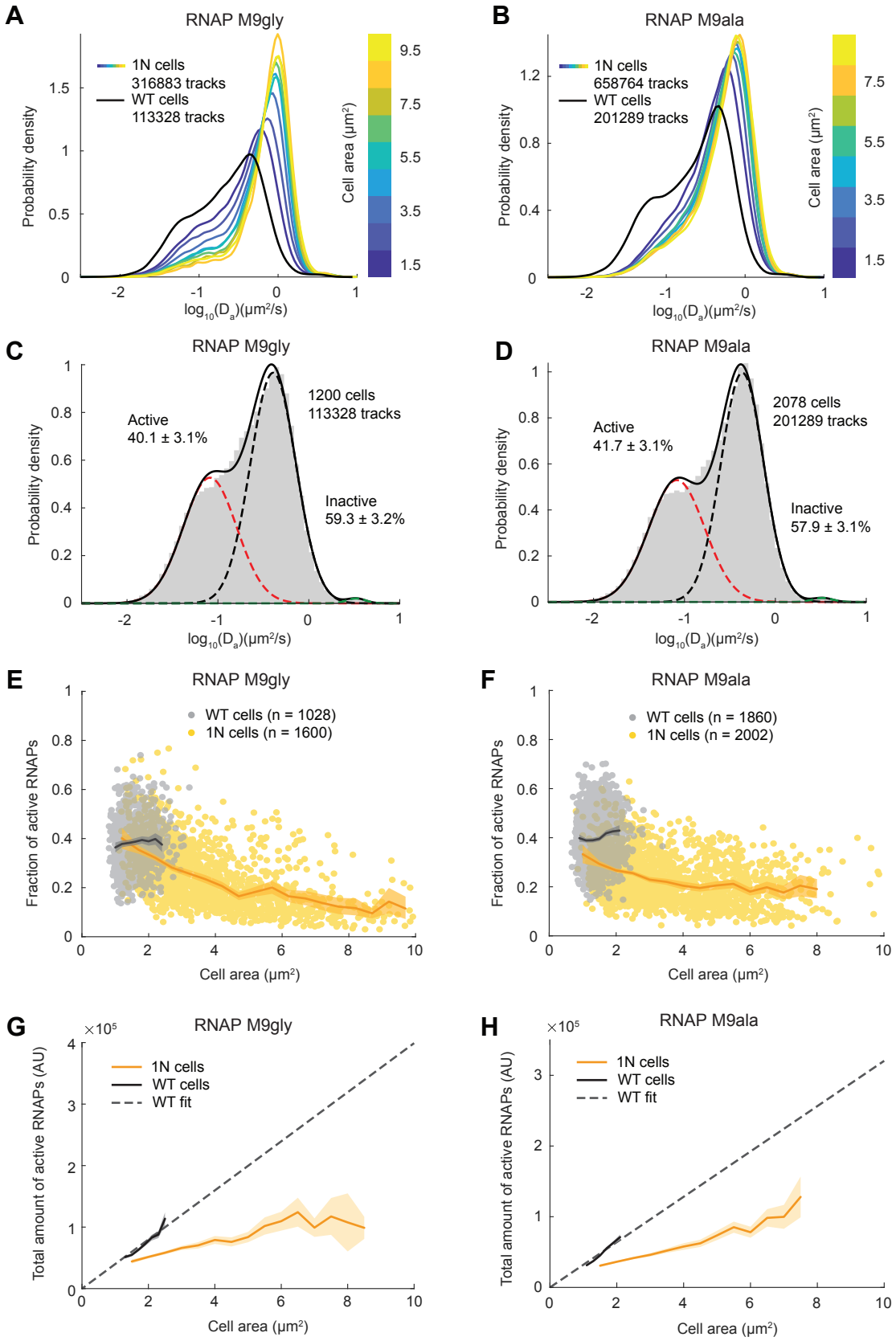

Fig 3 Fig supplement 4

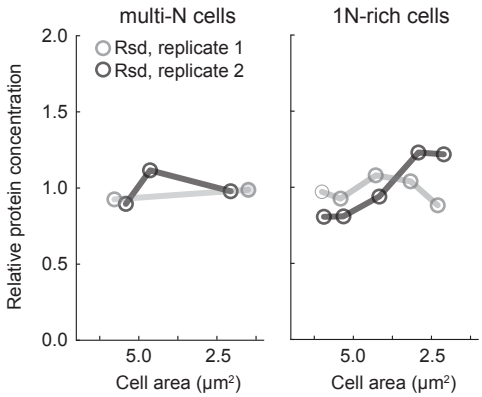

Fig 3 Fig supplement 5

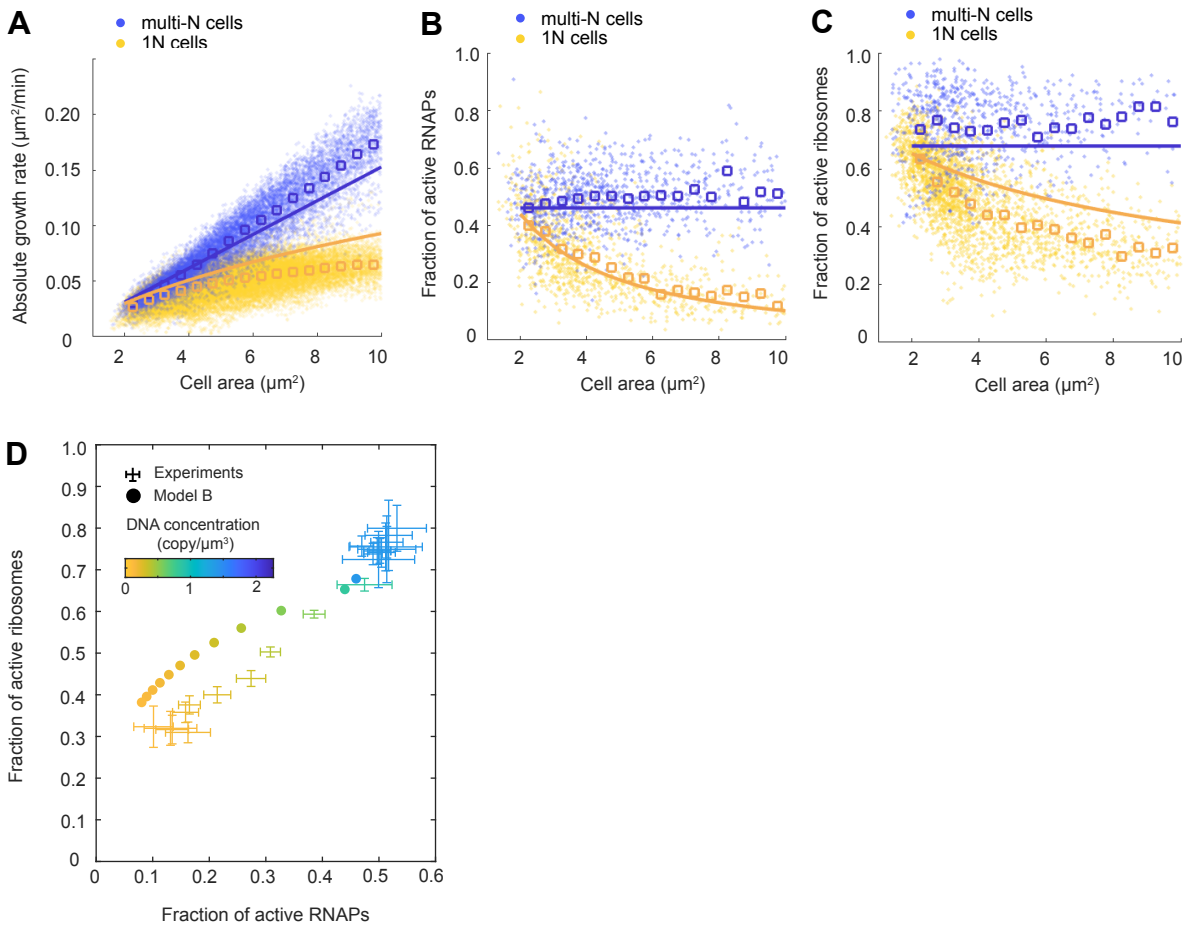

Fig 4 Fig supplement 1

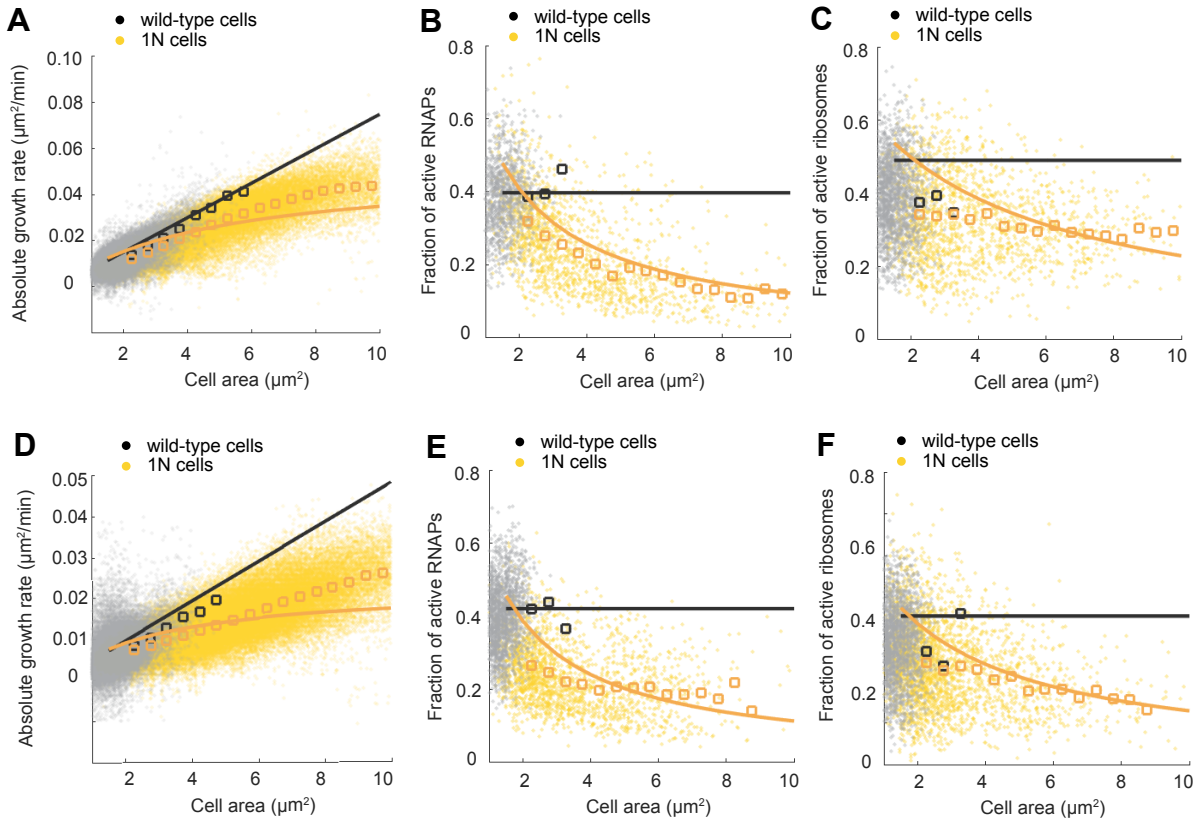

Fig 4 Fig supplement 2

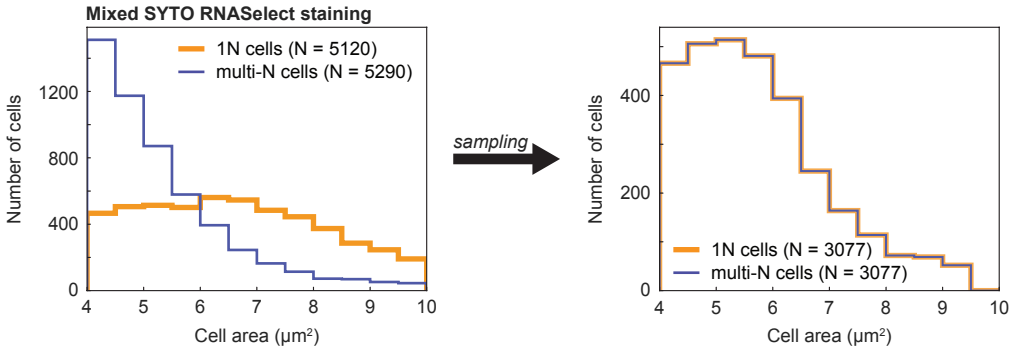

Fig 4 Fig supplement 3

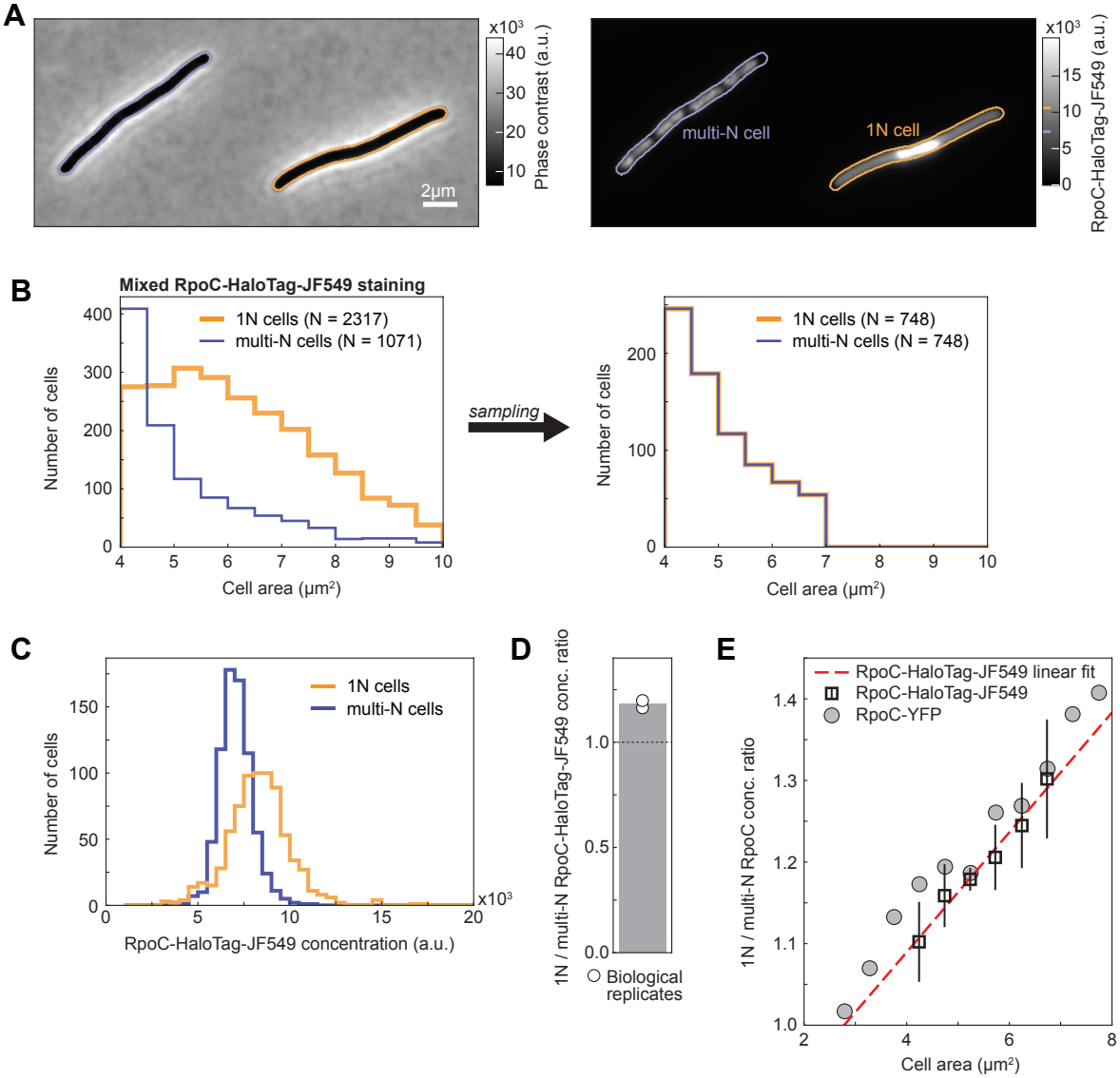

Fig 4 Fig supplement 4

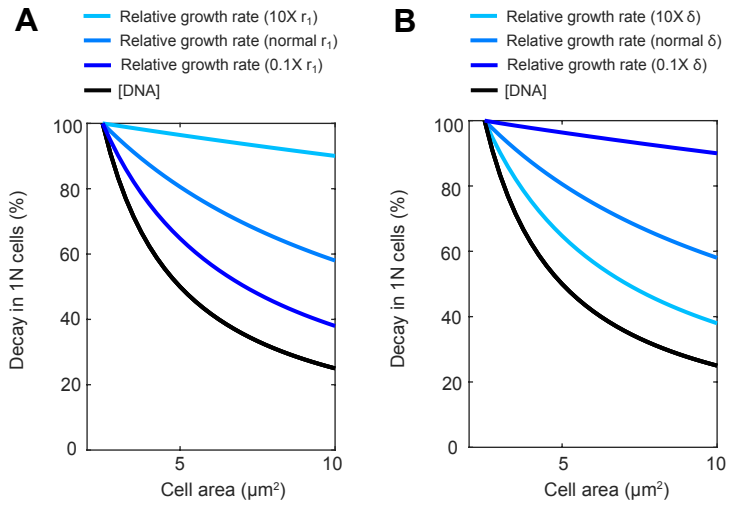

Fig 4 Fig supplement 5

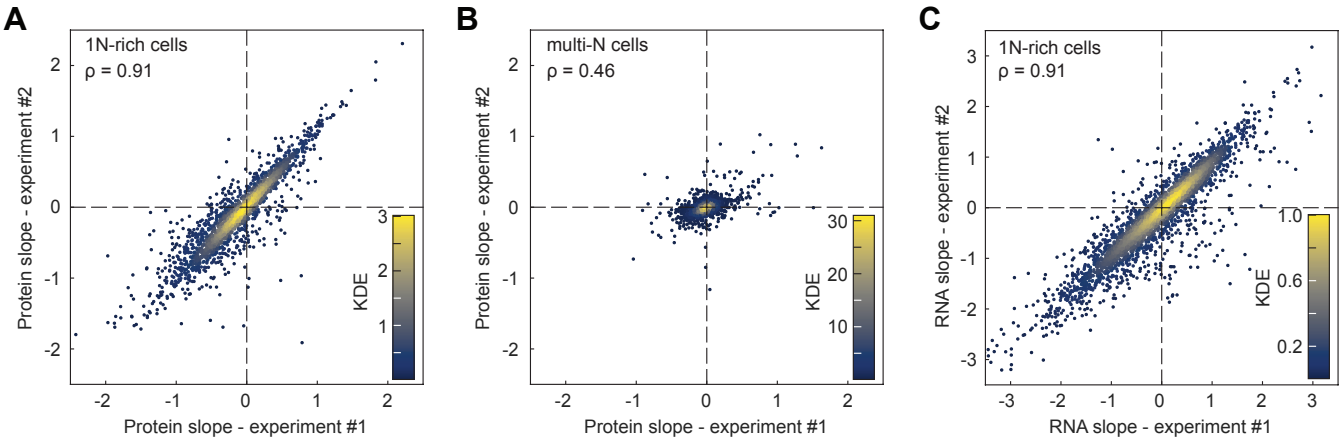

Fig 5 Fig supplement 1

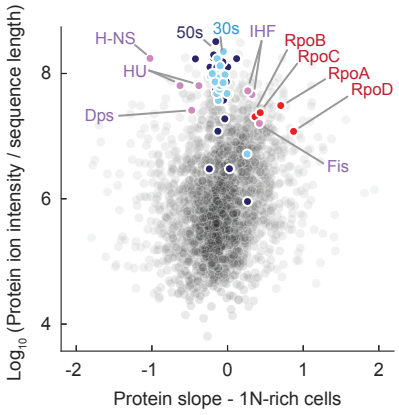

Fig 5 Fig supplement 2